

Titre: Active Antireflective Coatings for Ophthalmic and Architectural
Title: Applications

Auteur: Louis Dubé Riopel
Author:

Date: 2020

Type: Mémoire ou thèse / Dissertation or Thesis

Référence: Dubé Riopel, L. (2020). Active Antireflective Coatings for Ophthalmic and
Citation: Architectural Applications [Mémoire de maîtrise, Polytechnique Montréal].
PolyPublie. <https://publications.polymtl.ca/5441/>

 **Document en libre accès dans PolyPublie**
Open Access document in PolyPublie

URL de PolyPublie: <https://publications.polymtl.ca/5441/>
PolyPublie URL:

**Directeurs de
recherche:** Ludvik Martinu, & Jolanta-Ewa Sapiuha
Advisors:

Programme: Génie physique
Program:

POLYTECHNIQUE MONTRÉAL

affiliée à l'Université de Montréal

Active antireflective coatings for ophthalmic and architectural applications

LOUIS DUBÉ RIOPEL

Département de génie physique

Mémoire présenté en vue de l'obtention du diplôme de *Maîtrise ès sciences appliquées*

Génie physique

Août 2020

© Louis Dubé Riopel, 2020.

POLYTECHNIQUE MONTRÉAL

affiliée à l'Université de Montréal

Ce mémoire intitulé :

Active antireflective coatings for ophthalmic and architectural applications

présenté par **Louis DUBÉ RIOPEL**

en vue de l'obtention du diplôme de *Maîtrise ès sciences appliquées*

a été dûment accepté par le jury d'examen constitué de :

Yves-Alain PETER, président

Ludvik MARTINU, membre et directeur de recherche

Jolanta-Ewa SAPIEHA, membre et codirectrice de recherche

Clara SANTATO, membre

ACKNOWLEDGEMENTS

I want to gratefully acknowledge my research director Pr Ludvik Martinu and co-director Pr Jolanta-Ewa Sapieha for granting me the opportunity to fulfill this project, and also the industrial partners Essilor and Guardian for their interest and support.

During the project, Dr Bill Baloukas' support was essential to achieve the resulting conclusions, as his knowledge and passion to help reflect in the success of the ones he is associated with, and I thank him for that. Also, I would like to acknowledge the help of the members of the group, more precisely Oleg for his thoughtful insights, also Francis, Phillip, Antonin, Sasha, and everyone who contributed to the project's progression in the animated group meeting discussions.

I would also like to underline the support from the technical group composed of Francis Turcot, Francis Boutet and Samuel Cardinal, without whom our creativity would be limited to theoretical and analytical work.

Last but not least, I thank all my friends and family for their support during the whole degree, as well as Sally, for supporting through life in our daily routine, making me a better man.

RÉSUMÉ

La variation de la couleur d'une fenêtre est un concept bien étudié à des fins énergétiques, pratiques et esthétiques. Il est facile de s'imaginer une fenêtre de salle de conférence devenir floue au besoin, ou les lunettes de quelqu'un sortant à l'extérieur s'assombrir. Plusieurs technologies permettent de varier dynamiquement la façon dont laquelle la lumière interagit avec une surface, cependant l'électrochromisme prend de plus en plus de place sur le marché. Des miroirs de voiture aux hublots d'avion, cette technologie permet de colorer ou de blanchir une surface à l'aide de l'application d'un courant électrique. Cette simplicité dans son fonctionnement a permis l'émergence de cette technologie, contrairement à certaines qui dépendent de conditions comme la lumière ou la température, ce pour quoi plusieurs matériaux ont été étudiés pour leurs propriétés électrochromiques.

Le mécanisme permettant à un matériau électrochromique de se colorer dépend de sa structure, mais le principe de base repose sur l'intercalation, qui est l'insertion d'un ion et d'un électron dans le matériau. Le matériau électrochromique cathodique le plus prometteur est l'oxyde de tungstène (WO_3), principalement à cause de sa grande efficacité de coloration ainsi que sa stabilité structurale. Partant d'un état transparent, lors de l'intercalation d'un proton ou d'un ion de lithium dans sa maille, une bande d'absorption est observée dans le spectre visible/proche infrarouge résultant une couleur bleutée. Le comportement contraire, anodique, est observé chez l'oxyde de nickel, étant le matériau contre électrochromique communément utilisé. Lorsqu'intégrés dans un dispositif, les matériaux cathodiques et anodiques agissent de façon complémentaire, augmentant la coloration résultante.

Dans ce travail, un des principaux objectifs a été la conception d'un dispositif électrochromique solide, pouvant varier d'un comportement anti réflecteur dans l'état blanchit à un comportement réflecteur lorsque coloré. La modélisation, les procédés de fabrication et les outils de caractérisation ont été étudiés afin d'approfondir nos connaissances sur les filtres électrochromiques. Des programmes Matlab ont été écrits afin de modéliser la réponse optique des dispositifs, accompagnés d'autres logiciels permettant l'optimisation de l'épaisseur des couches. Selon les résultats modélisés avec des propriétés théoriques des matériaux, une variation de réflexion dans le visible de 4,2% à 7,1% était possible. La pulvérisation magnétron a été l'outil de fabrication choisit, permettant un contrôle de procédé précis ainsi qu'un large éventail de matériau

d'être déposé. L'état du substrat a été un élément critique, car des courts-circuits sont apparus entre les électrodes du dessus et du dessous en raison de particule sur la surface avant le dépôt. Après la fabrication, des mesures optiques (spectrophotométrie et ellipsométrie) ont été effectuées sur les dispositifs fabriqués, soutenus de mesure électrique (résistance et courant) durant l'application d'un voltage. Le dispositif final fabriqué était peu réflecteur (4%), cependant, lorsque coloré, la réflectivité a diminué (1%), proposant ainsi un désaccord entre les propriétés modélisées des matériaux actifs et celle mesurées dans un dispositif solide.

L'autre objectif principal de ce travail est l'étude des propriétés électrochromiques de l'oxyde de nickel. Étant le matériau de choix pour remplir le rôle de couche anodique dans le dispositif, des études de ses propriétés optiques et électrochimiques sont toutefois limitées dans la littérature. Afin de mieux comprendre la coloration de ce matériau, une caractérisation électrochimique rigoureuse de l'oxyde de nickel fut entreprise dans une solution de KOH lors de tests de voltammétrie cyclique (30 cycles allant de -0,6 V à 0,7 V à un taux de 0,1 V/s). En parallèle, des mesures spectrophotométrique et ellipsométrique furent faites, démontrant des augmentations de 1,88 à 2,05 et de 0,04 à 0,16 de l'indice de réfraction et du coefficient d'extinction à 550 nm respectivement, corrélant propriétés optiques et électrochimiques. Avec une caractérisation microstructurale (XRD, RBS et ERD) du film déterminant une structure Fm3m CFC ainsi que d'une composition de $\text{NiO}_{0.260}\text{O}_{0.53}\text{H}_{0.205}$ et une densité de $3,55\text{g/cm}^3$.

ABSTRACT

The variation of the coloration of glass is a concept studied widely nowadays for energetic, practical and aesthetics reasons. One can think of conference room windows blurring off on purpose, or someone's glasses turning to a dark blue color when stepping outside. While many technologies allow a dynamic variation of light interacting with a surface, electrochromism is starting to occupy a larger place on the development market. From car mirrors to airplane windows, this technology allows to color or bleach a surface by applying an electrical current. The easy controllability and simplicity being the main factors pushing this technology forward, as it is not dependent to ambient condition such as temperature or light, many materials have been studied for their electrochromic properties.

The mechanism allowing an electrochromic material to color varies depending on the structure, but the principle lies on intercalation, where an ion and an electron are inserted into the material. The most prominent cathodic electrochromic material is tungsten oxide (WO_3), mainly due to its large coloration efficiency and structural stability. Being transparent in its pristine state, when a hydrogen or lithium ion intercalates its lattice, an absorption band is observed in the visible/NIR spectrum and the material exhibits a blue color. The opposite behavior, termed anodic electrochromism, is observed in nickel oxide the tradition counter EC material in most present day devices. When combined into an electrochromic device, cathodic and anodic materials act complementary, increasing the resulting coloration.

In this work, the first main objective was to design and fabricate a full electrochromic device that was varying from an antireflective bleached state to a reflective colored state. The modeling, fabrication process and characterization tools were studied to increase our knowledge of electrochromic filters. *Matlab* programs were written to model the optical response of the device, along other softwares that allowed the optimization of the layers' thicknesses. According to the modeled performances of theoretical properties, a visible reflection variation from 4.2% to 7.2% was calculated. Magnetron sputtering was the chosen fabrication technique, as a precise microstructural and process control was possible, and a large variety of materials were available for deposition. The surface state of the substrate proved to be critical, as short-circuits between the top and bottom electrodes were observed due to particles on the surface prior to deposition. Following fabrication, optical (spectrophotometry and ellipsometry) measurements were made on the fabricated devices,

along with electrical measurements (resistance and current) upon voltage application. The deposited structure was lowly reflective (4%), however, when colored, the reflectivity lowered even more (1%), suggesting a mismatch between the modeled properties of the active materials and their behavior inside a device.

The second main objective presented in this work is the study of the electrochromic properties of nickel oxide. Being the best suited material for the anodic layer inside the device, studies of its optical and electrochemical properties are limited in the literature. To improve our comprehension of the coloration of the material, rigorous electrochemical characterization of nickel oxide films was undertaken inside a KOH solution during cyclic voltammetry testing (30 cycles between -0.6 V and 0.7V at a 0.1V/s scan rate). In parallel, spectrophotometric and ellipsometric measurements were also made to measure an increase of 1.88 to 2.05 and 0.04 to 0.16 of the refractive index and the coefficient at 550 nm respectively, correlating optical and electrochemical properties. With a microstructural characterization (XRD, RBS and ERD) of the films giving an Fm3m FCC structure and a composition of $\text{Ni}_{0.265}\text{O}_{0.53}\text{H}_{0.205}$ with a density of 3.55 g/cm^3 .

TABLE OF CONTENTS

ACKNOWLEDGEMENTS	III
RÉSUMÉ.....	IV
ABSTRACT	VI
TABLE OF CONTENTS	VIII
LIST OF TABLES	XI
LIST OF FIGURES.....	XII
LIST OF SYMBOLS AND ABBREVIATIONS.....	XVII
CHAPTER 1 INTRODUCTION.....	1
1.1 Chromogenic materials – optical functionalization of surfaces	1
1.1.1 Smart windows – glare and solar heat gain control	2
1.1.2 Future of the eyewear industry.....	5
1.2 Context of research.....	6
1.3 Objectives.....	7
1.4 Scientific publication.....	7
1.5 Thesis outline	8
CHAPTER 2 LITERATURE REVIEW AND THEORICAL BACKGROUND	9
2.1 Foreword	9
2.2 Electrochromism	9
2.2.1 Historical background	11
2.2.2 Tungsten oxide	12
2.2.3 Nickel oxide	15
2.2.4 All-solid-state electrochromic devices	19
CHAPTER 3 METHODOLOGY	27

3.1	Foreword	27
3.2	Fabrication methods	27
3.2.1	Substrate preparation	27
3.2.2	Thin film deposition by magnetron sputtering	33
3.2.3	Bias-assisted plasma etching	38
3.3	Optical characterization	39
3.3.1	Spectrophotometry	39
3.3.2	Spectroscopic ellipsometry	40
3.3.3	Modeling	43
3.4	Electrochemistry	46
3.4.1	Cyclic voltammetry	46
3.4.2	<i>In situ</i> spectroscopic transmission	48
3.5	Microstructural characterization	49
3.5.1	Scanning electron microscopy	49
3.5.2	X-ray diffraction	50
3.5.3	Ion beam analysis	51
CHAPTER 4 <i>IN SITU</i> SPECTROSCOPIC STUDY OF ELECTROCHROMIC NICKEL OXIDE FILMS		53
4.1	Foreword	53
4.2	Methodology	53
4.3	Optical properties	54
4.4	Electrochemical properties	60
4.5	Physical properties	67
CHAPTER 5 ALL-SOLID-STATE DEVICES DESIGN AND FABRICATION		71
5.1	Foreword	71

5.2	Device design and optimization	71
5.3	Fabrication and characterization	78
5.3.1	Filters deposited on the MAG-4 system.....	79
5.3.2	ASSDs deposited on the CMS-18 system.....	84
CHAPTER 6	CONCLUSION AND RECOMMANDATIONS	91
6.1	Summary	91
6.2	Perspectives	92
REFERENCES	97

LIST OF TABLES

Table 1-1: Conference proceeding.	8
Table 2-1 Property comparison of organic vs. inorganic EC materials.	9
Table 2-2 : Roles and possible materials of ASSDs.....	21
Table 3-1 : List of substrates used for the experiments.....	29
Table 3-2 : Magnetron sputtering systems used during the project.	33
Table 3-3: Deposition condition of the materials used for ASSD fabrication on the CMS-18.....	35
Table 3-4 : Optical oscillators used to obtain the optical properties of materials.	44
Table 3-5 : Parameters used for cyclic voltammetry procedures on NiO and WO ₃ films.	47
Table 4-1 : Deposition conditions of the nickel hydroxide films with maximized coloration efficiency deposited in the MAG-4 system.....	54
Table 4-2 : Optical and electrochemical results characterizing the EC performance of the NiOOH film through cycling.	62
Table 5-1 : Physical thicknesses of optimal modeled ASSD with their restrictions.....	77
Table 5-2 : Optical performance of the ASSD deposited on the MAG-4 system in comparison to the predicted modeled values.	81

LIST OF FIGURES

Figure 1-1 : (a) Human eye response, solar and thermal radiation of a black body at room temperature spectra, with the optical transmission of ideal coatings for hot and cold climate applications. Image taken from [8]. (b) Parts of a low-e coated window allowing to insulate the inside of a building from thermal radiation while transmitting solar heat from the outside. Image taken from [9].	3
Figure 1-2 : Ability to modulate visible transmittance vs SHGC of various chromogenic materials including thermochromic, electrochromic, suspended particles and gasochromic coatings. Passive windows such as a triple glazing unit (TGU) for hot climates and a double glazing unit (DGU) for cold climates are also indicated. Image taken from [11].	4
Figure 1-3 : Cross-section of a Visio-Rx lens showing the coating architecture of a modern lens. Image taken from [13].	5
Figure 2-1 Anodic and cathodic electrochromic oxides. All elements are transition metals. Image taken from [18].	10
Figure 2-2 Deb device architecture describing the first ASSD concept. Image adapted from [21].	12
Figure 2-3 : Tungsten oxide structure diagrams showing a) the ion diffusive hexagonal and triangular tunnels (Image taken from [76]) and b) the intercalated state (Image taken from [75]).	13
Figure 2-4 : Transition proportions depending on the intercalation level for WO_3 intercalated with Li^+ . Image taken from [25].	14
Figure 2-5 : Influence of a) oxygen (Image taken from [20]) and b) hydrogen (Image taken from [27]) on the optical properties of deposited nickel oxide films.	15
Figure 2-6 : Chemical evolution of nickel oxide crystallites when inserted into a KOH solution for cyclic voltammetry. Image taken from [29].	16
Figure 2-7 : $\beta\text{-Ni}(\text{OH})_2$ represented as a (a) unit cell projection and (b) ball and stick diagram. Ball color code is red O_2^- , grey Ni_2^+ and pink H^+ . The angle between the a and b axis is 120° , supposing a trigonal symmetry. Image taken from [27].	17

- Figure 2-8 : α -phase (right) / β -phase (left) junction showing the forces caused by water (blue and purple circles) inserted into the interlayer of α -Ni(OH)₂. Image taken from [30]. 18
- Figure 2-9 : Absorption coefficient of a Ni-V oxide film in its bleached and colored states. The inset shows a broad absorption peak in the colored state. Image taken from [20]. 18
- Figure 2-10 : Dispersion curves of NiOOH vs. Ni(OH)₂ corresponding to the colored and bleached states of the material. Image taken from [33], 19
- Figure 2-11 : Typical configurations of ASSDs. a) Composed of 2 substrates and laminated using a thick polymer electrolyte, as b) deposited onto a single substrate with a thin film electrolyte. Images inspired by [35]. 20
- Figure 2-12: Coloration and bleaching dynamics of an ASSD based on a lithium ions. Image taken from [38]. 22
- Figure 2-13 : Study of the degradation of the electrochromic properties over a large number of cycles of a WO₃/NiO ASSD using Li⁺ ions: a) shows the degradation during cyclic voltammetry measurements represented by b) the cathodic peaks, and by c) anodic peaks positions evolution. d) Shows the variation of the transmission at 550 nm and e) the charge capacity and its impact on η . Taken from [39]. 24
- Figure 2-14 : Transmission (top) and reflection (bottom) spectra in the visible and NIR a of a WO₃/ZrO₂/NiV_xO_yH_z ASSD in the colored and bleached states. Taken from [35]. 26
- Figure 3-1 : Examples of pin holes created by small particles. Top images show delamination of the coating due to nano-sized particles, while the bottom image displays a discontinuity caused by a micron size particle. Image taken from [42]. 28
- Figure 3-2 Pressure-enthalpy diagram of CO₂ and water. Right of CO₂'s supercritical point represents a gas fed source and the left part represents a liquid fed source. Taken from [48]. 31
- Figure 3-3 : Dynamics of the interaction between a surface and CO₂ particles. Figure a) shows the base mechanism involving CO₂ particles and gas stream interacting with particles. Figure b) shows the effect of the particle velocity on the surface deformation. Taken from [49]. 32

Figure 3-4 : Schematic representation of the fully automated CMS-18 sputtering system used during the project.	35
Figure 3-5 : Anders' modified structure zone diagram : The growth varies from a columnar microstructure (low E^* and T^*) to grain growth (high E^* and T^*). A region indentified as <i>ion etching zone</i> is observed at high E^* . Image taken from [52].	37
Figure 3-6 : AFM topography showing the effect of a 5 minute Ar plasma treatment at $V_B = -600$ V on the surface roughness of $\text{SiN}_x\text{:H}$ porous films: a) one layer, b) two-layer porous-dense stack and c) 13 layers porous-dense stack. Image taken from [53].	38
Figure 3-7 : Schematic of a Lambda 1050 spectrophotometer's functional parts. Image taken from [54].	40
Figure 3-8 : Ellipsometer base components. Image taken from [56].	41
Figure 3-9 : Schematic of the chemical cell used for cyclic voltammetry measurements attached to a RC2-XI ellipsometer.	42
Figure 3-10: Optical setup schematic for <i>in situ</i> spectroscopic transmission measurement during cyclic voltammetry procedures.	48
Figure 3-11 : Schematic of a typical scanning electron microscope. Image taken from [59].	49
Figure 3-12 : Schematic of an RBS/ERD measurement set-up. Image taken from [60].	51
Figure 4-1 : Spectrophotometric measurements of the NiOOH films in their colored and bleached states after the 30 th cycle.	55
Figure 4-2 : Ellipsometric measurements of the NiOOH films in colored and bleached states obtained between 45° and 70° for every 5° after the 30 st cycle.	55
Figure 4-3 : <i>In situ</i> transmission variation at 550 nm showing the evolution of the bleached and colored states over 30 cycles.	56
Figure 4-4 : <i>In situ</i> ellipsometric measurements at 550 nm showing the Ψ and Δ variation during coloration and over the 10 first cycles at an angle of 70°.	57
Figure 4-5 : Charge-dependent dispersion curves of NiOOH displaying the transition from bleached to colored states during the 10th cycle.	58

Figure 4-6 : Transmission spectra of water and lithium perchlorate from 300 to 2500 nm showing the absorption bands.....	59
Figure 4-7: Self-coloration effect observed in the transmission variation at 550 nm of a NiOOH film after charge insertion and removal from the electrochemical cell.....	60
Figure 4-8 : Voltammograms of the cycled NiOOH film showing an increase in charge transfer as well as a cathodic peak displacement over time.	61
Figure 4-9: Electrochemical and optical properties as a function of time of cycled NiOOH films aligned vertically showing the data synchronisation.....	63
Figure 4-10: Variation of the EC properties depending on the cathodic peak position. The top curve shows the inserted charge, middle curve the ratio between the bleached and colored transmission and the bottom curve the coloration efficiency.....	64
Figure 4-11: Refractive index (top) and extinction coefficient (bottom) variation as a function of inserted charge for the 10 th cycle shown at specific wavelengths.....	65
Figure 4-12: Thickness evolution during multiple cycles at the most colored and bleached states (left) and dynamic evolution of the thickness during the 10 th cycle (right).	66
Figure 4-13 : GIXRD diffractograms of NiO (190 nm) deposited on ITO (18 nm) in red and of the a masked region of the substrate containing only the ITO film in blue.	67
Figure 4-14 : Rutherford backscattering measurements made on a as deposited NiOOH film. No significant compositional variation was observed before and after cycling.	68
Figure 4-15 : Elastic recoil detection measurements of the NiOOH film showing the hydrogen content evolution before and after cycling.....	69
Figure 4-16: Number of intercalated hydrogen atoms compared to the number of intercalation sites for the first 10 cycles.	70
Figure 5-1 : a) adopted ASSD structure for b) reflection variation optimisation through coloration of the EC materials depending on their thicknesses (top SiO ₂ thickness equal to zero). c) Shows the modeled effect of the addition of a SiO ₂ layer on top of the device.....	72
Figure 5-2 : Resistivity variation of 100-nm-thick ITO films depending on the oxygen and hydrogen contents.	74

Figure 5-3 : Device patterning to optimize electrical properties and minimize the possibility of short circuits.	75
Figure 5-4 : Reflectance spectra of a modeled ASSD based on the thicknesses shown in Table 5-1. The full curve represents the bleached state (left axis) and the dashed curve the colored state (right axis).	78
Figure 5-5 : Modeled spectral transmission, reflection and absorption intensities of an ASSD fabricated in the MAG-4 going from a bleached state (blue) to a colored state (red).	80
Figure 5-6 : Coloration of an ASSD deposited in the MAG-4 system.	81
Figure 5-7 : SEM images showing an untreated NiO surface with large particles (~50 nm) (left) and defect free ion bombarded surface (right).	83
Figure 5-8 : Variation of the WO ₃ film thickness and roughness as a function of time under exposure to an argon plasma at 5 mTorr and -600 V bias as measured by <i>in situ</i> ellipsometry.	84
Figure 5-9 : Reflection, transmission and absorption in the visible area of a functional ASSD....	86
Figure 5-10 : ASSD based on one EC layer. a) adopted architecture of the device, and b) the resulting dispersion curves of the bleached and colored WO ₃	87
Figure 5-11 : SEM images of an ASSD following a CO ₂ snow cleaning treatment: a) and b) the cross section, c) and d) the surface.	88
Figure 5-12 : Effect of the cyclic voltammetry pre-intercalation process (a) on the optical transmission spectra (b).	89
Figure 6-1 : Suggested ASSD structure to effectively measure the coloration properties of each EC materials.	94
Figure 6-2 : Proposed architecture of a laminated ASSD composed of a Nafion (polymer) electrolyte and Mg ₄ Ni cathodic EC material. Imagen taken from [67].	95

LIST OF SYMBOLS AND ABBREVIATIONS

Abbreviations

AFM Atomic force microscopy

AR Anti-reflective

ASSD All-solid-state device

CAGR Compound annual growth rate

CE Counter electrode

CV Cyclic voltammetry

DC Direct current

DI De-ionized water

EC Electrochromic

EMA Effective medium approximation

LC Liquid crystal

FIR Far infrared spectrum

MSE Mean square error

NIR Near infrared spectrum

PCM Phase changing material

PSA Polarization state analyser

PSG Polarization state generator

QCM Quartz crystal microbalance

OT Optical thickness

RE Reference electrode

RF Radio frequency

SEM Scanning electron microscopy

SHGC	Solar heat gain coefficient
SCE	Saturated calomel electrode
SP	Suspended particles
UMA	Universal measurement accessory
VIS	Visible spectrum
WE	Working electrode
XRD	X-ray diffraction

Symbols

a -	Amorphous
A^+	Ion
A	Absorption
c -	Crystalline
e^-	Electron
k	Extinction coefficient
n	Refractive index
N	Carrier density
R	Reflection
T	Transmission
α -	Alpha phase
β -	Beta phase
γ -	Gamma phase
η	Coloration efficiency
μ	Carrier mobility
ρ	Resistivity

CHAPTER 1 INTRODUCTION

1.1 Chromogenic materials – optical functionalization of surfaces

Studying the evolution of the structural properties of solid materials submitted to changing temperatures, pressures and environmental conditions has preoccupied scientists for ages. One can think of the casting of bronze and controlling its properties through phase changes, or the evolution of carbon into diamond under extreme conditions. This precise control over the properties of materials has, therefore, allowed for the functionalization and adaptation of many structures and surfaces to our needs. However, most of these developed materials are passive, meaning that their properties are static and cannot be dynamically adjusted when needed. What happens, then, when the requirements of an application are time-dependent and would ideally need to be tuned?

This is where a particular class of materials, described as chromogenic, comes into play. Indeed, such materials display a color change upon the application of an external source of energy. The latter includes: temperature (thermochromic), an applied electric current (electrochromic - EC), incident light (photochromic), pressure (piezochromic), gaseous environment (gasochromic), and many others [1, 2].

The chromogenic materials market has seen a significant increase in the last few decades. For example, in the information display market, the advent of flexible screens on polymer substrates and electronic-paper has led to the introduction of various new materials providing variable colors, such as printable electrochromic paper from Acreo and Siemens [3]. While chromogenic materials only represent a small part of the display market, which is expected to reach a value of about \$190 billion by 2026, their contribution is expected to grow in the upcoming years [4].

One particular class of active materials is gaining in interest due to the possibilities it offers, its low energy consumption and durability. Indeed, since the first electrochromic-enhanced cathodic screens developed by Philips in the 1960's [2, 5, 6], many more sectors have found uses for these materials which offer adjustable optical properties and thus, variable transmission/reflection in the visible, NIR and IR spectrum. These include EC automotive car mirrors, sunroofs and aircraft passenger windows (Gentex [4]), architectural smart windows (View, Sage, etc.), and information displays [2]. In fact, the electrochromic glass market has a projected worth of about \$2.6 billion in 2020, with a compound annual growth rate (CAGR) of 12.3% [6]. The present work has

particularly been stimulated by the prospects of architectural and ophthalmic applications based on EC materials.

1.1.1 Smart windows – glare and solar heat gain control

The architectural glass and fenestration industry has, as one of their main purposes, the objective of maximizing the window surface on a building's envelope. In addition, current architectural trends for newly constructed buildings show very little brick/metal on their facades and are composed mainly of glass. Indeed, a study from the *Journal of Clinical Sleep Medicine* stated that, compared with a group of workers spending their day without sunlight, workers who have regular access to a window tend to be more physically active and have a longer and more restful sleep [7]. It is also no surprise, that with all the time spent indoors, people are trying to maximize their contact with the outside world. On the other hand, going all-glass makes it much harder to maintain a good insulation and, can therefore, lead to increased energy consumption. Research and development to improve the effectiveness of glass windows is thus critical.

The two main sources of energy transfer, in the present case, are the transmission of solar radiation (both visible (380 – 780 nm) and near-infrared (NIR) (780 – 2500 nm)) and thermal radiation (infrared – IR > 2500 nm) from outside and inside of a building. Normal windows made of glass transmit both the solar energy and thermal radiation (through absorption followed by blackbody re-emission). These characteristics lead to significant heat gains in the summertime and considerable heat losses in the wintertime, resulting in an increased demand on cooling and heating. A static widespread solution presently in use is to coat the glass with a thin layer of silver (~10 nm) which significantly increases the reflectivity of the glass in the IR thus lowering its emissivity and hence, the acronym low-e coatings. As a result, heat produced in the wintertime will be kept inside the building reducing heating costs. These coatings must, for obvious reasons, be kept transparent in the visible part of the spectrum, by adding antireflective coatings on either side of the silver film; although the amount of transmitted NIR solar energy can be tuned by adjusting the design of the low-e coating in accordance with the local climate conditions and to optimize energy gains. The required spectral properties as well as the glass unit function are detailed in Figure 1-1.

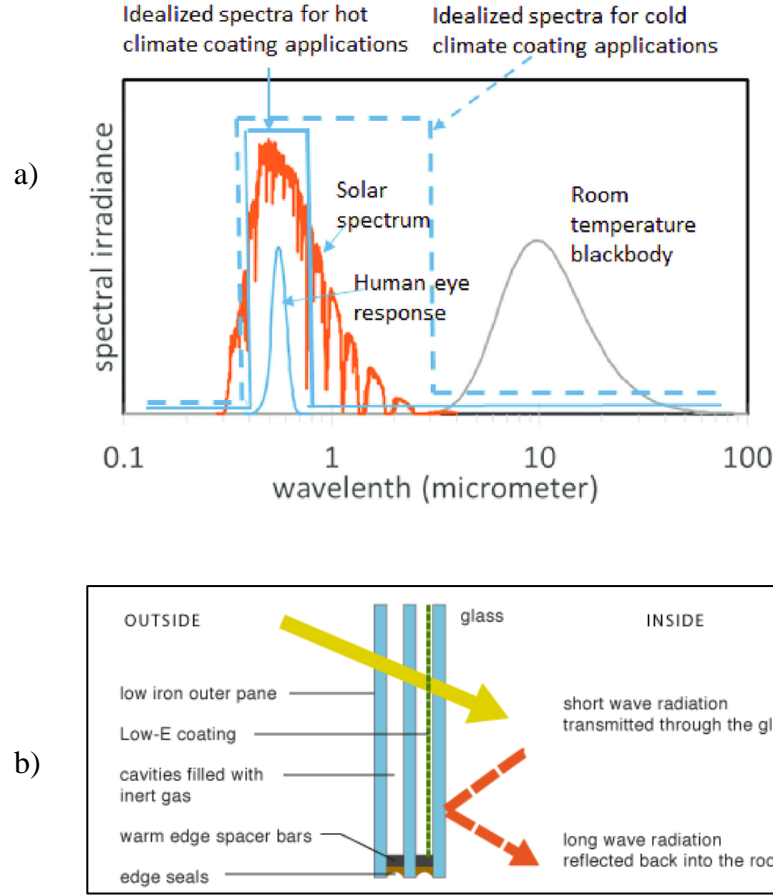


Figure 1-1 : (a) Human eye response, solar and thermal radiation of a black body at room temperature spectra, with the optical transmission of ideal coatings for hot and cold climate applications. Image taken from [8]. (b) Parts of a low-e coated window allowing to insulate the inside of a building from thermal radiation while transmitting solar heat from the outside. Image taken from [9].

As low-e coatings are static, their performance is limited in environments with significant seasonal changes. As such, the interest of chromogenic materials for architectural glass stems from the possibility of adjusting the visible and NIR transmittance (a.k.a, the solar heat gain coefficient SHGC), depending on the environmental conditions. The coefficient (T) is given by the equation below [10].

$$T = \frac{\int_{350\text{ nm}}^{2500\text{ nm}} T(\lambda)E(\lambda)d\lambda}{\int_{350\text{ nm}}^{2500\text{ nm}} E(\lambda)d\lambda} \quad 1-1$$

With $T(\lambda)$ the transmitted light and $E(\lambda)$ the ASTM solar irradiance, at specific wavelengths.

For instance, during summer, when it is warmer outside than inside, it is preferable to limit the solar heat gain (low SHGC). On the other hand, when it is colder outside during the winter season, a higher SHGC is needed to benefit from the sun's free energy.

Many chromogenic materials can be used to modulate the solar heat gain coefficient and, depending on their active spectral properties, better suited for specific climates. In Figure 1-2, the performance of various chromogenic materials is compared, specifically between thermochromic, electrochromic, suspended particles and gasochromic coatings.

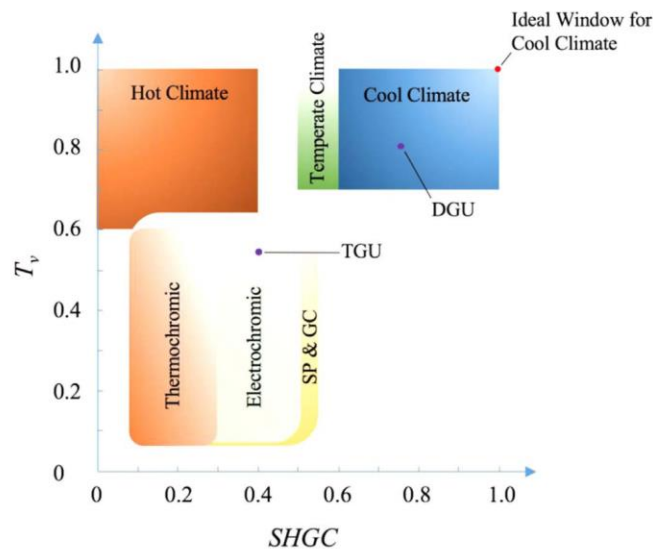


Figure 1-2 : Ability to modulate visible transmittance vs SHGC of various chromogenic materials including thermochromic, electrochromic, suspended particles and gasochromic coatings. Passive windows such as a triple glazing unit (TGU) for hot climates and a double glazing unit (DGU) for cold climates are also indicated. Image taken from [11].

In Figure 1-2, one can see that not all chromogenic materials are suited for every climate. For example, because of their high transition temperature, thermochromics have low efficiency in cold climates. With the different chromogenic materials from Figure 1-2 as well as with other active materials such as liquid crystals (LC) and phase changing materials (PCM), the concept of smart windows has been pushed forward [1, 2, 11]. However, smart windows, both thermochromic and electrochromic, still require fundamental research to help increase their environmental performance [12].

1.1.2 Future of the eyewear industry

Lenses and glasses can be, for some, their window to the world. Primarily a tool for vision correction, these lenses are also, nowadays, equipped with multiple functions, such as antireflective, scratch resistant, anti-fog, etc., making them more efficient for the wearer. In order to possess such properties, functional coatings must be added onto the lenses. A good example of a lens's multiscale and complex architecture is shown in Figure 1-3 (e.g.: the lens is in the 10^{-3} m range, the hard coat in the 10^{-6} m range and the top coating in the 10^{-8} m range).

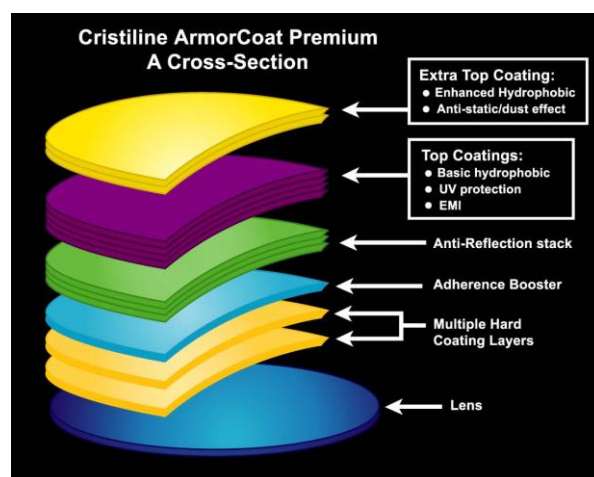


Figure 1-3 : Cross-section of a Visio-Rx lens showing the coating architecture of a modern lens.

Image taken from [13].

Multiple components of Figure 1-3 are studied and improved through material science and engineering research. In this thesis, the anti-reflection part is mainly of concern.

Among the chromogenic candidates, photochromic materials are already part of today's lenses. Glasses equipped with these materials are industrially produced, as people enjoy the possibility of maintaining their level of comfort and eye protection without having to change glasses when going outdoors. Lenses coated with spiropyran molecules [14] change color, as they pass from a transparent state to a colored state when exposed to UV light. This reaction changes the molecule's structure and makes it absorbing to visible light, and, when the exposure to the sun stops, thermodynamic equilibrium sets the structure back to its original form, making the lens transparent in the visible once again. The downsides of such materials are that the process of decoloration is quite long (tens of minutes), that the user has very limited control (e.g.: the lenses do not darken in

cars as the windows block UV light and the user cannot lighten them when desired) and that, overtime, when degraded, they tend to stay in a partly colored state.

The technology that is likely to surpass photochromic materials are the electrochromic materials. Indeed, they offer faster coloration/bleaching speeds (compared to photochromics), they are thinner (hundreds of nm vs. hundreds of μm) and controllable at the press of a button, and thus very well suited for lenswear.

1.2 Context of research

My journey at the Functional Coating and Surface Engineering Laboratory (FCSEL) began during the second year of my bachelor's program, in an internship on electrochromic materials coated on silver electrodes. I learned a lot during that summer and decided to extend my experience within a UPIR scholarship opportunity. Being surrounded by a strong team of experts, industrial partners as well as affiliated technicians, taking part in one of the largest industrial research Chairs in Canada was very stimulating.

Once I finished the bachelor's program, I decided to continue my studies with a master's program, and because of my previous experience, I put all my efforts into joining the FCSEL. As it so happened, a project, whose subject was close to that of my previous internship, was being planned by the group and its industrial partners. The project was based on the design and fabrication of an electrochromic-based device that would display a reflectivity variation, transitioning from an antireflective state to a more reflective state. The interest of such a device, for a lens supplier such as Essilor is clear, as a user would be able to use their glasses in a traditional manner when indoors or during the night, but would be able to switch to a sunglasses mode with the touch of a button as they went outside. The interest of Guardian, an architectural glass supplier, is also clear from the above discussion on smart windows (see section 1.1.1). As mentioned, devices based on suspended particles (SP) are already available, however they consume much more energy than EC materials, making them a less desirable choice for future innovations. As described in section 1.1.1, an EC device can be used on architectural glass for energy control, as well as for aesthetic purposes (color appearance). Thus, the whole project has been performed with an emphasis on the visible spectrum, but optical measurements over the whole solar spectrum were taken into account when possible.

It is also important to mention that prior work in the group had led to the establishment of this project. Dr. Bill Baloukas, Hubert Camirand, William Trottier-Lapointe, Francis Blanchard and Julien Gagnon all contributed to the development of electrochromic WO_3 coatings within the FCSEL, with the main focus on the processes and materials.

1.3 Objectives

To enhance our level of understanding of the optical behavior of all-solid-state electrochromic devices (ASSDs) and their fabrication and optimization, two main objectives were established:

1. To design, fabricate and characterize an all-solid-state electrochromic device (ASSD) for ophthalmic and architectural applications along four main criteria:
 - 1.1. The design must include an active behavior that presents anti-reflective and reflective properties depending on the state of the device.
 - 1.2. A reflection shift must follow, ideally giving rise to a 10% increase in reflection.
 - 1.3. Transmission must be at its highest and reflection at its lowest when in the bleached state, and vice versa when in the colored state.
 - 1.4. Absorption must be kept at a minimum in the bleached state.
2. Study in detail the coloration properties of nickel oxide. This objective is especially important for the optimization of the ASSD, as the knowledge of the optical performance of this material is rather limited in the literature.

Even if Objective 1 was the main instigator of this research, much emphasis was put on objective 2 as it was important to understand the material's behaviour to ensure the success of the device performance. Also, knowledge in both the literature and inside the group on NiO's optical properties was limited.

1.4 Scientific publication

Fabrication of the complete ASSD required implementation of both the cathodic EC material, namely tungsten oxide (WO_3), and the anodic material, nickel oxide (NiO). Their electrochemical and optical properties were studied by *in situ* spectroscopic ellipsometry during cyclic voltammetry (CV) measurements. During modeling of the ASSD, we found that the prediction of an appropriate

optical response of each material for a given coloration state was rather challenging, especially with respect to the characteristics of the NiO layers. That is why we devoted a considerable effort to further develop and validate a charge-dependent optical model of NiO's refractive index that would allow one to better predict the performance of the ASSD, as well as deepen our understanding of the phase-dependent optical properties of this material. The first results were presented at the Optical Interference Coatings (OIC) 2019 Topical Conference of the OSA in New Mexico, with an associated contribution to the proceedings (see Table 1-1).

Table 1-1: Conference proceeding.

L. Dubé-Riopel, B. Baloukas, O. Zabeida, L. Martinu, *In situ and Ex situ Spectroscopic Ellipsometry of Electrochromic NiO Films*, Optical Interference Coatings (OIC) Topical Conference 2019, OSA Technical Digest (Optical Society of America, 2019), paper ThC.6, New Mexico, June 2-9, 2019.

1.5 Thesis outline

Following the introduction in Chapter 1, Chapter 2 covers the theoretical background behind electrochromic ASSDs and their functionalities. As WO_3 was the main subject of multiple previous theses at the FCSEL, this thesis puts more emphasis on NiO. Following the theoretical background and the literature review, Chapter 3 gives an overview of the methodology used during the project, covering all aspects from fabrication to characterization and optimization of the ASSDs. Chapter 4 consists of a study that presents the dynamics of coloration of NiO through *ex situ* and *in situ* ellipsometry during cyclic voltammetry. Having access to this powerful tool of optical characterization, we were able to model the dispersion relations for the complex refractive index as a function of intercalation. With both electrochromic materials needed for the ASSD activation, NiO and WO_3 , modeled in all of their intermediate states going from fully bleached to fully colored, the results obtained for a complete ASSD are described in Chapter 5, including optical performance, modeling, as well as the importance of cleaning procedures to reduce the impact of short-circuits. Finally, Chapter 6 concludes the work, which was performed during the past two years, while discussing the completion of the original objectives and presenting suggestions for future research on EC devices.

CHAPTER 2 LITERATURE REVIEW AND THEORICAL BACKGROUND

2.1 Foreword

This section of the thesis first starts with a short historical background on the discovery of electrochromism and further development of this technology. Following is a short overview on the most popular studied materials displaying coloration upon electrical potential application. As mentioned in [5, 15], tungsten oxide (WO_3) has been studied rigorously in the group and in the community. Nickel oxide (NiO), on the other hand, possesses a more complex structure, which results in less documentation regarding its characteristics and behavior. Following the study of EC materials, a brief literature overview of ASSDs will be described.

2.2 Electrochromism

Some of the most widely studied and implemented chromogenic materials in research and development are EC, as they offer many advantages. Indeed, electrochromic materials present a reversible and controllable coloration following the insertion of both electrons and ions upon the application of an electrical potential, the latter inducing an electrochemical oxido-reduction reaction [5, 15]. The two main families of EC materials are organic and inorganic [16], both possessing advantages and disadvantages. Table 2-1 shows the differences between the two families.

Table 2-1 Property comparison of organic vs. inorganic EC materials.

	Organic	Inorganic
Materials	Organic compounds (C, H, N, R), Viologens	Transition metal oxides (see Figure 2-1)

Structure	Conducting polymers, metallopolymers, metallophthalocyanines [17]	Amorphous, polycrystalline, monocrystalline, nanocrystalline
Phase	Liquid or solid	Solid

Organic-based devices offer various spectral features, as the resonance bands can be tuned by the composition of the monomers. Plus, as they do not require costly or elaborate equipment, they are easily accessible, and they are flexible when deposited onto a polymer substrate. However, they tend to degrade faster than inorganic materials as they are often very sensitive to oxidization and UV light, making the fabrication more complex by the requirement of adding subsequent protective layers. The advantage of inorganic EC materials is their long-term durability and lower thicknesses. Plus, different applications can be targeted as they may be produced by several means (sol-gel, chemical vapor deposition, physical vapor deposition and more).

The present thesis focuses on inorganic semi-conducting materials as these materials were specifically targeted for the present application (see Section 1.1). Among all the known elements that can form an oxide only a select few present EC properties as shown in Figure 2-1.

ELECTROCHROMIC OXIDES:

H																			He
Li	Be																		
Na	Mg																		
K	Ca	Sc	Ti	V	Cr	Mn	Fe	Co	Ni	Cu	Zn	Ga	Ge	As	Se	Br	Kr		
Rb	Sr	Y	Zr	Nb	Mo	Tc	Ru	Rh	Pd	Ag	Cd	In	Sn	Sb	Te	I	Xe		
Cs	Ba	La	Hf	Ta	W	Re	Os	Ir	Pt	Au	Hg	Tl	Pb	Bi	Po	At	Rn		
Fr	Ra	Ac																	

Cathodic coloration

Anodic coloration

Figure 2-1 Anodic and cathodic electrochromic oxides. All elements are transition metals. Image taken from [18].

As many forms of oxides can be EC, their EC activity varies in terms of color change, activity, stability, etc. Furthermore, EC materials can be divided into two main categories: either they are labeled cathodic, in which case they color when intercalated with ions, or they are labeled anodic

and color upon ion extraction. One may note the special case of vanadium where, depending on the stoichiometry of its oxide, can be either cathodic or anodic. The most studied and implemented EC oxide is WO_3 , as it possesses a large color variation and coloration efficiency (η), displays different properties when amorphous or crystalline [19], can be cycled many times before losing its EC properties and other advantages. Indeed, the CE, η , is a metric often used to quantify the electrochromic performance of materials. Defined as the capacity of a material to change its optical density (ΔOC) as a function of the inserted charge density (Q [C/cm^2]) it can be expressed as follows:

$$\eta = \frac{\Delta OC}{Q} = \ln\left(\frac{T_b}{T_c}\right) / Q \text{ [cm}^2/\text{C}] \quad 2-1$$

The coloration efficiency values for inorganic EC materials are typically between 30-100 cm^2/C [20].

2.2.1 Historical background

To consider the evolution of our comprehension of electrochromism, one must go back to its first discovery. The first observation of an EC material was a dye composed of hexacyanoferrate called Prussian Blue, by Diesbach in 1704. At this time, people mainly used this dye for its dark blue color but had no knowledge of its active properties. It took until 1815 to observe an actual color changing effect, when Berzelius observed the appearance of blue following the application of a constant flow of hydrogen onto WO_3 , and 1824 for Wöhler to observe a change from pale yellow to blue during a chemical reduction of WO_3 in contact with a sodium-based metal. During the following century, no notable progress in ECs is documented, as the first reported electrochemical experiment was made in an unreported publication in 1953 (Liechtenstein), where a research group observed color variations of sodium tungsten bronzes under electrochemical treatments [5, 15].

During the 1960's, Deb published the first example of an all-solid-state EC-based device. Using hydrogen as the intercalation ions, obtained from the ambient humidity when water was dissociated following the application of a high voltage, the original published design is shown in Figure 2-2.

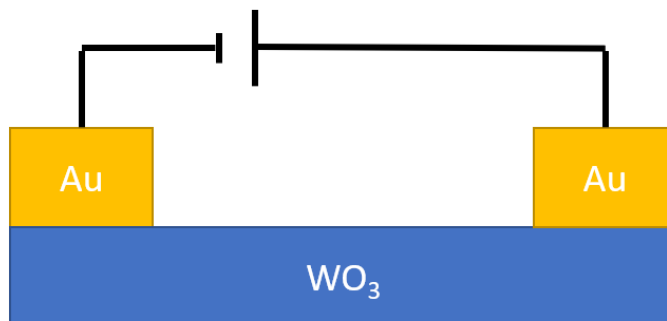


Figure 2-2 Deb device architecture describing the first ASSD concept. Image adapted from [21].

With one micron thick layers of WO_3 and gold electrodes, Deb observed a coloration when applying 1400 V on the electrodes. This type of device was ground-breaking in the field, but the optical and electrical performance were limited, as the coloration time was very long (half an hour) without a direct source of ions and obviously the applied potential was too high for any practical application. Nowadays, ASSDs are composed of more complex architectures, and will be discussed in more detail in Section 2.2.4.

2.2.2 Tungsten oxide

WO_3 has been studied for its electrochromic characteristics for almost two centuries. It has been the main subject of many studies, but despite this, its fundamental coloration mechanism is still under debate. This section gives a brief overview of its main characteristics and coloration and bleaching mechanisms.

The main simplified reaction responsible for the coloration of WO_3 involves ions (M^+) and electrons (e^-) inserted into $\alpha\text{-WO}_3$:



where x represents the intercalation ratio. Ions used in this reaction are typically H^+ and Li^+ [22].

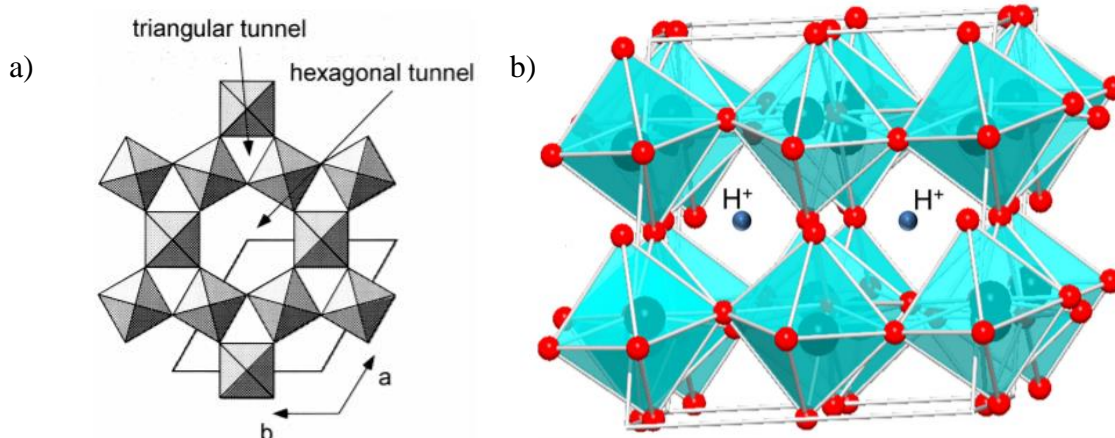


Figure 2-3 : Tungsten oxide structure diagrams showing a) the ion diffusive hexagonal and triangular tunnels (Image taken from [76]) and b) the intercalated state (Image taken from [75]).

From Figure 2-3, the spatial disposition of WO_3 lattices are detailed, as the ions (H^+ in this case) propagate in tunnels through the material to reach intercalation sites. Furthermore, one can associate Figure 2-3 b) to a perovskite crystal structure (AB_3). By corner-sharing the perovskite lattices form octahedra where ions can intercalate. When perfectly crystalline, no hexagonal tunnels are possible, making ion diffusion more limited. Amorphous and polycrystalline structures, on the other hand, possessing a less dense microstructure due to the presence of more channels, have been observed to keep an octahedron shape [23]. Another factor influencing the diffusion properties is the porosity of the material. As ions diffuse through inter-lattice tunnels, when a material is porous, more channels will be accessible than in a dense structure, granting access to more intercalation sites to carriers. In fact, it has been observed that the diffusion coefficient and the amount of inserted charge during cyclic voltammetry are proportional to the material's porosity [24].

$\alpha\text{-WO}_3$ has a localized electronic structure within octahedrons of W surrounded by six O ions. However, when intercalated, the added electrons that are injected into the structure are localized at specific positions and absorb at given energies through intervalence charge transfers between two metallic sites [20]. This charge transfer is the cause of the observed coloration, as the resulting transitions generate absorption in the visible spectrum. The possible transitions in the intercalated structure become $\text{W}^{6+}\text{-W}^{5+}$, $\text{W}^{6+}\text{-W}^{4+}$ and $\text{W}^{5+}\text{-W}^4$, whose individual energy levels result in different resonating frequencies [20].

Depending on the level of intercalation, the proportion of the three possible transitions varies, making the corresponding absorption vary as well. Berggren developed a theoretical model for this phenomenon, called the site-saturation model, correlating the absorption behavior with the intercalation level [25].

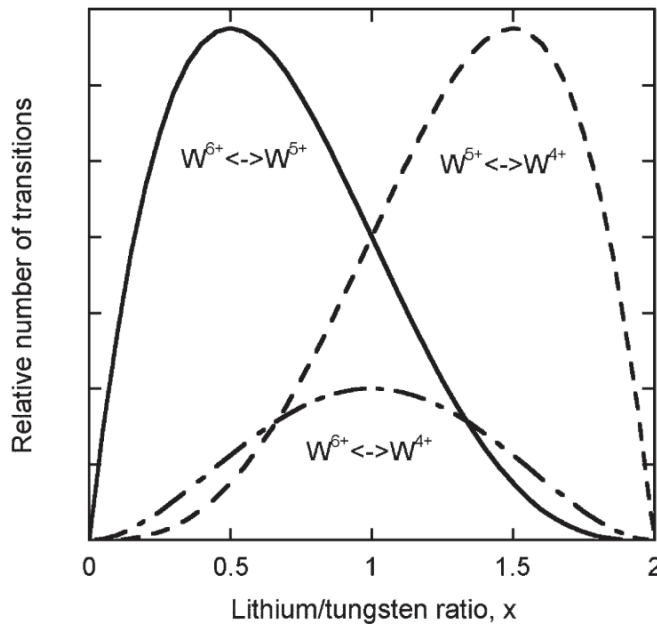


Figure 2-4 : Transition proportions depending on the intercalation level for WO_3 intercalated with Li^+ . Image taken from [25].

From Figure 2-4, as the intercalation level increases, the proportion of each possible transition varies. The expressions for each probable transition are given by the following equations:

$$\begin{aligned}
 P(W^{6+} \leftrightarrow W^{5+}) &= \frac{x(2-x)^3}{8} \\
 P(W^{6+} \leftrightarrow W^{4+}) &= \frac{x^2(2-x)^2}{16} \\
 P(W^{5+} \leftrightarrow W^{4+}) &= \frac{x^3(2-x)}{8}
 \end{aligned}
 \tag{2-3}$$

Thus, depending on the ion/tungsten ratio (proportional to the intercalation ratio), the coloration efficiency and its spectral behavior will vary, as the absorption coefficient variation is higher at low ratios and lower at high ratios, mainly because the absorption coefficient is higher for the $W^{6+} \leftrightarrow W^{5+}$ transition than the others. However, as it has been stated by Yamada *et al* [26], for most applications, the intercalation ratio is rarely higher than $x = 0.3-0.4$, limiting the electronic

transitions mainly to $W^{6+} \leftrightarrow W^{5+}$. It is also interesting to note that when highly saturated under a high voltage applied over a long duration, WO_3 shows an increased reflective behavior, as it starts to act as a metal due to the presence of free electrons.

2.2.3 Nickel oxide

Nickel oxide (NiO) is the most common anodic EC material, as it possesses a large color variation in the near-UV part of the spectrum going from a light yellow to dark brownish color. The major downsides of this material are that it tends to absorb even in its bleached state, and that, contrarily to WO_3 whose properties are relatively stable, it is much more sensitive to deposition conditions. Nickel oxide can possess multiple stoichiometries such as NiO and Ni_2O_3 , depending on the fabrication conditions. For magnetron sputtering applications, vanadium is typically added to decrease the magnetic properties of the Ni target which interfere with the magnetic field of the magnetron, in a Ni(93%)-V(7%) compound ratio.

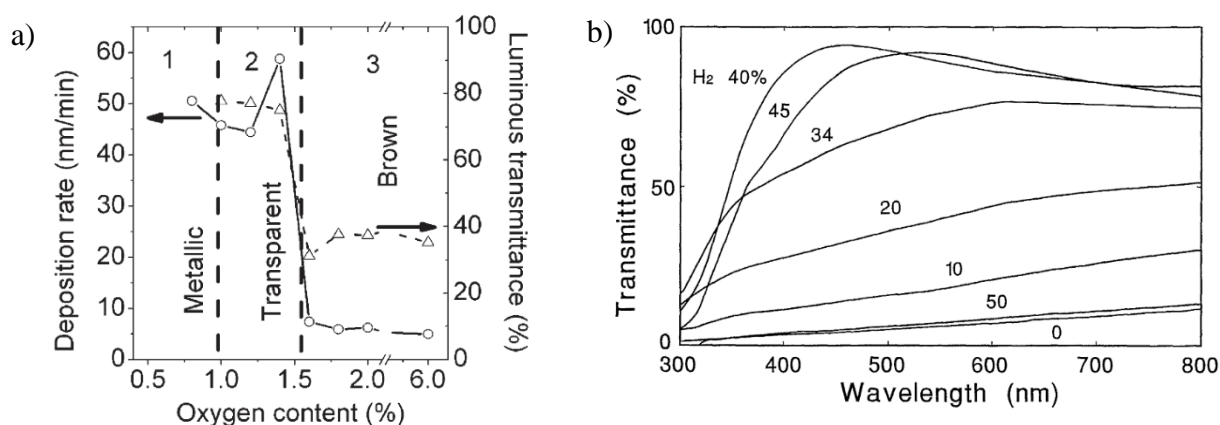


Figure 2-5 : Influence of a) oxygen (Image taken from [20]) and b) hydrogen (Image taken from [27]) on the optical properties of deposited nickel oxide films.

Figure 2-5 a), shows how the addition of too much oxygen can lead to the formation of a brownish much less transparent film. As NiO_x films are anodic, hydrogen is also often added to the gas mixture in order to pre-intercalate the film and render it more transparent (see Fig. 2-5 b)) and hydrated [27]. This transparency is key for EC activity, as it is directly correlated to the amount of inserted charges, suggesting that the plasma composition is a key fabrication parameter.

NiO films deposited at room temperature by magnetron sputtering methods show a mix between a crystalline and an amorphous structure. Such a structure has been described as short-range ordered by Ahn *et al.*, suggesting the formation of nanocrystals that share no orientation with neighbouring lattices, resulting in a quasi-amorphous material [28]. This short-range order effect causes an increase in EC activity in comparison to a fully polycrystalline NiO, as more crystallites are easily accessible to diffusing ions.

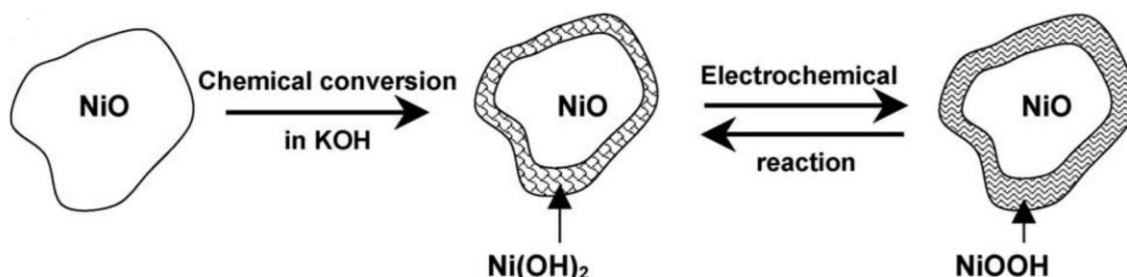
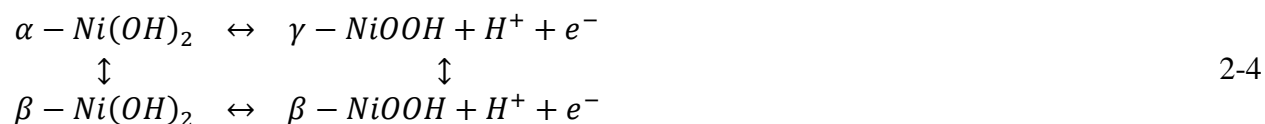


Figure 2-6 : Chemical evolution of nickel oxide crystallites when inserted into a KOH solution for cyclic voltammetry. Image taken from [29].

When inserted in KOH (aqueous solution used during electrochemical testing), oxygen and hydrogen bond with the structure at the surface of the crystallites, creating a NiO core with a Ni-hydroxide shell, as depicted in Figure 2-6. In this case the material is most often referred to as active nickel hydroxide when intercalated and to nickel oxyhydroxide when deintercalated). The equation below shows the various phase transitions depending on the water content (α - γ or β - β) and intercalation, taken from [20, 30].



Originally, when NiO is transformed into $\text{Ni}(\text{OH})_2$, H_2O molecules are located in the interplanar spaces. After a certain amount of time inside water or KOH, the H_2O molecules are extracted from the material due to tensile and compressive forces applied on the interplanar spaces, as the phase changes from α - $\text{Ni}(\text{OH})_2$ to β - $\text{Ni}(\text{OH})_2$ by a process labeled **ageing** [30]; correspondingly, the densities for these two phases vary from 2.6-2.8 $\text{g}\cdot\text{cm}^{-3}$ to 3.65-4.15 $\text{g}\cdot\text{cm}^{-3}$, respectively [20]. This pathway is reversible (beta to alpha), however this phenomenon occurs at specific temperatures (> 80°C partial recovery, >160 °C total recovery). The non-intercalated phases (right side of the

equations), *i.e.* γ -NiOOH and β -NiOOH are also linked via a pathway termed **overcharging**, occurring when a high negative voltage is applied to the film.

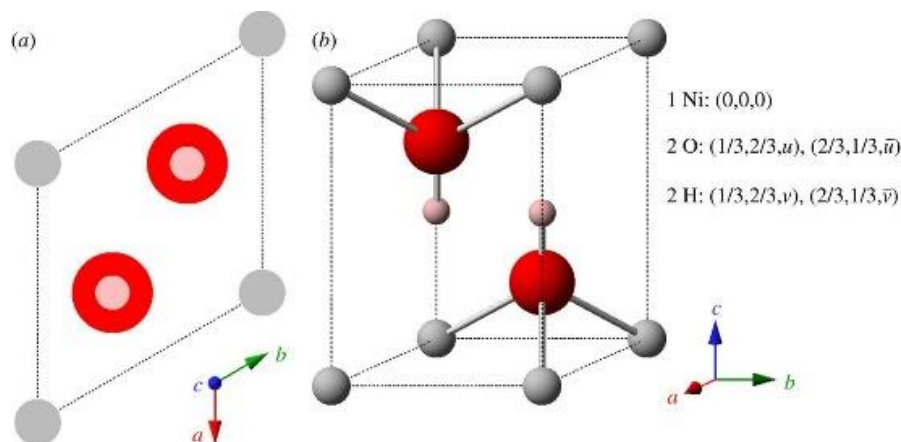


Figure 2-7 : β -Ni(OH)₂ represented as a (a) unit cell projection and (b) ball and stick diagram.

Ball color code is red O₂₋, grey Ni₂₊ and pink H⁺. The angle between the a and b axis is 120°, supposing a trigonal symmetry. Image taken from [27].

The cell represented in Figure 2-7 shows two layers of β -Ni(OH)₂ as in a brucite type structure. The space between the nickel atoms in the *ab* plane is the interlayer where water is inserted in the α -phase. Figure 2-8 shows the difference between the α - and β - phase, where water is extracted due to a combination of tensile and compressive forces, creating a “zipper” effect.

Aside from hydration/dehydration, ageing is the most studied phase change in the literature. Studies showing the effect on the optical and electrochemical properties have shown an increase in the EC properties (η) when ageing occurs [31]. Also, ageing induces an overall decrease of the film thickness, as shown by atomic force microscopy (AFM) [32], corresponding the water removed from the structure during phase transition toward a stable thermodynamic equilibrium, as shown in Figure 2-8.

The optical behavior of nickel hydroxide during coloration comes from the bandgap displacement from 3.6-3.9 eV (Ni(OH)₂) to 1.7-1.8 eV (NiOOH) as the band structure varies from a *n*-type to a

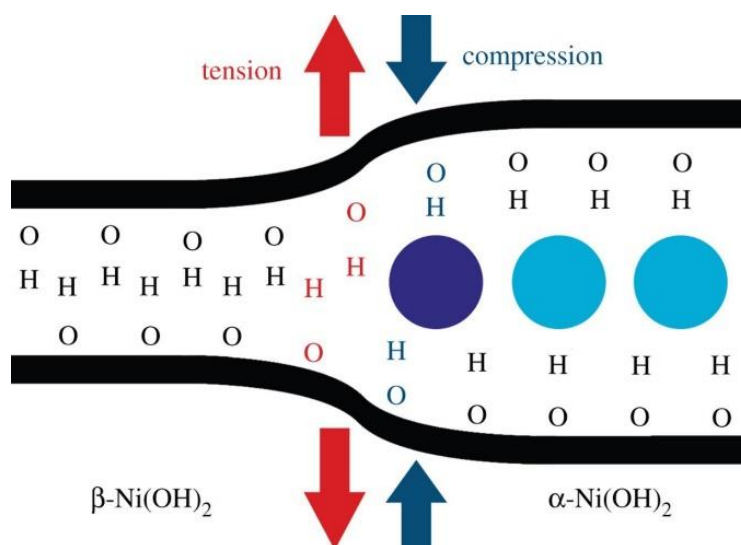


Figure 2-8 : α -phase (right) / β -phase (left) junction showing the forces caused by water (blue and purple circles) inserted into the interlayer of α -Ni(OH)₂. Image taken from [30].

p -type semiconductor. This band transformation comes from the charge transfer from Ni²⁺ to Ni³⁺ when protons are extracted [20].

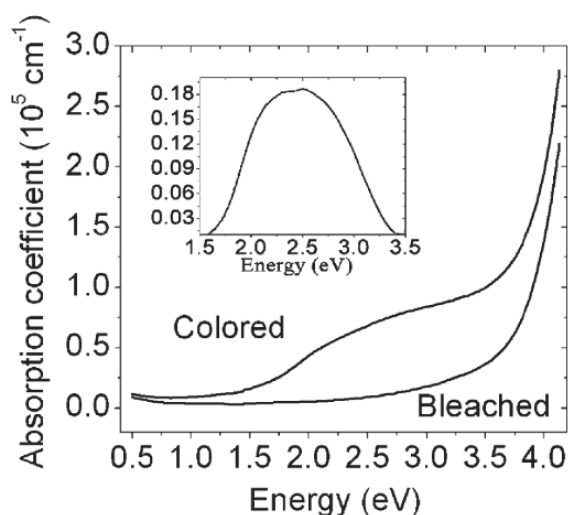


Figure 2-9 : Absorption coefficient of a Ni-V oxide film in its bleached and colored states. The inset shows a broad absorption peak in the colored state. Image taken from [20].

The band structure variation induced by proton intercalation affects the bandgap and consequently the absorption in the visible spectrum as observed in Figure 2-9. This variation in the optical

absorption is obviously synonymous with a variation in the refractive index and extinction coefficient of the material.

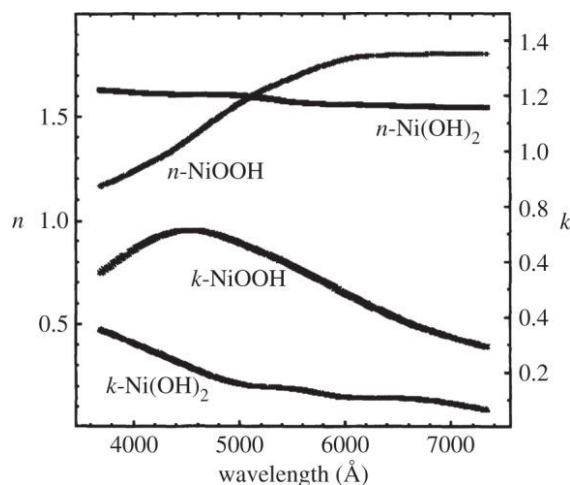


Figure 2-10 : Dispersion curves of NiOOH vs. Ni(OH)₂) corresponding to the colored and bleached states of the material. Image taken from [33],

Using spectroscopic ellipsometry measurements to model the dispersion properties of the NiOOH-Ni(OH)₂ reaction, Souza *et al.* established the coloration behavior of the film when treated in a chemical cell. The charge intercalation is correlated with an increase of the extinction coefficient (absorption) and to an increase of the refractive index above 500 nm and a decrease below 500 nm. When comparing the extinction coefficient with the absorption values from Figure 2-9, the same absorptive behavior is observed for wavelengths below 400 nm for the bleached state of the materials, suggesting that a fully transparent state of a nickel oxide film cannot be obtained.

2.2.4 All-solid-state electrochromic devices

EC devices based on inorganic materials are mostly composed of solid components, as mentioned in section 2.2, although some of them comprise a liquid electrolyte. Such devices can be referred to all-solid-state devices (ASSD). Two types of ASSD are mostly studied in the literature: those based on polymer electrolytes and those based on thin inorganic electrolytes. While both devices offer their own advantages/disadvantages, they operate on the same principle: coloration and bleaching result from applying an electrical potential on the top and bottom electrode, causing ionic diffusion within the device.

An ASSD based on a polymer electrolyte typically possesses a higher overall thickness due to the electrolyte, allowing a strong electronic insulation between both electrodes. The method usually used to fabricate such devices is to coat two different substrates with an electrode and an EC material, and to laminate the substrates along with the electrolyte to form a complete device (see for instance the devices produced by ChromoGenics [34]). This method is more complex than the inorganic-electrolyte devices which have been fabricated in a single sequence from a single substrate, but it offers more stability overtime, as the device is less subject to degradation compared to a thin film where cracks and defects occur more easily. On the other hand, an ASSD based on inorganic film is thinner and simpler to fabricate, as it can be all deposited on a substrate in a single fabrication process. In addition, as the electrolyte thickness is much lower, typically in the 100 to 300 nm range, the whole device is compatible with interference filter designs which require thicknesses of the order of the wavelength of interest (visible here). However, the use of much thinner electrolytes is often the source of short-circuits resulting in dysfunctional device [35].

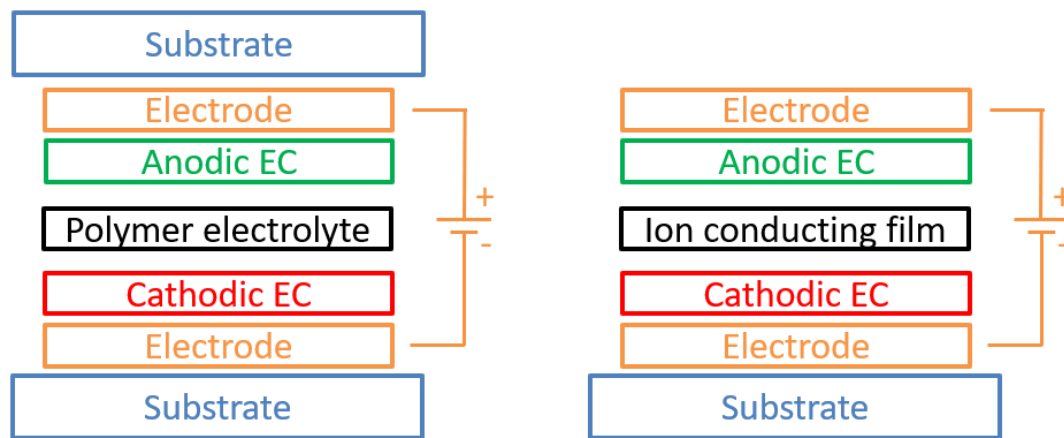


Figure 2-11 : Typical configurations of ASSDs. a) Composed of 2 substrates and laminated using a thick polymer electrolyte, as b) deposited onto a single substrate with a thin film electrolyte.

Images inspired by [35].

As shown in Figure 2-11, an ASSD has four different core components, excluding the substrate. Each component must fulfil its role to obtain a working active device. These functions are listed in Table 2-2. Exceptions to this architecture exist, as the electrolyte can also serve as an ion reservoir, removing one of the two EC layers. However, such devices show lower color variation, as they do not rely on the additive effect of using two EC materials (anodic and cathodic). In the case of NiO and WO₃ there is also the added benefit that the absorption spectra of both materials are

complementary, meaning that the brownish color of NiO and the bluish color of WO₃ result in a more neutral coloration.

Table 2-2 : Roles and possible materials of ASSDs.

Component	Functions	Possible material examples
Electrode	Allow the application of the driving potential and provide electrons to the underlying EC material	ITO, AZO, carbon nanotubes [36]
Anodic EC	Colored when non-intercalated / ion reservoir.	NiO , CoO, Mg ₄ Ni [37]
Electrolyte	Block electrons, conducts ions, ideally transparent	Ta ₂ O ₅ , SiO ₂ , ZrO ₂ , polymers
Cathodic EC	Colored when intercalated	WO₃ , MoO, VO ₂

To operate, the device itself must also be connected to a power source in order to apply a potential and drive electrons into the electrodes. When inserted, the e⁻ diffuse through the electrochromic layer populating intercalation sites. This electron accumulation causes an ion diffusion through the electrolyte to balance the charge. Depending on the polarity of the voltage, the electrons will either populate the top or the bottom EC/electrode duo. The presence of the electrolyte, which only allows the passage of ionic species (Li⁺, H⁺), results in a battery-like behaviour, as the electrons can only accumulate in a single EC layer at a time thus controlling where the ions intercalate.

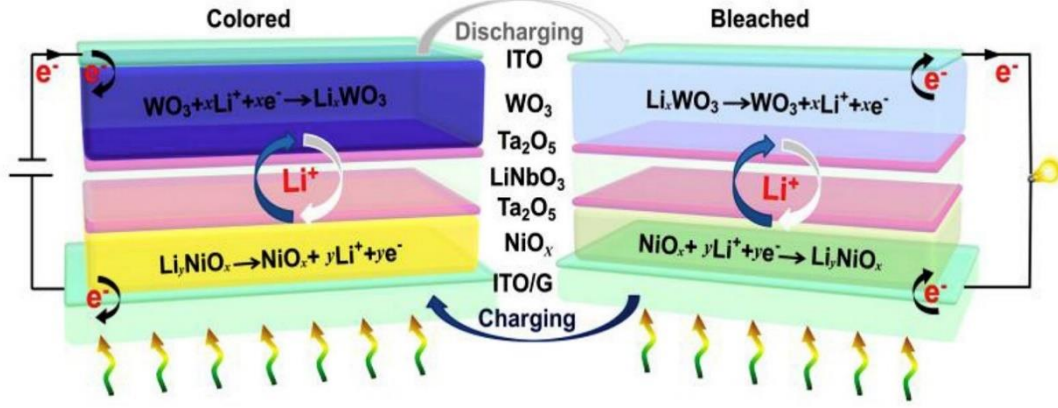


Figure 2-12: Coloration and bleaching dynamics of an ASSD based on a lithium ions. Image taken from [38].

The coloration dynamics, as shown in Figure 2-12, are based on charge displacement inside a device that colors or bleaches when intercalating specific layers (colors when intercalating the cathodic EC layer, bleaches in the anodic EC layer). The device's optical properties saturate after a certain amount of time upon a fixed voltage application, as the carrier population reaches a maximum. Different levels of intercalation can be obtained by removing the electrical potential at a specific time, yielding a specific coloration. When intercalated, after removing the potential, the charges remain in their respective layers, as a behavior known as memory effect. However, in a non ideal case (presence of imperfections) leak currents short-circuiting the electrolyte cause loss of coloration overtime. To solve the coloration loss happening after the potential removal, recurrent application of a potential (3 V for 5 seconds every few minutes for example) helps maintaining the device in the desired colored or bleached state.

The main parameters studied to characterize the performance of an ASSD, as taken from [5], are:

1. **Contrast ratio (CR):** This ratio quantifies the luminance of the brightest color against the darkest color.
 - a. For reflection: $CR = \left(\frac{R_0}{R_x}\right)$, where R_0 is the reflection of a standard perfectly scattering surface (non-shiny white card) and R_x the diffuse reflection of the ASSD.
 - b. For transmission: $CR = \left(\frac{T_b}{T_c}\right)$, where T_b is the bleached state transmission and T_c is the colored state transmission.

2. **Response time** (τ): The time required for a device to pass from a fully bleached state to a fully colored state. For most applications $\tau_b \neq \tau_c$. Thicker electrolytes (e.g.: polymer) cause higher response times (minutes), while thin film electrolytes offer a response time typically in the 10 s range.
3. **Write-erase efficiency**: The amount of coloration that can be subsequently bleached back or vice versa. To be successful in terms of repeatability, an ASSD must have the highest possible efficiency.
4. **Cycle life**: Number of cycles before a device shows significant degradation.
5. **Coloration efficiency** (η): Transmission variation divided by the amount of inserted charges, as defined in section 2.2 ($\eta = \frac{\Delta OC}{Q}$).

The evolution of the device properties over time is of interest, as degradation causes loss of performances. The main identified failures are short-circuiting increasing over time and trapping (mainly in the context of Li^+ ions) and will be discussed and studied in this thesis.

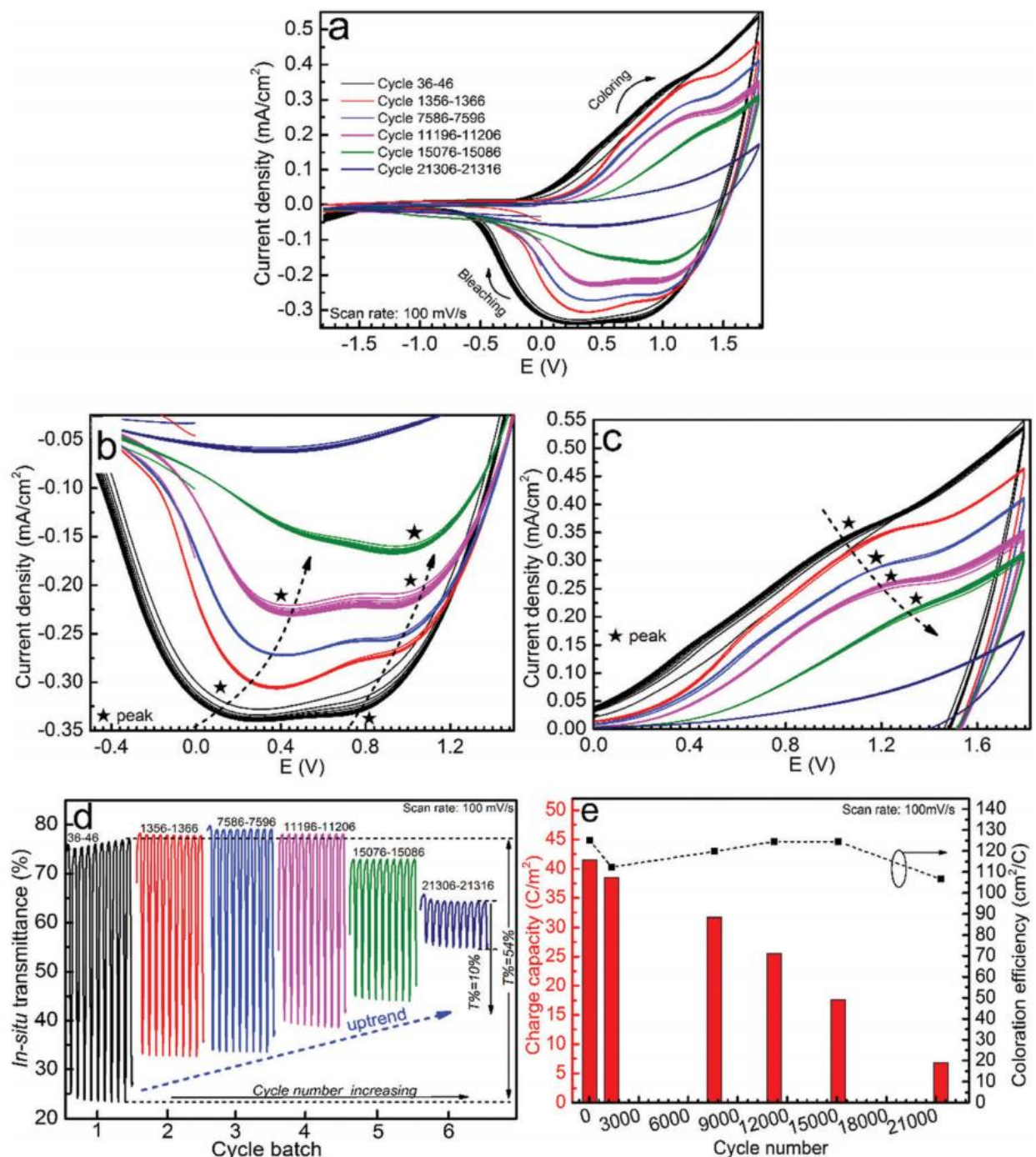


Figure 2-13 : Study of the degradation of the electrochromic properties over a large number of cycles of a WO_3/NiO ASSD using Li^+ ions: a) shows the degradation during cyclic voltammetry measurements represented by b) the cathodic peaks, and by c) anodic peaks positions evolution. d) Shows the variation of the transmission at 550 nm and e) the charge capacity and its impact on η . Taken from [39].

The study by Dong *et al.* summarized in Figure 2-13 shows the effect of degradation on the EC properties of a ITO | WO₃ | lithiated polymer | NiO | ITO device. More precisely, the charge inserted (area of the voltammograms) and transmission variation diminishes over time, decreasing the ability of the device to change color. Six ranges of 10 cycles have been studied, at different stages of the cycling process which lasted 21 280 cycles. As both the level of coloration and the amount of charges in play diminish, the coloration efficiency stays relatively stable, as it is proportional to the ratio of these two parameters. The main reason for the observed degradation is ion trapping in the NiO and WO₃ layers, which results in the permanent coloration of the device. However, a study by Wen *et al.* showed that EC materials can be “rejuvenated” by applying a high galvanostatic potential to the layer in order to remove trapped Li⁺ ions [40], suggesting a possible solution to stop or slow down ASSD deterioration. Note however, that this has only been applied to single layers in liquid environments and that it has yet to be applied to ASSDs.

It is interesting to look at the coloration and bleaching properties of a typical device as a function of wavelength. Indeed, as the optical properties of the EC materials are varied through intercalation the Fresnel coefficients in transmission and reflection in the visible region will change accordingly. A study by Granqvist *et al.* in 2004 measured the variation in transmission and reflection for the whole solar spectrum (see Figure 2-14).

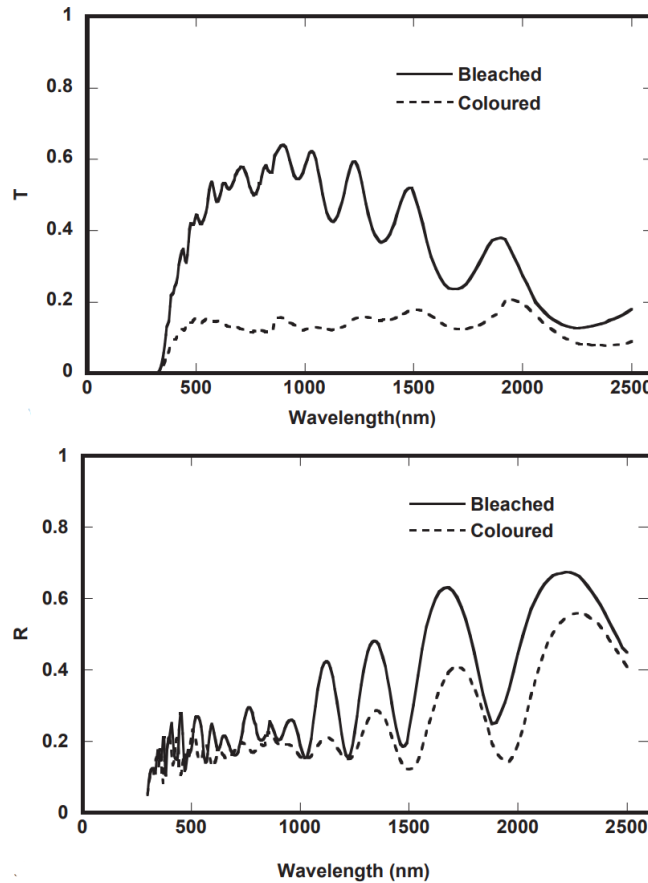


Figure 2-14 : Transmission (top) and reflection (bottom) spectra in the visible and NIR of a $\text{WO}_3|\text{ZrO}_2|\text{NiV}_x\text{O}_y\text{H}_z$ ASSD in the colored and bleached states. Taken from [35].

The behavior observed in Figure 2-14 shows a large decrease of the transmission upon coloration, while the reflection is seen to also decrease but to a much lower extent most especially in the visible. This is important to note as one of the objectives of the present project is to generate an increase of at least 10% upon coloration. Furthermore, one can observe the presence of a significant amount of interference fringes (oscillations) in the spectra which are related to the total optical thickness of the device ($\text{thickness} \times \text{refractive index}$).

By tuning each layer's thickness, it is thus possible to create optical filters such as reflectors, anti-reflective (AR) coatings, band-pass filters, etc. The project's first objective (see section 1.3) is therefore to fine tune the layer thicknesses of the ASSD to obtain an antireflective effect in the bleached state which, if designed appropriately would lead to an increase in reflection upon coloration.

CHAPTER 3 METHODOLOGY

3.1 Foreword

This section covers the various methods used during the project to fabricate the EC thin film systems and characterize their properties and performance. The applied methods and methodologies were inspired by previously developed approaches at the FCSEL, however, many of them have been adjusted and updated for the specific case of ASSDs.

This chapter is divided into sections pertaining to the preparation and fabrication of the films as well as their electrochemical and optical characterization. Additional physical characterization techniques are also described, as they were used for the analysis of the NiO layers explored in more detail in Chapter 4.

3.2 Fabrication methods

ASSDs can be fabricated through various techniques (electrodeposition, sol-gel, chemical vapor deposition, evaporation, sputtering, etc.), all having their own advantages/disadvantages [41]. The quality of the produced layers (presence of contaminants, crystallinity, stoichiometry), deposition rate and associated operation costs, thickness precision, etc. are all factors to consider when choosing the most appropriate path for such a project. We chose magnetron sputtering, not only because the FCSEL possesses such systems and a large expertise, but also because the quality of the produced films and its high precision and repeatability are best suited for the fabrication of an ASSD where the control of the thickness of individual layers is critical in order to satisfy the optical requirements of an antireflection filter. In the following section, film fabrication and surface treatments are addressed.

3.2.1 Substrate preparation

The substrate's surface state before thin film deposition has a critical impact on the growth of a thin film. Nano-defects (10-100 nm) impact the adatom surface mobility, whereas micro-defects ($> 1 \mu\text{m}$) cause discontinuities and shadowing effects in the film. Such contamination is one of the main obstacles in this work, as it results in short-circuits in the fabricated devices. Since the work

is performed in a non-cleanroom environment, the solution to reduce the presence of these particles is to use an appropriate cleaning method during the substrate preparation.

3.2.1.1 Short-circuit studies

As mentioned in section 2.2.4, short-circuits through the electrolyte are often responsible for malfunctioning of the devices. The factors causing these shorts come from various possible sources, but pin holes, created by small particles, have been identified as the main culprit. These particles often come from ambient dust, are created during the fabrication process, or consist in process residues. The generated pinholes are generally due to one of the two following phenomena: (i) complete delamination of specific regions caused by nano-sized particles, or (ii) resulting from the shadowing effects generated by micro particles, as shown in Figure 3-1. Both effects can lead to the direct contact of the top and bottom electrodes.

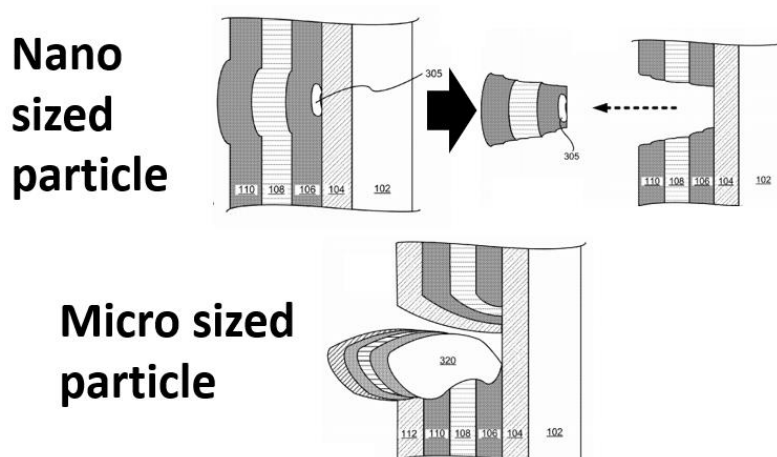


Figure 3-1 : Examples of pin holes created by small particles. Top images show delamination of the coating due to nano-sized particles, while the bottom image displays a discontinuity caused by a micron size particle. Image taken from [42].

Other phenomena can also be responsible for short circuits, such as a direct contact between the electrodes at the edges of the device, or a poorly insulating electrolyte. In order to obtain a fully functional device and increase the yield during the production of EC devices, a few methods have also been developed to palliate the short-circuits problem; this includes isolating pin holes [43] or the center of a device from its edges [44] by using a combination of laser ablation and thermal imaging monitoring. Indeed, as short circuits generate heat due to high current densities, they can

be detected with a thermal camera, and then isolated by etching small circles around them. Clean room environments have also been proven to help [45], as significantly less particles are transferred during the various fabrication steps. Access to these methods was however limited in the present project, in addition to considering our industrial partners who favored a fabrication process with minimized complexity. Different approaches were thus implemented to reduce short circuits such as edge isolation by plasma etching (section 3.2.3) and the implementation of a CO₂ snow cleaning procedure (section 3.2.1.3).

3.2.1.2 Cleaning and patterning

Multiple types of substrates were used during the project and each of them had their specific utility. Table 3-1 provides a list of each substrate, its role and expected results.

Table 3-1 : List of substrates used for the experiments.

Substrate	Role	Thickness
B270 glass	Common substrate for optical characterization.	2 mm
c-Si	Optical characterization of all materials as it displays a good optical contrast with most dielectrics. Transmission measurements are however not possible in the visible spectrum.	0.3 mm
ITO-coated glass	Substrate coated with conductive ITO thin film for ASSD and EC materials.	0.7 – 1.1 mm
ORMA polymer	Material of choice for Essilor lenses	2 – 3 mm

The choice of substrate is also of importance as it has an impact on the material growth and correspondingly the optical and electrochromic properties.

As previously mentioned and, as observed throughout the project, the most critical part during the sample preparation prior to the deposition of ASSDs is the removal of particles present on the

surface of the ITO electrodes as they can give rise to short circuits. As a result, quite a few approaches were implemented and tested. These methods are listed below.

Method 1: Soap cleaning

The quickest cleaning method that yields a surface free of defects is washing the substrate in soapy water. The method consists in scrubbing the surface with soap, rinsing it with deionized (DI) water and drying it with a nitrogen flow. An optional rinsing in isopropanol followed by deionized water before drying is possible, as it removes most solvent traces.

Method 2: Ultrasonic bath

One of the most efficient methods widely used in surface treatments is cleaning with an ultrasonic bath. The generated acoustic waves mechanically remove physisorbed particles, and, when submerged in an appropriate solvent, chemisorbed species can also be removed. The typical method is to submerge the sample in an acetone ultrasonic bath for 10 minutes, followed by an isopropanol bath for another 10 minutes. After the treatment, the sample is rinsed with DI water and dried with a nitrogen flow.

Method 3: CO₂ snow cleaning

A novel cleaning method introduced in our laboratory is based on spraying cold (-20°C to -50°C) solid CO₂ particles. To do so, the substrate is first mounted onto a heat plate set at 50°C to avoid water condensation upon exposure to the CO₂ snow. The sample is then exposed to a CO₂ solid particle flow using a raster motion starting from the edge nearest the user towards the outer edge of the sample. This ensures that the ejected particles are not redeposited onto the sample. The last step is to dry the sample and remove residual water with a nitrogen flow.

Method 2 is widely used to eliminate the presence of chemisorbed substances and particles to improve the adhesion between the substrate and the coatings. For example, this is of importance in the context of thick hard protective coatings deposited onto metallic substrates. In the context of optical coatings, where layer thicknesses are typically much lower, method 1 is most often sufficient, as soap cleaning is enough to remove most particles which could generate optical defects visible to the naked eye. However, in particular cases where defects are affecting the coatings integrity, which is the case for EC devices, method 3 is preferred, as this technique removes more particles than the other methods.

3.2.1.3 CO₂ snow cleaning

As previously mentioned, a novel cleaning method, based on CO₂ snow particles, was adopted to easily remove both physisorbed and chemisorbed particles. This approach was indeed mentioned in patents related to ASSD fabrication and short circuit reduction [46]. As the name suggests, liquid or gas CO₂ is converted into solid particles using a nozzle that rapidly reduces the fluid's pressure, resulting in a rapid expansion.

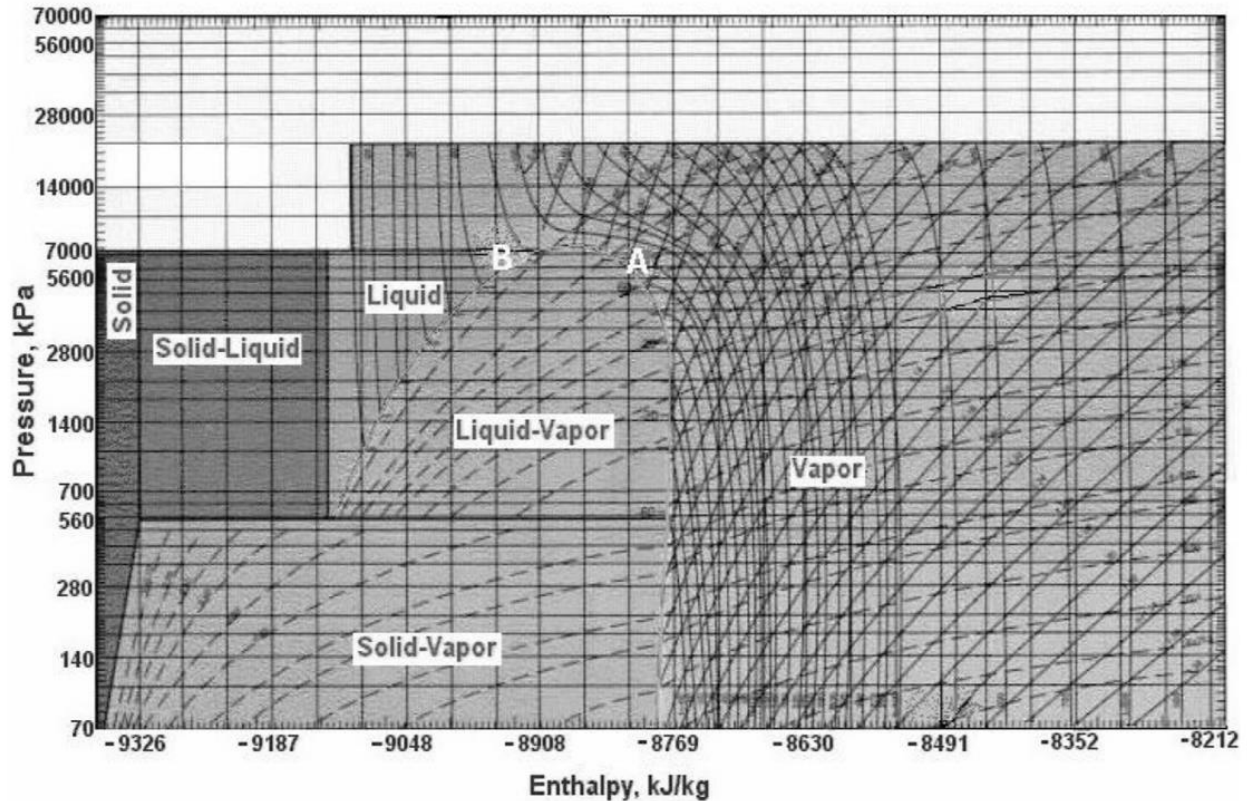


Figure 3-2 Pressure-enthalpy diagram of CO₂ and water. Right of CO₂'s supercritical point represents a gas fed source and the left part represents a liquid fed source. Taken from [47].

From Figure 3-2, it is possible to see the pressure dependence of the three different phases of CO₂ as a function of temperature. A nozzle is designed to maximize the drop in pressure at constant enthalpy, creating an adiabatic expansion. As the pressure drops rapidly, a phase transformation occurs, as solid particles are forming when the pressure reaches below the 560 kPa line. When using a gas source of CO₂ (right of CO₂'s supercritical point in Fig. 3-3), the gas is converted into liquid through droplet nucleation, and below 560 kPa part of the liquid turns to a solid; 6% of dry

ice in the present case. When starting from a liquid source (left of CO₂'s supercritical point in Fig. 3-3), the phase changes from liquid to gas to solid, and the yield goes up to 45% of dry ice.

The flow coming out of the nozzle is then a combination of gas, solid and liquid CO₂ with a high velocity (up to 100 m/s). However, as the gas stream velocity is largely reduced after a short distance (cm), the usage of a CO₂ flow is best at close range (2-3 cm from the surface).

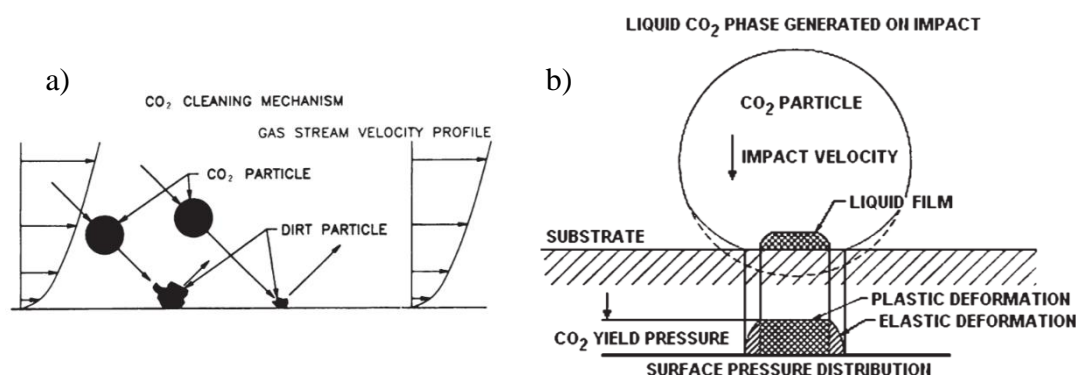


Figure 3-3 : Dynamics of the interaction between a surface and CO₂ particles. Figure a) shows the base mechanism involving CO₂ particles and gas stream interacting with particles. Figure b) shows the effect of the particle velocity on the surface deformation. Taken from [49].

Three main mechanisms are involved when cleaning a surface with a CO₂ flow. The first occurs when a solid particle of CO₂ interacts with the surface, as it sublimates, and its volume increases by approximately 800 times [47]. This phenomenon causes a high pressure on the surface due to momentum transfer, and a mechanical shock wave is created at the impact zone due to sublimation. These waves are thus responsible for the dislodging of particles on the surface. The second mechanism is due to the gas flow which creates an aerodynamical drag on the surface's particles. Being proportional to the particle's area, the drag effect mostly removes larger particles, while the ice removes smaller particles. A third phenomenon, seen in Figure 3-3 b), occurs when a liquid film is created at the interface between the CO₂ particle and the substrate. This film acts as a solvent and dissolves organic species chemisorbed at the surface, such as hydrocarbons. Plus, with a liquid CO₂ source, a freeze – fracture effect is created at the surface and non-dissolving compounds such as silicones, fluorinated compounds and pump oils can also be removed.

With a proper ventilation system, such cleaning mechanisms have been proven to be useful in several sectors, such as telescope mirror cleaning and MEMS surface preparation. Several studies

(AFM, SEM, optical microscope) have shown complete removal of dust, grease and even marker marks on Si wafers [48].

3.2.2 Thin film deposition by magnetron sputtering

Magnetron sputtering is a widely used tool for fabricating thin films (nanometer scale) in the industry, such as hard drives, semiconductors, glasses, solar cells and many more. Compared to other physical vapor deposition (PVD) techniques, magnetron sputtering offers a high deposition rate ($\sim 1\text{-}10 \text{ \AA/s}$) while maintaining a good precision on thickness control (nanometer) and also allows for the deposition of various compounds (oxides, nitrides) in a straightforward manner. In addition, as the technique relies on sputtering, the technique doesn't require melting of a material, allowing a larger variety of compounds to be created, a plus compared to evaporation techniques [49].

During this project, two deposition systems were used to fabricate different components of the ASSDs. The characteristics of the sputtering systems are detailed in Table 3-2, namely the CMS-18 UHV apparatus from Kurt J. Lesker, and the home-made MAG-4 four-magnetron high vacuum sputtering apparatus.

Table 3-2 : Magnetron sputtering systems used during the project.

Component	System	
	MAG-4	CMS-18
Power supply (W)	150 (RF)	450 (RF and DC)
Number of magnetrons / Target diameter (inch)	4 / 2	4 / 3
Chamber volume (L)	25	80
Control systems	<ul style="list-style-type: none"> PID-controlled butterfly valve for pressure 	<ul style="list-style-type: none"> Fully automated. Equipped with load-lock for sample transfer.

	control. Manual operation.	
Pumping system	Turbomolecular pump supported by a mechanical pump	
Base pressure (Torr)	2×10^{-6}	8×10^{-8}
Thickness monitoring	Time control	<i>In situ</i> ellipsometer

The following target materials were used:

- **Ceramic targets:** SiO₂, ITO, WO₃.
- **Metallic targets:** W, Ta, Ni(93%)-V(7%), Si.

Controlling the layer thickness was important to deposit devices with a predesigned optical performance. To achieve a nanometer-scale thickness control, two methods were used. The first method of predicting the thickness was a simple time monitoring, assuming a stable deposition rate. However, this was often insufficient due to non-linearity in the deposition rate, leading to occasional mismatches. A higher accuracy was achieved within the CMS-18 system equipped with *in situ* ellipsometry (M-2000 from J.A. Woollam).

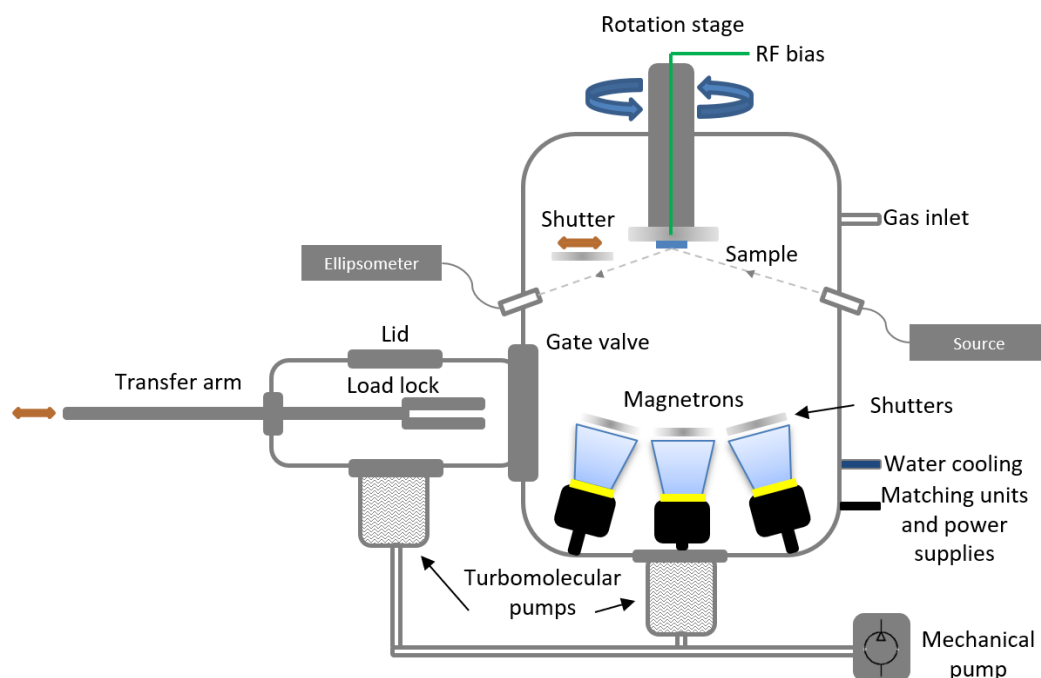


Figure 3-4 : Schematic representation of the fully automated CMS-18 sputtering system used during the project.

Figure 3-4 shows a schematic representation of the CMS-18. Two parts are particularly important in the context of the present work: the main chamber and the load lock. Both have their own turbomolecular pump to maintain the vacuum. The procedure starts by inserting the sample into the load lock, as it serves as an intermediate transfer point between the ambient air and the main vacuum chamber, thus decreasing the time required to obtain a sufficiently low base pressure before deposition as well as decreasing the presence of contaminants. Using the transfer arm, the sample is then mounted onto the rotation stage and the deposition sequence is ready to start.

Table 3-3: Deposition condition of the materials used for ASSD fabrication on the CMS-18.

Role	Material	Gas proportion (%)			Power Density (W/cm ²)	Pressure (mTorr)
		Ar	O ₂	H ₂		
Electrode	ITO	100	0	0	2.19	5
EC layer	NiO	35	3.5	26	9.87	10

	WO ₃	40	20	40	9.87	14
Electrolyte/Filter	SiO ₂	77	23	0	9.87	5
	Ta ₂ O ₅	50	50	0	9.87	20

The deposition condition displayed in Table 3-3 were used to fabricate the devices that are discussed in Chapter 5. During the deposition of the filters, the substrate holder was fixed to monitor *in situ* the growth with ellipsometry.

Sputtering is a thin film fabrication technique that allows growth by bombarding a target material with a reactive (oxygen, hydrogen, nitrogen, etc.) or non-reactive (argon) plasma, where the collision ejects the target's atoms towards a substrate, creating a growth with a rate in the nanometer per second on the surface. To do so, gas is injected into a high vacuum chamber (typically below 10^{-5} Torr to avoid contamination) and ionised under an electrical potential between the anode (ground) and the cathode (sputtering target), that can vary between sixty to hundreds of volts. Under the generated field, the electrical force accelerates the ions toward the target. This technique, called direct current (DC) sputtering, is useful when using metallic targets, but cannot be used on dielectric targets. In this project, the radio frequency (RF) sputtering method was adopted in order to use ceramic targets (Silica and ITO), where alternating electrical potential is applied between the plasma and the target, avoiding charge buildup that could damage the ceramics.

The collision between the ionized species and the target material results in two phenomena: in the first one, atoms are ejected through a momentum transfer, that are themselves projected towards the substrate, with a specific flux corresponding to the deposition rate. The second is the ejection of secondary electrons (according to the Townsend's and Paschen's laws), which are accelerated towards the plasma due to the potential between the cathode and the anode, which contribute to maintaining the plasma discharge. Nowadays, most systems are equipped with a magnetron that confines the plasma close to the target with a strong magnetic field orthogonal to the surface, confining the electrons and thus creating a high plasma density near the target, therefore increasing the deposition rate. This whole process must be performed under vacuum to increase the mean free path between ions, reducing the number of collisions, therefore not interacting with the incoming atoms after their "flight" between the target and the substrate. When the pressure is too low (less than 1 mTorr) or too high (more than 100 mTorr), the deposition rate drops rapidly and the

discharge becomes unstable, as the potential needed to ionize too far apart (too high mean free path) or too many atoms (too low mean free path) during the discharge would be too high [50].

Under vacuum, accelerated ions towards the substrate holder can cause multiple effects, such as material growth of multiple phases or resputtering of the deposited film. In the structure zone diagram (SZD) (see Figure 3-5), the conditions to obtain specific structures (or etching) are detailed.

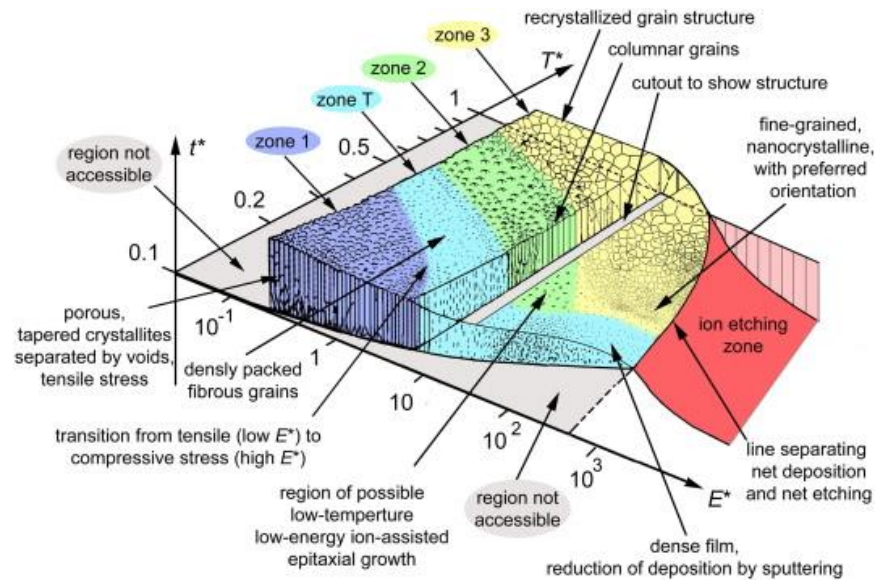


Figure 3-5 : Anders' modified structure zone diagram : The growth varies from a columnar microstructure (low E^* and T^*) to grain growth (high E^* and T^*). A region identified as *ion etching zone* is observed at high E^* . Image taken from [51].

The two main parameters of the Anders' SZD are E^* the normalized energy and T^* the generalized substrate temperature, describing, respectively, the kinetic energy of the bombarding particle and potential energy of the deposited particles. Depending on the region in the diagram, it is possible to observe that the normalized thickness t^* and the growth types are affected by E^* and T^* . At low energies, the growing film tends to be more porous and thicker, whereas at higher energies the resulting microstructure is denser and more crystalline. As functional coatings are strongly affected by their structural characteristics (porosity, stress, crystallinity, etc.), choosing the appropriate growth conditions is paramount. At high E^* , a zone labeled “ion etching zone” in Figure 3-5 can be seen, as growth is no longer observed resulting from the densification/etching of the underlying surface. This effect can also be useful in functional coatings fabrication when depositing a dense

film on top of a porous one, as surface densification can lower the roughness of a porous film allowing to deposit a subsequent film in more controlled conditions.

3.2.3 Bias-assisted plasma etching

An interesting feature regarding the SZD is the “ion etching zone”, which results from highly energetic ionic bombardment. In this regime, no growth is possible, and the film thickness will reduce overtime. While thickness reduction occurs, densification of the top part of the film is also observed. A study made in our group by Vernhes *et al.* prior to Anders’ model, showed the effect of plasma etching on roughness as shown in Figure 3-6 [52].

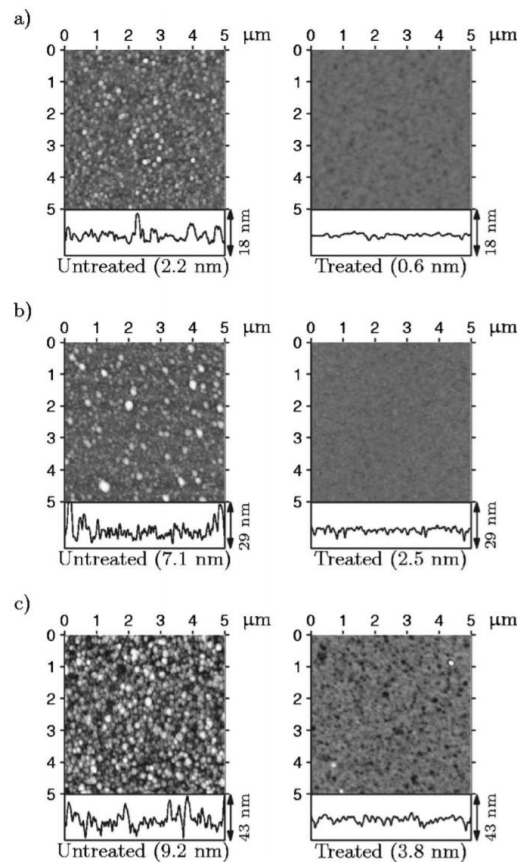


Figure 3-6 : AFM topography showing the effect of a 5 minute Ar plasma treatment at $V_B = -600$ V on the surface roughness of $\text{SiN}_x\text{:H}$ porous films: a) one layer, b) two-layer porous-dense stack and c) 13 layers porous-dense stack. Image taken from [52].

In the latter study it was observed that both surface densification and surface preferential sputtering were occurring at high bias. The result of these two phenomena was the confirmation of an overall

decrease of the surface roughness (see Figure 3-7). This work was inspired by the necessity to grow dense/porous multilayers with abrupt interfaces, and this ended up being important in the present thesis as well.

As similar approach was implemented in the present project to reduce the surface roughness of porous EC materials prior to the deposition of the top ITO electrode. This proved critical when depositing very thin ITO films as the sheet resistance was observed to significantly decrease following such a treatment. For high thicknesses (higher than the roughness), the effect of the subsequent layer has less impact on the film resistivity; however, for films having lower thicknesses, this method proved to help the integrity of the grown subsequent dense ITO layers.

3.3 Optical characterization

Significant part of this project was the characterization of the optical properties of the ASSD's materials, using spectroscopic ellipsometry and spectrophotometry. The objective of these measurements was mainly to obtain the refractive index (n) and extinction coefficient (k) of each material involved in the ASSD fabrication, and most importantly, of the EC materials in their various states of coloration. With the obtained dispersion curves, it is then possible to model and predict the optical response of the ASSD depending on the level of coloration. In this section, the characterization and the modeling techniques will be described.

3.3.1 Spectrophotometry

Spectrophotometry is a quantitative method to measure the intensity of light reflected off or transmitted through a sample. To measure both these properties at multiple wavelengths, two techniques are usually employed. In the first one, a monochromator is used to generate a monochromatic light beam and a photodetector measures the resulting intensity after interaction with the sample under study; the sample is thus scanned one wavelength at a time. In the second approach, a broadband light beam covering the desired spectrum is sent onto the sample and the transmitted or reflected beam is then sent onto a diffraction grating; the spatially separated light is then directed to a CCD detector where each pixel measures intensity at a specific wavelength. The first technique offers the advantage of a higher resolution (narrower spectral bandwidth) whereas the second technique provides much faster measurements. Note that both techniques require a

baseline prior to acquisition. Figure 3-8 shows a schematic representation of a monochromator-based spectrophotometer.

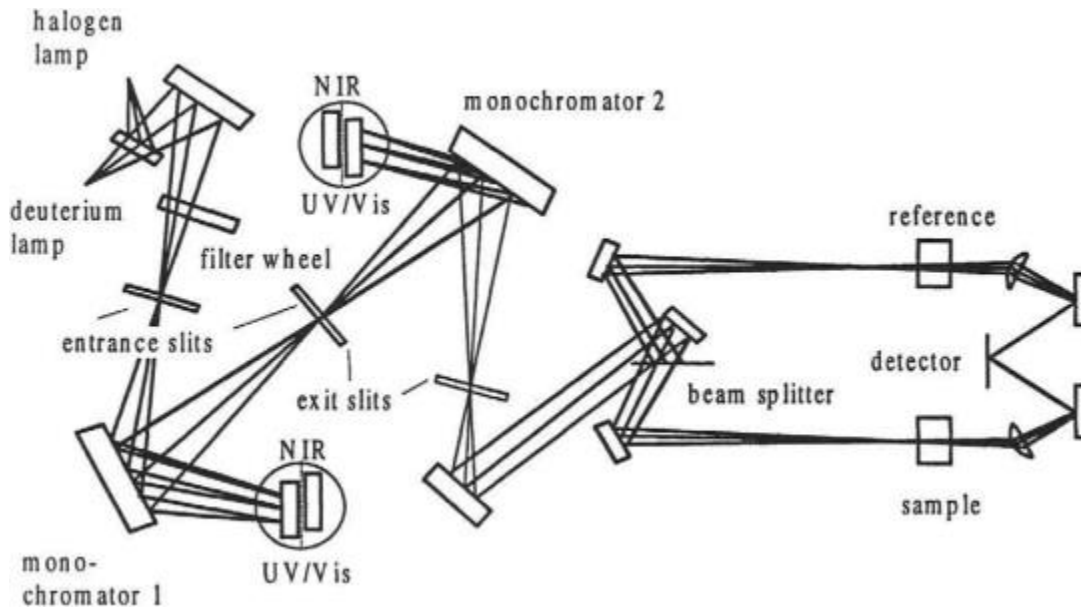


Figure 3-7 : Schematic of a Lambda 1050 spectrophotometer's functional parts. Image taken from [53].

The schematic of Figure 3-7 can be associated to the first measurement technique, *i.e.* with the use of monochromators. Because the source intensity fluctuates overtime, a baseline alone cannot provide accurate corrections to the measurements. In this case, a reference beam (not interacting with the sample) is used to compare the initial signal with the light coming out of the sample, compensating for these fluctuations.

Two spectrophotometers were used during the project, the first being the Lambda 1050 from PerkinElmer, which also possesses a liquid cell mount used to measure the transparency of liquid solutions. The second spectrophotometer was the Cary 7000 from Agilent Technologies, equipped with a universal measurement accessory (UMA) allowing one to characterize samples at multiple angles in both transmission and reflection up to 85° .

3.3.2 Spectroscopic ellipsometry

Spectroscopic ellipsometry is an essential characterization technique in the optical material field. The basic principles have been established by Paul Drude in 1945 [54], but the technique continues to be improved. As the measurement is sensitive to phase variations between an incident polarized-

known and a reflected beams on a surface, ellipsometry is not only sensitive to intensity changes (such as in spectrophotometry) but also to phase changes making it much more sensitive to minor surface modifications and very thin films. The principle of ellipsometry is to send light with a known polarization onto a surface and analyze the resulting change in polarization. Figure 3-8 shows the main components to perform such a measurement.

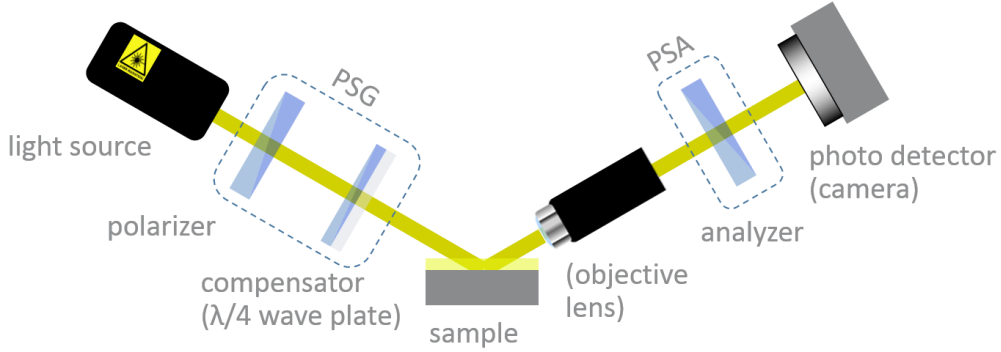


Figure 3-8 : Ellipsometer base components. Image taken from [55].

The light coming out of the source is unpolarized and can cover a broad spectral range for spectroscopic ellipsometry. The light beam first passes through the polarization state generator (PSG), where it is first polarized and then phased-delayed by a compensator. Thus, before reaching the sample at a predefined angle, the polarization state of the light beam is precisely known. After interacting with the surface in reflection in the present case, the phase and amplitude of both polarizations will vary. The resulting polarization is obtained by sending the light beam through the polarization state analyser (PSA) and onto a detector. The phase delay (Δ) and intensity ratio (Ψ) between the p -polarization (parallel to the plane of incidence) and s -polarization (perpendicular to the plane of incidence) are defined by the following equations:

$$\begin{aligned}\rho &= \frac{-r_p}{r_s} = \tan\Psi e^{i\Delta} \\ \tan\Psi &= \frac{R_p}{R_s} \\ \Delta &= \delta_p - \delta_s\end{aligned}\tag{3-1}$$

with ρ the complex reflectance ratio, Ψ the amplitude ratio of both polarizations, Δ their phase difference, R the reflectance and r the Fresnel reflection coefficient. As ellipsometry is based on a ratio, it does not require a baseline measurement, as in the case of spectrophotometry, bypassing the issues created by the source intensity fluctuations. From the ellipsometric data (Ψ and Δ), it is

then possible to obtain the optical properties of the analyzed sample through modeling (see 3.3.3 for more details) – ellipsometry is thus an indirect characterization method. The ellipsometer used during the project was a RC2-XI from J.A. Woollam Co., Inc. By combining measurements performed at multiple incidence angles with transmission/reflection spectra obtained on the UMA, reliable optical models were built.

3.3.2.1 Cyclic voltammetry *in situ* measurements

An advantage of optical measurements is that they are most of the time non-intrusive in physical experiments. As such, it is relatively easy to optically characterize surfaces *in operando* or *in situ* while fabricating or treating a sample. For EC materials, the dependency between optical and electrochemical properties is key to comprehending the coloration dynamics. The most popular approach is to measure the variation in transmission at a single wavelength (for example at 550 nm, the peak in the human eye's sensitivity), however when measuring a single wavelength, less information is obtained with regards to the coloration mechanisms. In this project, both multiwavelength transmission spectrophotometry and ellipsometry were used to characterize the electrochromic behavior of materials *in situ*. To perform cyclic voltammetry *in situ* measurements, we used a chemical cell attached to the RC2-XI, as shown in Figure 3-9.

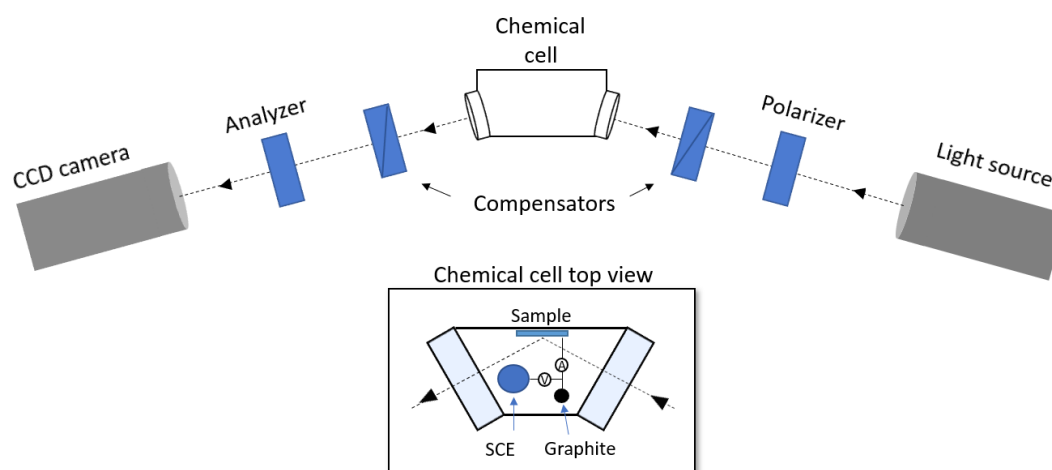


Figure 3-9 : Schematic of the chemical cell used for cyclic voltammetry measurements attached to a RC2-XI ellipsometer.

As this tool can be used to characterize EC materials dynamically (multiple measurements during a single cycle), limitations and disadvantages are also associated with, such absorption caused by

water, limiting the spectral range and limitation to single angle measurements (unlike conventional measurements where multiple angles are used). More details will be given in Chapter 4, where *in situ* vs. *ex situ* techniques are compared.

3.3.3 Modeling

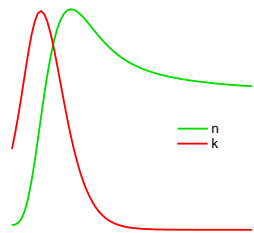
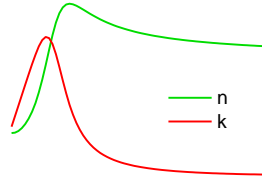
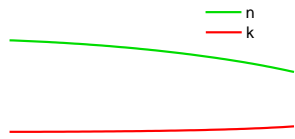
The complex refractive index, $N = n - ik$, where n is the refractive index and k the extinction coefficient, is an intrinsic and critical parameter when it comes to optical filters. Indeed, where the optical response may vary depending on the thickness, inhomogeneity and other physical aspects, the refractive index will remain invariant if the material keeps its structural and compositional integrity. This is important when trying to predict the optical response of an optical system.

When characterizing a material by spectroscopic ellipsometry, the first step is to establish an optical model which will allow for the generation of the appropriate dispersion curves for n and k . By fitting the model to the experimental data, one obtains the desired optical properties. Using the matrix method described further below one can then model the theoretical response in reflection and transmission of the characterized material.

3.3.3.1 Obtaining the dispersion curves

Modeling the ellipsometry/spectrophotometry data can be tricky, as multiple physical phenomena can be at play (bandgap, absorption bands, free-electron contributions, etc.). Thus, to accurately model optical data requires skill and practice. The best mathematical tool available for representing the optical response of materials are oscillators, which are essentially mathematical functions derived from physical models describing light-matter interactions, e.g.: the electrons in a material. Table 3-4 shows various oscillators implemented during the analysis of the multiple materials required in this project. Aside from the optical properties, other useful information can be obtained from the models, such as the layer thickness, the surface roughness, the presence of inhomogeneity vs. growth, thickness non-uniformity, and much more.

Table 3-4 : Optical oscillators used to obtain the optical properties of materials.

Oscillator	Parameters	Form vs. wavelength (300-1000 nm)	Utility
Gaussian	Amplitude, width, energy.		Allows fitting of absorption bands.
Tauc-Lorentz	Amplitude, broadness, energy, band gap energy.		Asymmetrical oscillator that mimics the band gap behavior of materials.
Drude	Resistivity and scattering time.		Model the dispersive behavior of metals due to the presence of free electrons.

The analysis of a single material can require the use of multiple oscillators to accurately fit the data. For example, in the case of ITO, a Tauc-Lorentz oscillator is used to model the band gap of the material and a Drude oscillator to model the free electrons responsible for its conductive properties. A gradient (variation vs. thickness) in the resistivity of the Drude model is also often added to improve the match between the experimental and modeled data (better fit). In another example, to accurately model colored WO_3 , a gaussian oscillator must be added to the bleached state model to represent the W^{5+} - W^{6+} transitions.

3.3.3.2 Dispersion curves, Fresnel coefficients and the matrix approach

Having obtained the dispersion curves of the characterized materials, it is possible to calculate the Fresnel coefficients (R and T and A from $A = 1 - R - T$) of a single interface. When considering

optical filters which consist in a series of layers of different materials and with specific thicknesses one must also consider the phase of the multiple light beams being reflected/transmitted at the various interfaces. Indeed, it is the interaction of these multiple beams which is at the basis of thin film interference. For a system of j layers, with each layer having a given refractive index N_j and thickness d_j , the following approach allows for the calculation of the transmission and reflection using a matrix formulation:

$$M_k = \begin{bmatrix} \cos \varphi_k & \frac{i}{N_k} \sin \varphi_k \\ iN_k \sin \varphi_k & \cos \varphi_k \end{bmatrix}$$

With M_j the characteristic matrix of layer j and φ_j the phase shift at normal incidence given by:

$$\varphi_k = \frac{2\pi}{\lambda} N_k d_k$$

To obtain the response of a multilayer stack, one simply needs to multiply the matrices of each individual layer:

$$M = \begin{bmatrix} m_{11} & m_{12} \\ m_{21} & m_{22} \end{bmatrix} = \prod_{j=q}^1 M_k$$

Where q is the total number of layers. Finally, the reflection and transmission can be obtained from the final M transfer matrix by using the following equations:

$$\begin{aligned} r &= \frac{m_{11} - N_s m_{22} + N_s m_{12} - m_{21}}{m_{11} + N_s m_{22} + N_s m_{12} + m_{21}} \\ t &= \frac{2}{m_{11} + N_s m_{22} + N_s m_{12} + m_{21}} \\ R &= |r|^2 \\ T &= \text{Re}(N_s) |t|^2 \\ A &= 1 - R - T \end{aligned}$$

With N_s the refractive index of the substrate. References [56, 57] describe this approach in more detail. These same equations are at the basis of most optical filter design software such as *OpenFilters* [50], a homemade open-source software developed at the FCSEL by S. Larouche. Such modeling is at the basis of optical filters design. It allows the thickness optimization of each material comprising a filter, creating optical patterns observed in antireflective filters, bandpass filters and more.

3.4 Electrochemistry

Electrochemistry is a science that studies the relationship between electrical and chemical changes. More precisely, when an electrical potential is applied at the extremities of a medium and an electric field is formed, electrochemical measurements will quantify the chemical change induced by the field. Following the Nernst equation (variation of an ion concentration being proportional to an equilibrium potential), the chemical nature of a medium varies depending on a certain potential applied on its ionized species. When this potential varies, the concentration of ions is therefore affected. A common technique called cyclic voltammetry (CV) based on this phenomenon characterizes the chemical changes upon a variable applied potential with a defined scan speed. Such electrochemical measurements are key in ECs; in combination with optical characterizations, determination of the coloration efficiency is then possible.

3.4.1 Cyclic voltammetry



For the specific case of EC materials, the most common electrochemical CV procedure is based on applying a voltage between two electrodes on a Electrode | Ion reservoir | EC film | Electrode system. While linearly varying the potential between a positive and negative value at a specific scan rate, ions and electrons are intercalated and de-intercalated in the material under study, and this charge displacement generates an electrical current which can be measured. When combining cyclic voltammetry with *in situ* optical measurements, it is possible to accurately quantify the coloration and bleaching performance of an EC material.

For NiO and WO₃ characterization, we used a chemical cell equipped with two transparent windows to spectrally characterize the optical behavior of the films in transmission. A saturated calomel electrode (SCE) was used as the **reference electrode** (RE), a graphite rod as the **counter electrode** (CE), and the sample itself as the **working electrode** (WE). A PGSTAT204 potentiostat from Metrohm applied a voltage between the counter and working electrodes and the resulting current between the working and counter electrode measured. The following procedure was applied in order to perform a cyclic voltammetry measurement. First, the chosen electrolyte was inserted into the cell and the CE and RE installed. After, a baseline was taken in the case of spectrophotometry measurements. The sample (WE) was then installed and the optical acquisition started. Before starting the CV sequence, a fixed potential was applied (positive for WO₃, negative

for NiO) for 60 s to allow the film to be fully bleached prior to the first cycle. Finally, the cycling sequence was started, at a specific scan rate in a given voltage range and for a predefined number of cycles. Table 3-4 below specifies the detailed parameters used in CV sequences for both studied EC materials.

As observed in the CV measurement sequence, the full electrochromic characterization requires the simultaneous execution of the said sequence in combination with the *in situ* transmission measurement; a correct synchronization of both these obtained data sets is critical when interpreting the measurements. In this work, the synchronization was accomplished by matching the start of the optical variation with the start of the electrochemical sequence, as transmission measurements are acquired earlier for calibration.

Table 3-5 : Parameters used for cyclic voltammetry procedures on NiO and WO₃ films.

		NiO	WO ₃
Electrolyte	Chemical formula	KOH / LiClO ₄ -PC	H ₂ SO ₄ / LiClO ₄ -PC
	Concentration	1 mol/L / 1 mol/L	0.1 mol/l / 1 mol/L
Voltage	Range	-0.6 – 0.7 V	-0.6 – 1.0 V
	Scan rate	25 mV/s	10 mV/s
Characteristic shape			

Through careful analysis of CV measurements, it is possible to observe several dynamics, such as charge trapping, phase changes, film degradation, inserted and extraction charge ratios, the diffusion coefficient of ions, intercalation ratio and coloration efficiency (when coupled with *in situ* transmission measurements [24]).

3.4.2 *In situ* spectroscopic transmission

During the CV tests, the best suited characterization procedure to quantify the coloration is to measure the transmission variation overtime, the coloration efficiency being one of the most important metrics of EC materials. A USB2000 spectrophotometer in combination with a deuterium and tungsten halogen DH2000 lamp sources were used to measure the transmission in the 300 nm to 800 nm range.

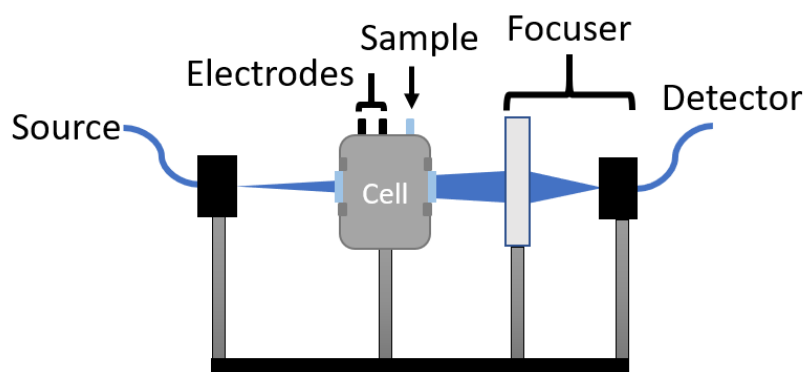


Figure 3-10: Optical setup schematic for *in situ* spectroscopic transmission measurement during cyclic voltammetry procedures.

The setup from Figure 3-10 is composed of a source and a detector that are used to send and collect the light which passes through the sample under study. As the divergence of the beam was low, no collimator was required to limit the spot size on the sample. However, to maximize the signal, a focuser was implemented to converge the beam onto the detector. The acquisition rate and number of scans to average were set to maximize the signal at a 1 spectrum/second. A baseline was performed by blocking the beam to acquire the background signal followed by 100% reference spectrum. The data saving option was then activated when the CV experiment was ready to start.

With the data acquired from these measurements, it is possible to quantify the coloration efficiency (η), determine the coloration speed as well as serve during the optical modeling phase to increase accuracy.

3.5 Microstructural characterization

Several characterization techniques were used during the project to obtain further information on the composition, surface morphology and crystallinity of the samples. The basic principles of these techniques are described in this section.

3.5.1 Scanning electron microscopy

As the observable physical phenomena of interest in this project are in the range of the nanometer to micrometer scale, a choice between two imaging systems was available: atomic force microscopy (AFM) or scanning electron microscopy (SEM). At the beginning of the project, AFM was considered to characterize the surface of the NiO films, but a fast degradation of the scanning probe tip falsified the resulting topographic measurements. Therefore, SEM was used for the remainder of the project.

The principle of topography SEM measurements is to analyse the secondary electrons coming from the surface of the sample created by the exposure of the surface to an electron beam. By methodically establishing a raster with a beam, a mapping of the electronic signal intensity results in an image that contains topographic information.

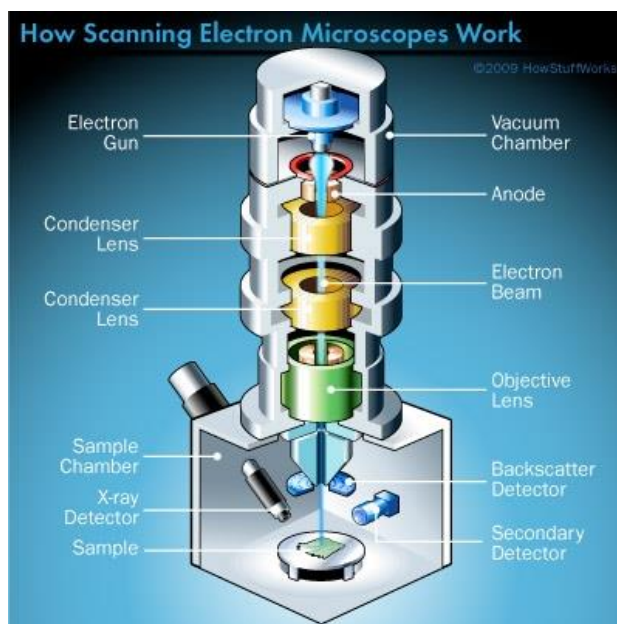


Figure 3-11 : Schematic of a typical scanning electron microscope. Image taken from [58].

For the project, topographic measurements of cross sections and surfaces were performed using the JSM-7600F SEM from Jeol. Images with magnifications varying between 10 nm and 100 microns (magnification of 10X to 100 000X) were obtained using the secondary detector.

3.5.2 X-ray diffraction

X-ray diffraction (XRD) is a method that allows the determination of the structure of a crystal. As many deposited thin films are polycrystalline (see Figure 3-5), XRD can be used to study the effect of many factors on a known structure, such as stress, annealing, chemical treatments and others. The process is based on Bragg's principle, in which a beam is diffracted at a specific angle (θ), depending on the wavelength (λ) and the distance between the crystallographic planes parallel to the surface. Bragg's law describes the principle of diffraction with the said parameters as follows:

$$2d \sin \theta = n\lambda \quad 3-2$$

The known parameters being θ and λ , the unknown and of interest variable being d . The interplanar distances in a crystal are in the Å range (10^{-10} m), and so must be the wavelength of the radiation to observe diffraction. As a spectrum (multiple λ) in this region is hard to obtain practically (a synchrotron would be needed), the technique is typically restricted to the use of a monochromatic source. The λ variable from Bragg's law being fixed, the solution to observe diffraction at specific interplanar distances is to scan the surface angularly (θ). Using the Bruker D8 XRD system, it is possible to establish a diffractogram of the characteristic peaks of a crystal depending on the incidence angle. More precisely, while angularly scanning a sample with an X-ray beam, characteristic diffraction peaks will appear when the angle will correspond to $\arcsin(n\lambda/2d)$. Two sample-beam configurations were used during the project, the first being θ - 2θ . This technique relies on scanning the surface with the source and detector keeping a θ - 2θ dependency, limiting the observed diffracting planes to the ones which are parallel to the surface. The second technique used is the grazing incidence XRD (GIXRD) and relies on a fixed source positioned at a low angle (about 1°) and scanning a full angle range with the detector. With this technique, all planes which are not parallel to the surface can be observed, which can be helpful for structures exhibiting low crystallinity.

3.5.3 Ion beam analysis

In 1911, Rutherford demonstrated that atoms are composed of a positively charge dense nucleus, obsoleting Thompson's plump pudding model. The experiment relied on the detection of scattered ions when alpha particles interacted with a solid object, a gold foil in this case. With Thompson's theory, the positively charged incident particle would simply pass through the atom, however, observing a backscattering effect proved the existence of protons inside atoms. The interest of this experiment nowadays is the quantification of the energy lost by the backscattered ions to the nuclei of the material's atoms' during the elastic collision. The technique used to measure the composition of a material based on this experiment is called Rutherford backscattered spectrometry (RBS). The basis of RBS is to expose a sample to a beam of high energy ions (He^{2+} or alpha particles) and detect their energy when they are backscattered. In the elastic regime, the momentum transfer between the beam's ions and the atoms of the studied surface is proportional to the atoms' mass, therefore so is the remaining energy of the backscatter ions. By measuring the number and energy of the backscattered ions, it is possible to establish the composition and area density of a material.

One limitation of RBS occurs when studying materials composed of light atoms such as hydrogen. When the mass of the ion is close to the interacting atom's, the elastic collision will eject the atom from the surface instead of backscattering the charged particle. A technique known as elastic recoil detection (ERD) allows the classification of the ejected atoms. Equipped with a mass spectrometer, an ERD system can determine the atoms composing the studied structure by analyzing the ejected species. As the technique does not rely on backscattering light ions, heavier elements can be used in the beam to increase the degree of ionisation, increasing the beam's energy (applied voltage times degree of ionisation) and therefore the ejection efficiency. Also, by knowing the energy of the incident ions, timing the flight duration between the ejection and the detection of the atom can establish the depth profile of the structure with the identified atoms composing it.

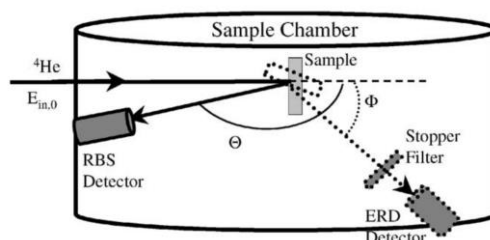


Figure 3-12 : Schematic of an RBS/ERD measurement set-up. Image taken from [59].

From Figure 3-12, the basic principle of an RBS/ERD system is detailed, where depending on the position of the sample, backscattered ions or ejected atoms can be measured. However, in the facilities available, the two experiments were conducted in different ion beam lines. The system used for the RBS measurements is a 1.7 MeV Tandetron accelerator, with a 2 MeV He^{2+} beam. The ERD measurements were made in a Tandem accelerator using particles with energies of up to 48 MeV, equipped with a 7.5 μm mylar foil to filter out any scattered ions from heavier elements than hydrogen. To extract the atomic density and composition from the ion beam measurements, the software Simnra 7.0 was used to simulate the spectra and correlate them to a specific material composition.

CHAPTER 4 *IN SITU* SPECTROSCOPIC STUDY OF ELECTROCHROMIC NICKEL OXIDE FILMS

4.1 Foreword

The study of nickel oxide films was a major part of the project, motivated by the objective 2 criteria. The coloration of the material having a direct impact on its refractive index, rigorous characterization of the optical properties was needed in order to allow for the modeling of full ASSD stacks. First, the methodology used to fabricate and characterize the samples is described. Following are the measurements of the films' optical properties during coloration. The measured properties (R , T , A , Ψ , Δ) were used to create optical models from which the dispersion curves could then be established dynamically, meaning that the models are time-, and thus, charge-dependent. Following the optical characterization, the electrochemical properties are discussed, establishing a correlation between the observed optical behavior and phase evolution (ageing). Finally, additional physical characteristics are presented to determine the structure and stoichiometry of the films, along with their intercalation level.

4.2 Methodology

The fabrication of NiOOH films followed the previous work by Niklasson *et al.* [20] and by Kitao *et al.* [27], in which a plasma composition of 40% hydrogen, 2-6% oxygen in a complementary argon environment was used. With the objective of maximizing the coloration efficiency (η), a study of the effect of the deposition pressure and oxygen composition was first performed. To do so, a series of samples were fabricated by magnetron sputtering onto glass substrates coated with ITO (18 nm). The target used during the sputtering process was composed of 93% Ni and 7% Va. The thickness target was fixed between 150 nm and 200 nm with a preestablished deposition rate of $\sim 4 \text{ \AA/s}$. To set the optimal pressure and oxygen composition, the chosen strategy was to first establish the pressure giving the highest η between 5, 10, 15, 20 and 25 mTorr with 12% oxygen (arbitrary value), and secondly, having chosen the pressure, repeat a new deposition sequence to obtain the ideal oxygen composition between 5%, 10%, 15% and 20% giving the highest η . The

power density was established to maximize the power. The parameters yielding the highest η are listed in Table 4-1.

Table 4-1 : Deposition conditions of the nickel hydroxide films with maximized coloration efficiency deposited in the MAG-4 system.

Gas proportion (%)			Power density (W/cm ²)	Deposition pressure (mTorr)
H ₂	O ₂	Ar		
35	5	60	7.4	15

With the optimal deposition parameters established in Table 4-1, a series of identical NiO films were deposited for further optical analysis during electrochemical cycling.

The CV process applied to the NiO samples was a sequence of 30 cycles of voltage sweeps between -0.6 V and 0.7 V at a scan rate of 10 mV/s in a 1 M KOH solution. The sequence was performed both in two different electrochemical cells, one for the *in situ* transmission measurements and the other for the *in situ* ellipsometric characterization. Two methods were also adopted to gain the optical properties through coloration: *in situ* measurements were used to gain the dynamic optical properties, *ex situ* measurements for the accurate modeling of the bleached and colored states of the film. Depending on the desired state, the cycles were followed by the application of a fixed potential of either -0.6 V for bleached films or 0.7 V for colored films for 1 minute. The samples were then rinsed with DI water and dried with a nitrogen flow before characterization within 1 minute to limit charge leakage.

4.3 Optical properties

The strategy used to characterize the dynamic optical properties of nickel oxide is based on a two-step sequence. First, after being cycled in the CV process for 30 cycles mentioned in the previous section, they were characterized *ex situ* (meaning after the experiment) with the spectrophotometer and ellipsometer to establish a liable model in both bleached and colored states. Second, with samples of the same fabrication process from the ones studied *ex situ*, optical characterization (spectrophotometric and ellipsometric) was performed *in situ* (meaning during the experiment) in order to analyse dynamically the optical properties depending on the coloration level.

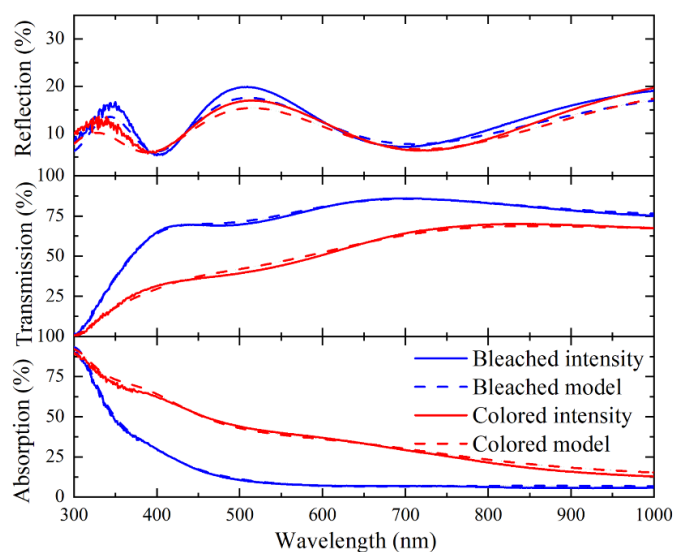


Figure 4-1 : Spectrophotometric measurements of the NiOOH films in their colored and bleached states after the 30th cycle.

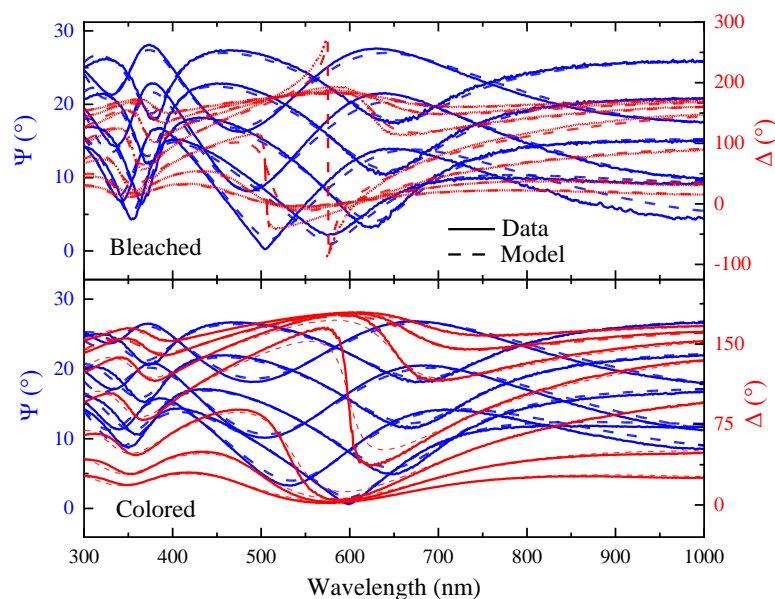


Figure 4-2 : Ellipsometric measurements of the NiOOH films in colored and bleached states obtained between 45° and 70° for every 5° after the 30st cycle.

Figure 4-1 shows the reflection, transmission and absorption spectra of the bleached and colored films. One can observe a clear increase in the absorption when the material is colored and a corresponding drop in transmission. However, the reflection decreases by only 1.5% at 550 nm.

This effect is mainly due to the coloration mechanism of NiOOH, which relies on a bandgap displacement in the visible spectrum creating an absorption band upon deintercalation; the latter having little impact on the reflection spectrum. Figure 4-2, shows the corresponding ellipsometric data; as the reflection does not change significantly in intensity, changes in Ψ are correspondingly limited whereas changes in Δ are, nevertheless, more important.

From the *ex situ* spectral measurements, an accurate optical model was established in order to obtain the dispersion curves, as it is based on ellipsometry data measured at multiple incidence angles combined with reflection and transmission spectrophotometric data, not to mention that all the data was acquired using longer acquisition times for higher precision .

The experimental step that followed was to measure the optical properties with the *in situ* ellipsometry and transmission spectrophotometry techniques to model the time dependant refractive index and extinction coefficient.

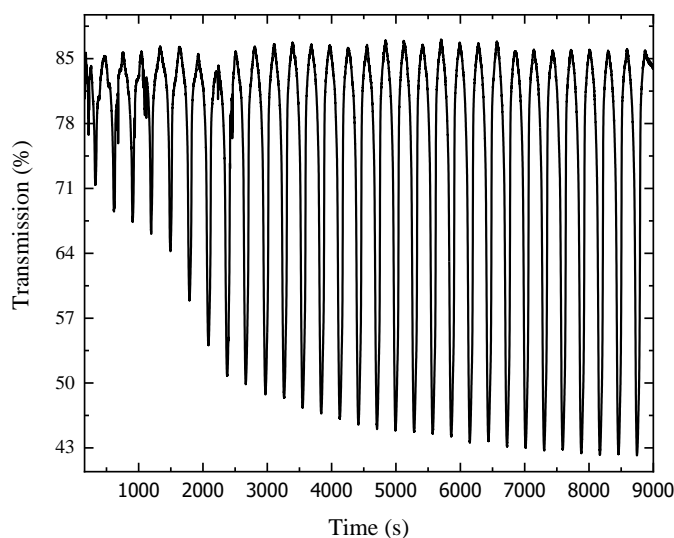


Figure 4-3 : *In situ* transmission variation at 550 nm showing the evolution of the bleached and colored states over 30 cycles.

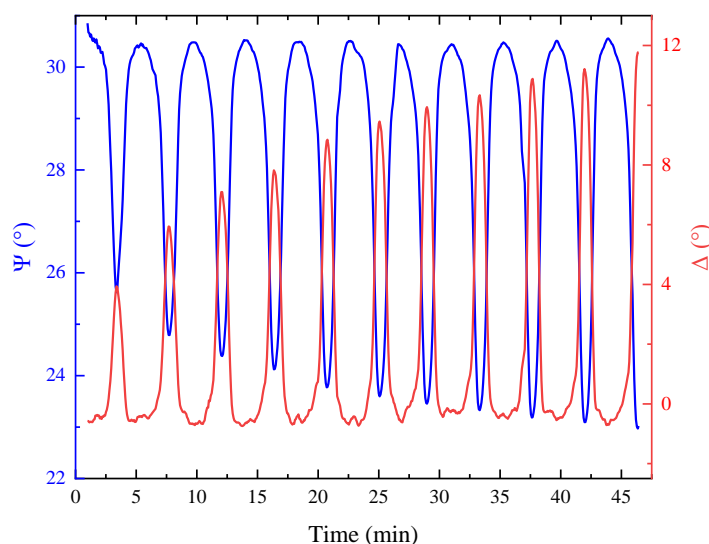


Figure 4-4 : *In situ* ellipsometric measurements at 550 nm showing the Ψ and Δ variation during coloration and over the 10 first cycles at an angle of 70° .

The optical activation of the NiOOH film, as seen in Figure 4-3, suggests an absorption increase from $\sim 10\%$ to 40% during cycling (assuming a limited change in the reflection as demonstrated in Fig. 4-1). One can also observe a limited change in the bleached state transmission indicating that while the film is increasing its EC activity it is otherwise stable. This activation is also observed in the ellipsometric data which shows an increasing variation in Ψ and Δ (see Figure 4-4). While the optical *ex situ* measurements showed minor changes in reflection following coloration, the *in situ* transmission measurements show an “activation” period which directly impacts the optical behaviour. This activation period can be attributed to the formation of NiOOH clusters and to *ageing*, a phase transformation observed when water is removed from interplanar spaces as discussed in section 2.2.2.

The oscillators were adjusted to the optical measurements in order to model the dispersion curves using the following methodology. With the *ex situ* spectroscopic and ellipsometric measurements, a Tauc-Lorentz oscillator was used to fit the experimental data in the bleached ($\text{Ni}(\text{OH})_2$) and colored (NiOOH) states. These models, deemed rigorous due to multiple *ex situ* measurements made on the samples, were implemented in a Bruggeman effective medium approximation (EMA) model to fit the dynamic measurements of the *in situ* method. This approximation supposes a host

material of $\text{Ni}(\text{OH})_2$ with spherical inclusions of NiOOH , corresponding to deintercalated crystallites, whose concentration varies depending on the coloration state. This approach was also judged to be more reliable as it limited the total number of fitting parameters (thickness, concentration of NiOOH and surface roughness). Indeed, adding the Tauc-Lorentz parameters to the fitting process most often resulted in optical properties which were diverging from the expected values in the Tauc-Lorentz parameter's values (bandgap of 0 eV for example). Also, the mean square error (MSE) increased from 30 to 45 when coloring, reducing the model reliability.

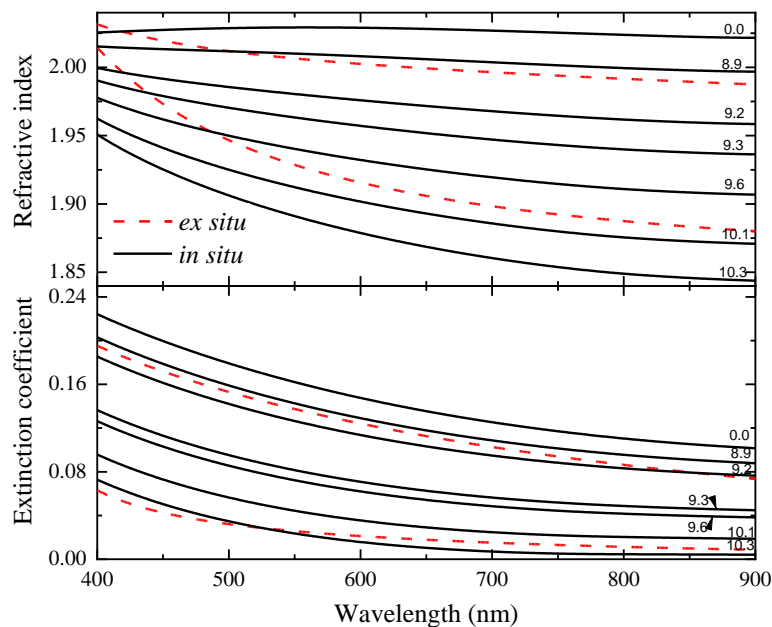


Figure 4-5 : Charge-dependent dispersion curves of NiOOH displaying the transition from bleached to colored states during the 10th cycle.

Figure 4-5 shows the variation in optical properties when charges are extracted during the 10th cycle. As expected, the material displays dielectric-like optical properties with a refractive index of 1.88 and a low extinction coefficient of 0.04 at 550 nm in the bleached state, compared to the semi-conductor-like properties with a refractive index of 2.05 and higher extinction coefficient of 0.16 at 550 nm in the colored state. The variation in k explains the absorption observations in the spectrophotometric measurements, while the variation in n suggests that this would lead to changes in the optical thickness and thus changes in the interference properties of an optical filter.

When comparing the *ex situ* and *in situ* results, a mismatch between the refractive indices below 500 nm is observed, as the dispersion curves are quite sensitive to the change in bandgap during modeling. Also, in both intercalated and non-intercalated states, the *ex situ* n and k do not perfectly coincide but are nevertheless quite close. In the case of the bleached state, some difference is expected as the *ex situ* sample was shown to lose charge as a function of time; as a result, one would expect a higher absorption in the case of the *ex situ* bleached sample; this is indeed the case especially when looking at the refractive index. Another possible explanation for the observed differences is that the material's optical behavior can change when going from an aqueous solution to a dry environment.

An interesting feature of *in situ* measurements is the limitation of the spectral range due to liquid absorption. While *ex situ* spectra can be measured up to 2.5 microns, NIR light gets absorbed in the solution when attempted *in situ*.

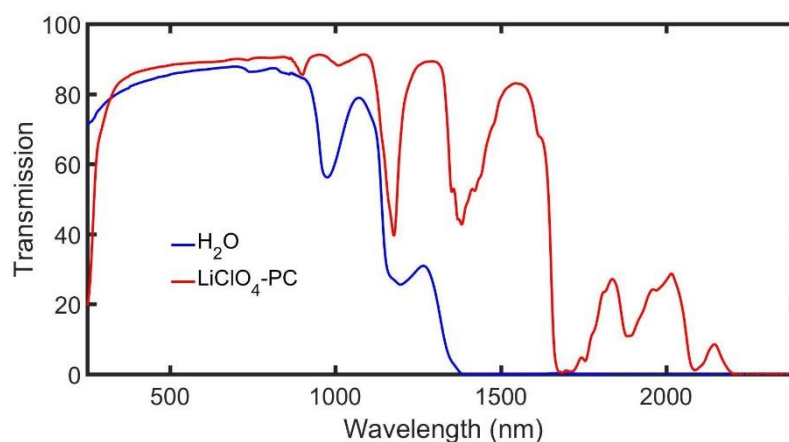


Figure 4-6 : Transmission spectra of water and lithium perchlorate from 300 to 2500 nm showing the absorption bands.

Light absorption in liquids can be problematic when studying the NIR spectrum, an important part of the solar spectrum. However, as presented in Figure 4-6, the visible part is less affected. The luminous transmittance which is shown is not 100%, but this effect is mainly due to reflection on the windows of the cell used for the measurements (3% at each interface).

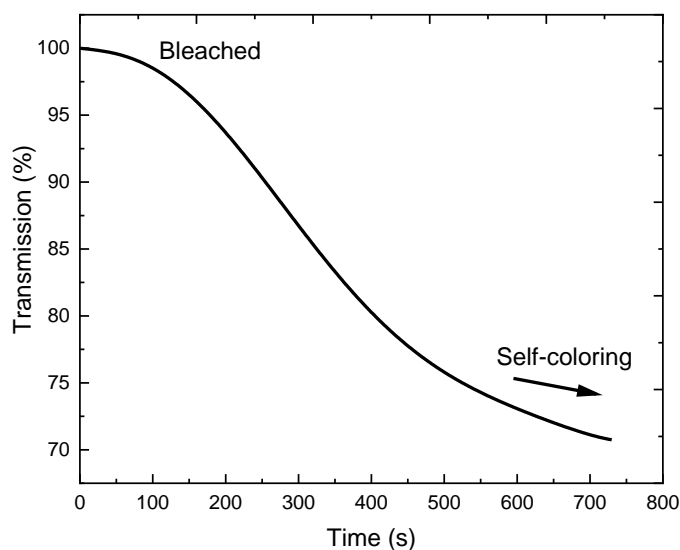


Figure 4-7: Self-coloration effect observed in the transmission variation at 550 nm of a NiOOH film after charge insertion and removal from the electrochemical cell.

To characterize the optical variation of NiOOH between a “wet” and “dry” environment, the *in situ* transmission optical system was used to measure a sample that was cycled and immediately remounted on the emptied cell. Figure 4-7 displays the corresponding relative transmission evolution as a function of time, showing a self-coloring behavior that is most probably due to water or charge desorption. This result confirms that *ex situ* measurements do not show the full amplitude of the optical properties due to desorption effects.

4.4 Electrochemical properties

To further understand the evolution of NiOOH upon cycling in KOH, an analysis of the obtained cyclic voltammograms during cycling was performed to help support the previous observations. In addition, in order to correlate the electrochemical and optical results, it was important to correctly synchronise both datasets. By quantifying the optical variation through charge insertion/extraction, the EC performances of the studied NiOOH films were established.

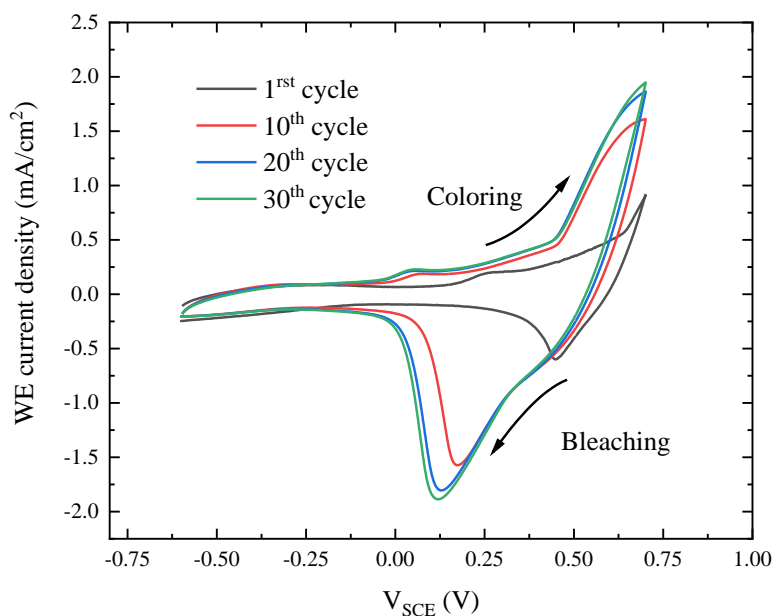


Figure 4-8 : Voltammograms of the cycled NiOOH film showing an increase in charge transfer as well as a cathodic peak displacement over time.

The charge calculation is obtained by integrating the area of a voltammogram (converting the voltage axis to time using the applied scan rate and integrating the current over time) for both the charge insertion regime (when the current is negative) and the charge extraction regime (when the current is positive). An increasing voltammogram surface, as can be observed when going from the first to the tenth cycle (see Figure 4-8), indicates that more charges are involved in the electrochemical process. This increase of charge is due to ageing, as described in section 2.2.3, which corresponds to the phase pathway from α -NiOOH \leftrightarrow γ -Ni(OH)₂ to β -NiOOH \leftrightarrow β -Ni(OH)₂ that is caused by H₂O absorption. When water is inserted into the material, an “unzipping” effect of the interplanar spaces allows charges to reach more intercalation sites [30]. This effect is also observed on the cathodic peak position, which varies from 0.45 V to 0.12 V, positions corresponding to α -NiOOH and β -NiOOH respectively [15].

Table 4-2 : Optical and electrochemical results characterizing the EC performance of the NiOOH film through cycling.

	1 st cycle	5 th cycle	10 th cycle	30 th cycle
Inserted charge density (mC/cm²)	5.4	5.7	10.6	12.6
Extracted charge density (mC/cm²)	4.5	5.9	10.4	12.6
Extraction ratio (%)	83	103	103	100
ΔT_{550nm} (%)	14.5	22.4	38.1	44.5
η (cm²C⁻¹)	34.3	52.2	54.6	57.3
Cathodic peak position (V)	0.45	0.38	0.17	0.12

From Table 4-2, it is possible to observe an increase in the optical and electrochemical properties throughout cycling. At first, little optical variation is observed, along with the amount of charges involved. The resulting coloration efficiency is however increasing, as the logarithm of the optical variation is higher than the charge insertion variation throughout cycling. This increase, following the characteristic cathodic peak position variation associated with ageing, suggest that the $\alpha \leftrightarrow \gamma$ pathway is less EC than the $\beta \leftrightarrow \beta$ pathway. The resulting η is comparable to what is published in the literature, *i.e.* between 30 and 100 cm²C⁻¹, a value that is affected by the deposition and cyclic voltammetry conditions.

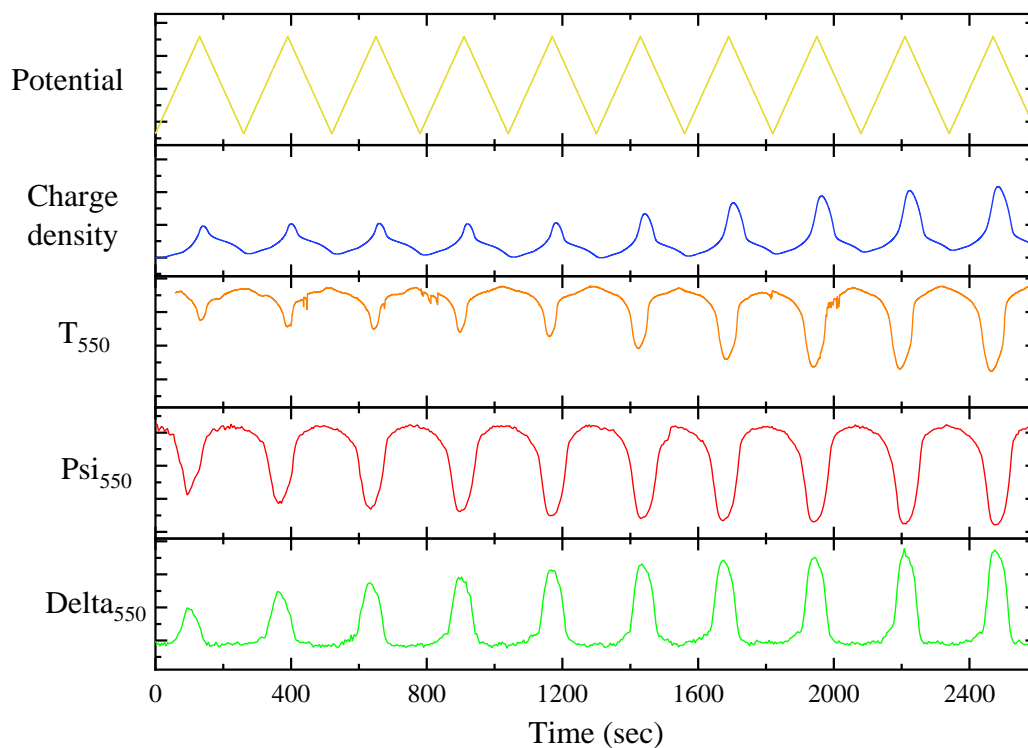


Figure 4-9: Electrochemical and optical properties as a function of time of cycled NiOOH films aligned vertically showing the data synchronisation.

The increase of the optical properties overtime follows the increase of the charge density inserted into the film, as seen in Figure 4-9. This effect tends to increase rapidly after the first few cycles of the process, reaching a steady state after approximately 10 cycles. From this point on, the material begins to be saturated in water, stabilizing the electrochemical properties.

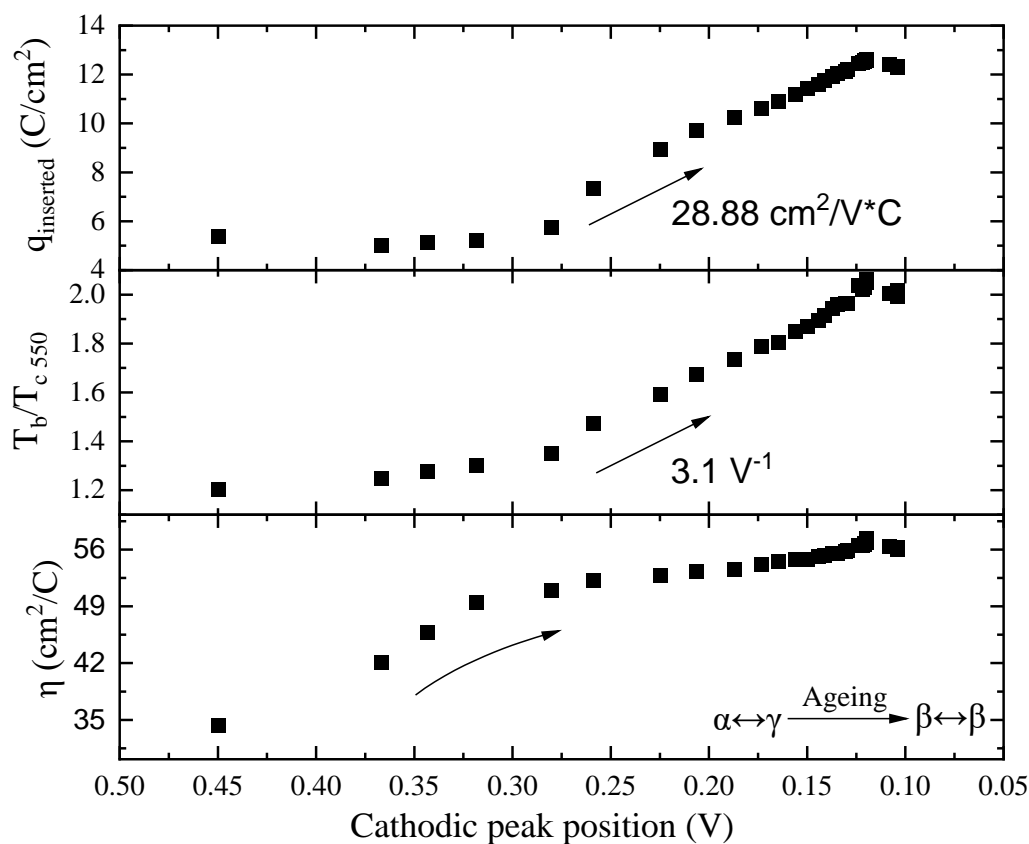


Figure 4-10: Variation of the EC properties depending on the cathodic peak position. The top curve shows the inserted charge, middle curve the ratio between the bleached and colored transmission and the bottom curve the coloration efficiency.

In Granqvist's reference handbook on EC materials [15], it is established that during activation of nickel hydroxide, the cathodic peak position shifts towards lower voltages upon cycling, a shift corresponding to the $\alpha \leftrightarrow \beta$ pathway (ageing – see Section 2.2.2). From the previous cyclic voltammetry results, it was also demonstrated that η increases with ageing. The source of this increase is shown in Figure 4-10, where the transmission variation and inserted charge density are both shown to vary linearly with the cathodic peak position. The transmission variation's slope being higher than the charge variation's, the resulting η increases. Using the ratio between the logarithm of T_b/T_c and the inserted charge q to get η , a plateau is observed after a few cycles even though T_b/T_c is still increasing. This behavior suggests that the EC performance stabilizes after 4-5 cycles, where the following cycles display an increase of transmission at the expense of a proportional increase of inserted charge density.

When correlating the dispersion curves of the material with the state of intercalation during a single cycle (as presented in Figure 4-5), a hysteresis behavior can be observed, suggesting a delay between the optical response and the intercalation level (see Figure 4-10).

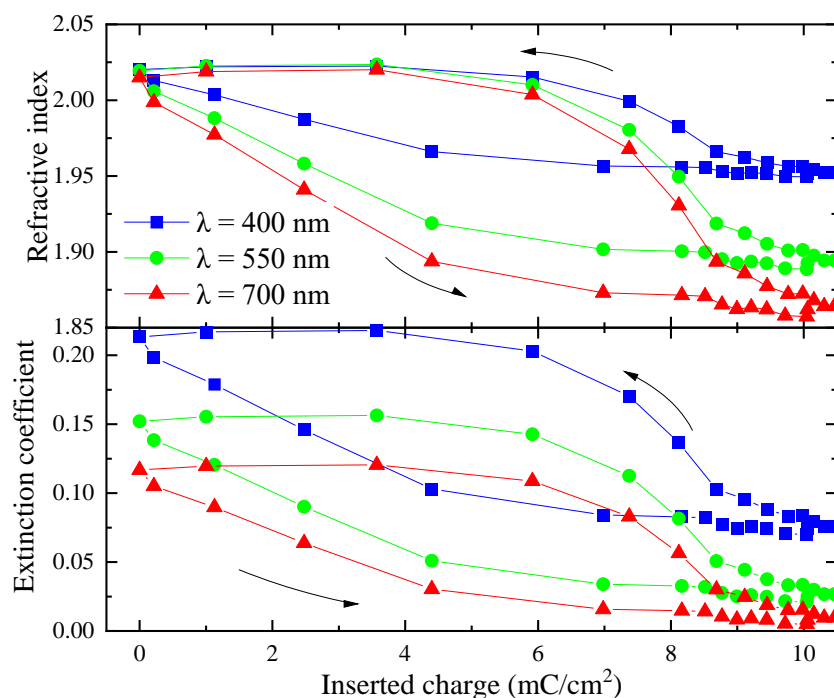


Figure 4-11: Refractive index (top) and extinction coefficient (bottom) variation as a function of inserted charge for the 10th cycle shown at specific wavelengths.

When looking at the dispersion behavior of NiOOH during the transition from a bleached state to a colored state and back to the bleached state, an asymmetrical coloration can be observed. At the beginning of the cycle (bottom right of Figure 4-11), no charge is removed until a sufficiently high potential is reached, suggesting a certain inertia of the carriers at lower voltages. Once coloration occurs, a saturation of both the refractive index and extinction coefficient is observed (top left). At the coloration maximum when all charges have been removed (0 mC/cm²), a minimal dispersion behavior is observed in the visible spectrum for the refractive index as all values converge towards 2.03 (as also observed in Figure 4-5). Once charges are reinserted and the potential switches, decoloration is observed, and the optical properties return to their original bleached state values.

Charge intercalation is also known to create a “swelling” effect in the film, as the structure expands when ions are inserted. With the use of the developed optical models, it is also possible to obtain

the thickness and surface roughness evolution of the films as a function of cycling. Whereas the roughness stays stable at approximately 40 nm, the thickness, on the other hand, is shown to vary during a single cycle and from cycle to another cycle as well (see Figure 4-12).

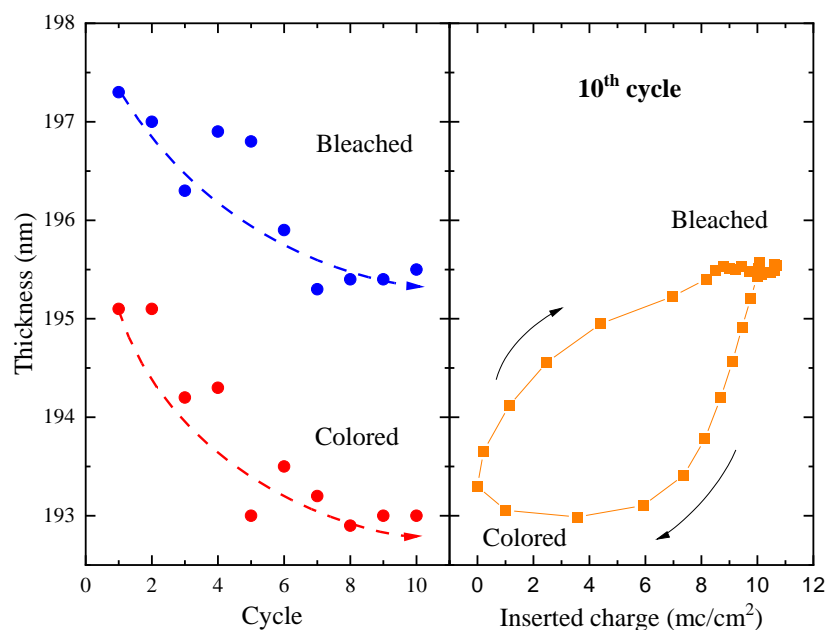


Figure 4-12: Thickness evolution during multiple cycles at the most colored and bleached states (left) and dynamic evolution of the thickness during the 10th cycle (right).

A study made by Häring *et al.* [32] on the thickness evolution of nickel hydroxide during similar CV measurements under AFM monitoring suggested that the material swells when intercalated, and shrinks when charges are removed. Also, overtime, the thickness was seen to decrease, as aged NiOOH possesses a more compact structure (higher density) when water is removed. However, since AFM measurements only show relative thickness variations from a starting point, the total thickness was not studied in their publication. These observations are nevertheless in accordance with the results shown in Figure 4-12 as the thickness is shown to equally decrease in both the bleached and the colored states by around 2 nm during the first 10 cycles. Indeed, the initial film thickness of the bleached state starts at ~197 nm and finishes at ~195 nm, while the colored state shows a similar decrease but starting with thickness values which are ~2 nm lower. The 10th cycle thickness variation has also been analysed in more detail (see right side of Figure 4-12) to observe the swelling and shrinking behaviour. The obtained hysteresis behavior is similar to the one

observed during the analysis of the optical properties and confirms that charge insertion does indeed lead to swelling of the NiOOH film.

4.5 Physical properties

To further understand the optical and electrochemical observations, a structural and compositional characterization of the as deposited and cycled films was performed. A series of GIXRD measurements were made to observe the crystallinity of the films (see Fig. 4-13).

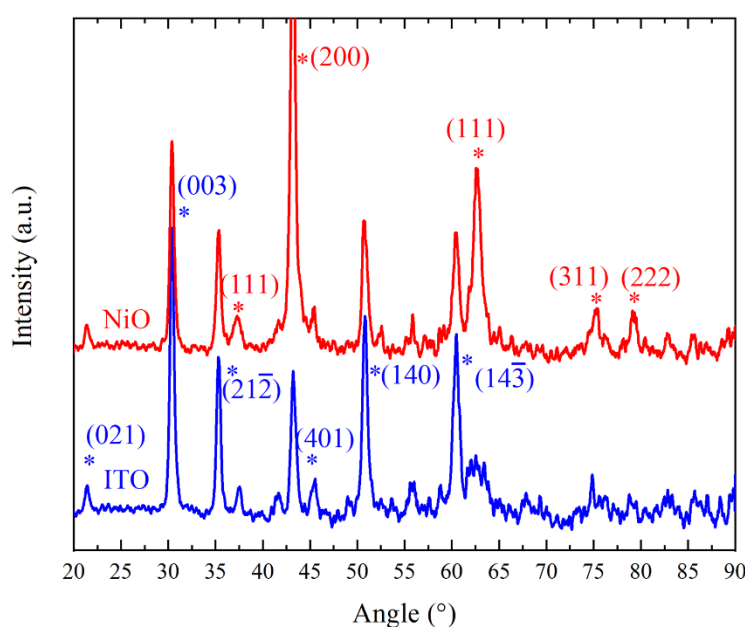


Figure 4-13 : GIXRD diffractograms of NiO (190 nm) deposited on ITO (18 nm) in red and of the a masked region of the substrate containing only the ITO film in blue.

Due to the high number of peaks coming from the ITO film, a measurement of a masked region of the surface (only ITO) was performed to be able to clearly assess its contribution to the diffractogram. As a low peak intensity was expected due to NiO's low crystallinity, in part due to its short-range order, the GIXRD configuration was chosen instead of the $\theta/2\theta$ to maximize the number of diffracting planes (not being limited to the planes parallel to the surface). From the results shown in Figure 4-13, it is possible to conclude that the as deposited NiO film has a Fm3m face centered cubic structure, as expected from similar studies [28]. The charts used to identify the

peaks were taken from the International Centre for Diffraction Data (NiO: 00-44-1159, ITO: 01-088-0773).

The film's composition was obtained by RBS (see Fig. 4-13) specifically looking at the Ni to O ratio. ERD measurements were also performed for the H content.

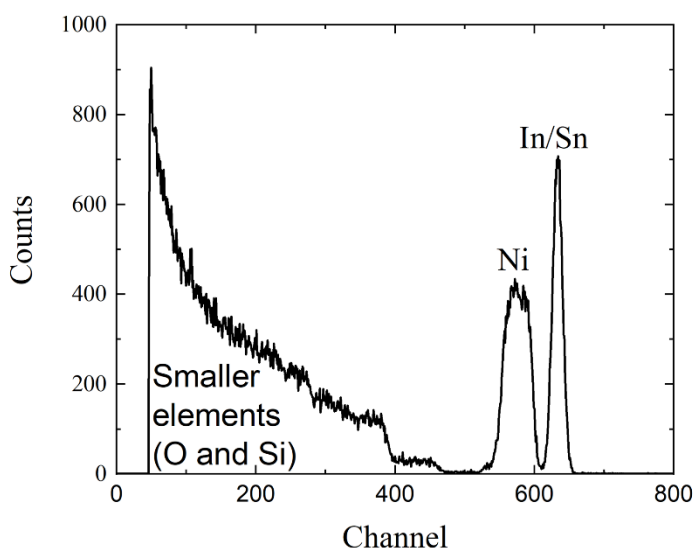


Figure 4-14 : Rutherford backscattering measurements made on a as deposited NiOOH film. No significant compositional variation was observed before and after cycling.

With traces of indium due to the underlying thin ITO electrode (~ 18 nm), and silicon coming from the substrate, the main elements present in the studied film are nickel and oxygen. Modeling based on these results suggest roughly a 2:1 O to Ni ratio which is indicative that the film has reacted with hydroxide. To obtain the total atomic density, the amount of hydrogen was also quantified (see Figure 4-14).

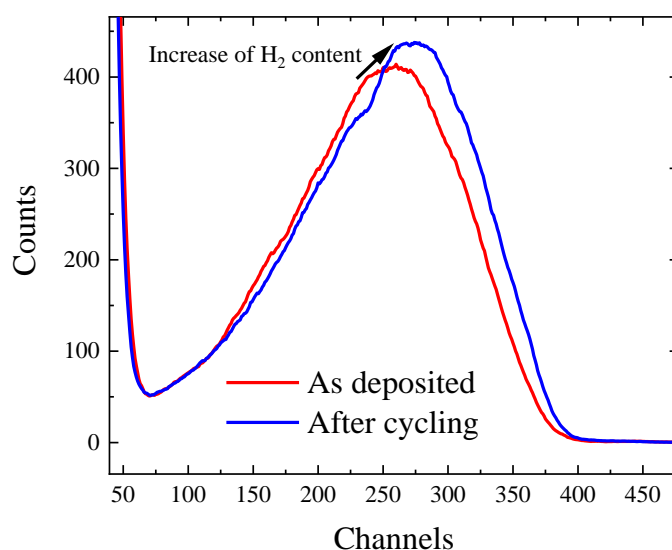


Figure 4-15 : Elastic recoil detection measurements of the NiOOH film showing the hydrogen content evolution before and after cycling.

With the ERD measurements of Figure 4-15, the stoichiometry of the film is established to $\text{Ni}_{0.265}\text{O}_{0.53}\text{H}_{0.205}$ with a density of 3.55 g/cm^3 considering a 179 nm thick film (as established from *ex situ* optical measurements). In the literature, the reported densities of α -NiOOH and β -NiOOH are respectively between 2.6 g/cm^3 and 2.8 g/cm^3 and between 3.65 g/cm^3 and 4.15 g/cm^3 [20], suggesting that the measured film is composed of a mix of α and β phases. Other factors can influence the density of the material, such as porosity. To obtain a more accurate and representative density of each phase, measurements on fully dehydrated and hydrated samples should be performed; however, such measurements would require ion beam analysis on samples in a liquid environment, which would be complex. Nevertheless, using the density to estimate the number of oxygen atoms in the film, which correspond to intercalation sites [30], it is possible to establish the intercalation level by comparing the oxygen concentration with the electron concentration taken from the inserted charge values in CV measurements. This estimation relies on assuming that each inserted electron is coupled with a hydrogen ion at an intercalation site and that the oxygen concentration is stable as a function of cycling.

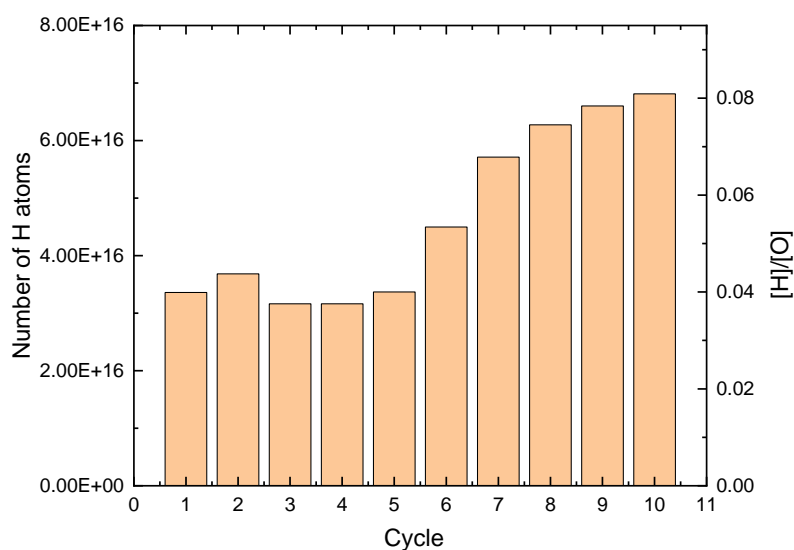


Figure 4-16: Number of intercalated hydrogen atoms compared to the number of intercalation sites for the first 10 cycles.

As expected, as the amount of inserted charge increases as a function of cycling, the intercalation ratio increases accordingly as a result of the ageing process. When water “unzips” the interplanar spaces in the film, more intercalation sites are made accessible to ions. However, as the intercalation ratio saturates at 8%, the present estimation indicates that a great many sites are still not occupied or simply not accessible after the phase transformation.

CHAPTER 5 ALL-SOLID-STATE DEVICES DESIGN AND FABRICATION

5.1 Foreword

This chapter is dedicated to the design, fabrication and characterization of electrochromic-based devices. While the study of each individual material of an ASSD was one of the main objectives of the project, their integration into a functional device was the most demanding one. Indeed, multiple critical elements during fabrication were found to lead to device failure, and as such also constitute an important part of the chapter. The basic designs and materials are first covered, followed by the measured performance of the devices. Finally, the chapter will be concluded by a general discussion on device reproducibility and alternative designs.

5.2 Device design and optimization

Considering the overview given on ASSDs in Section 2.2.4, the first step towards the fabrication of a device was obviously the deposition of each individual material, the characterization of its optical, EC and physical properties, as well as its optimization. The chosen architecture was the one shown in Figure 2-11b, for two main reasons: 1) the fabrication of ASSDs with thick electrolytes requires additional fabrication steps and an installation not available at our partner's production facilities, and 2) at the beginning of the project, we had limited tools for modeling thick media within a stack. Indeed, light coherence inside a layer is assumed when using the matrix approach (see Section 3.3.3.2) to model interference filters. As a result, media thicker than the coherence length (30 μm for a mercury lamp [60]) cannot be modeled. The materials which were used and their respective roles are listed in Table 3-3 along with their deposition conditions.

At the start of the project, preliminary models were made using a homemade *Matlab* program with the refractive index of the materials taken from literature in order to confirm that the reflection increase was possible with the suggested architecture.

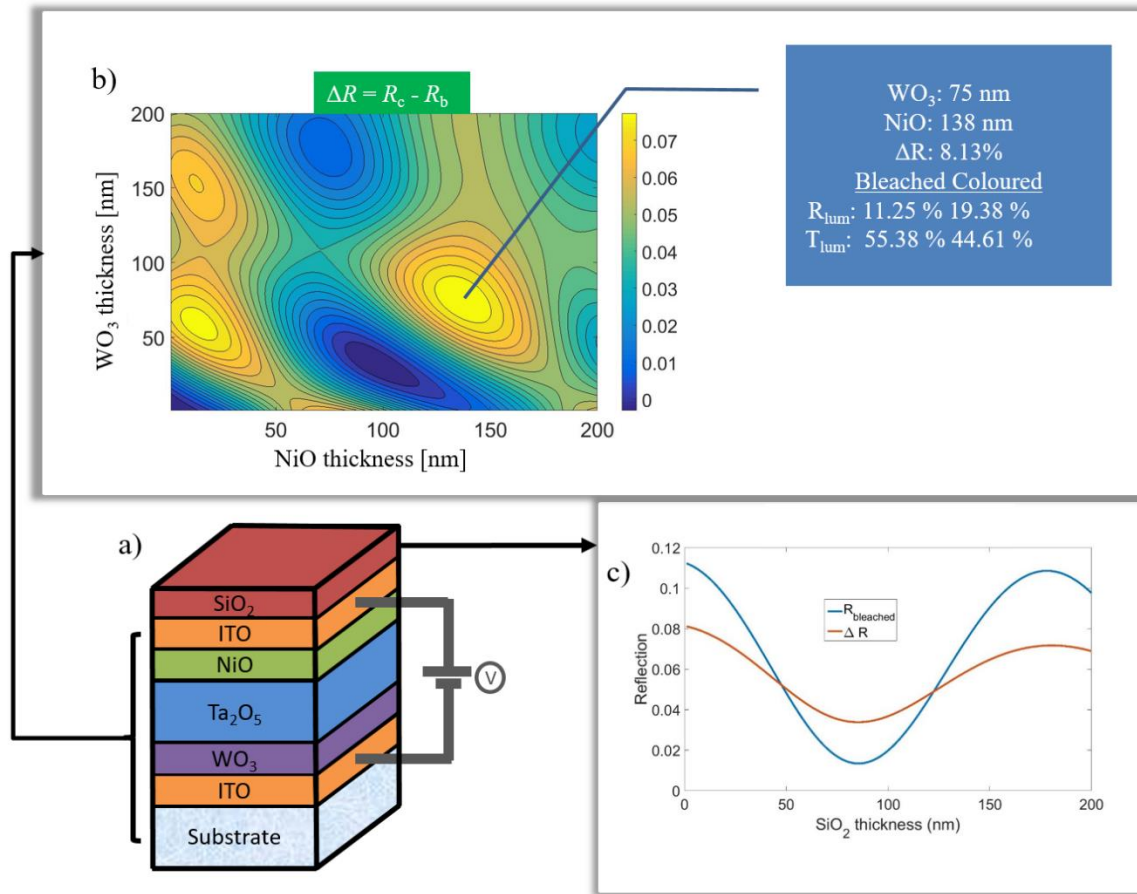


Figure 5-1 : a) adopted ASSD structure for b) reflection variation optimisation through coloration of the EC materials depending on their thicknesses (top SiO₂ thickness equal to zero). c) Shows the modeled effect of the addition of a SiO₂ layer on top of the device.

Figure 5-1 shows the variation of the spectral parameters for a bleached and colored ASSD. The device shown is composed of ITO layers of 20 nm, a Ta₂O₅ layer of 200 nm, varying EC layer thicknesses and a 2 mm B270 substrate. An optimal reflection variation of 8.13% is found when implementing a 75 nm film of WO₃ and a 138 nm film of NiO, with a bleached state reflectivity of 11.25 %. In an attempt to decrease the bleach state reflection, modeling the impact of the addition of a silica layer on top of the device is detailed in Figure 5-1c, where a minimum in the bleached reflectivity of 1% is obtained with a 82 nm thick layer, at the expense, unfortunately, of a 4% drop in reflectivity variation. However, it is to be noted that such modeling was performed with optical properties taken from literature, and thus, the characterization of each deposited material in our facilities was yet needed for modeling of a more representative stack.

As previously indicated, the EC layers' deposition conditions were optimized to obtain the highest CE. In the case of the electrolytes, they were optimized first with the aim of minimizing their absorption. However, porosity of the films is also known to impact the ion diffusion coefficient, hence why the deposition parameters were also tuned to yield a sufficiently dense (low pressure) and transparent (gas proportion) electrolyte film. As the coloration speed was not a critical parameter in the present project, the best electronic insulating devices were composed of a relatively porous (low refractive index) Ta₂O₅ layer followed by a dense silica layer of more than 150 nm in thickness. This architecture was chosen to minimize the electronic short-circuits and maximize the coloration speed.

The top ITO electrode fabrication proved to be critical for device functionality, as the surface resistivity was often too high to allow charge accumulation for intercalation. Two physical parameters influence an ITO film's resistivity ρ : the carrier concentration N and their mobility μ . With a fixed N corresponding to the concentration of Sn atoms in the ITO structure, the tunable parameter allowing to lower ρ is μ . The latter is affected by physical parameters such as the presence of vacancies, holes, pores, dislocations, grain and phase boundaries, and as such, microstructures with lower defect levels yield a higher conductivity [61]. To decrease the number of defects and increase the carrier's mobility, a high deposition temperature and/or biasing are typically added during deposition, and/or a post-annealing process performed afterwards. In the present case, the power density was kept low due to the limited thermal capacity of the ceramic target's bonding agent and a low substrate temperature was required to allow deposition onto polymer substrates. Biasing during deposition was tested as well, but no significant improvement was observed for bias values going from -50 V to -300 V. However, while the deposited ITO films could still have been improved in terms of their conductivity and transparency, they were sufficiently conductive for the size of the devices under study and their extinction coefficient below 0.24 at 550 nm lead to a reasonably low absorption (4% for a 15 nm film). The film's thickness was limited to 15-30 nm, as a minimum thickness was needed for it to be conductive, but too thick of a layer resulted in an increase in short-circuits through the device. By assuming that nano and micro particles present on the surface before deposition are creating pinholes through the electrolyte (see section 3.2.1.1), the more conductive material is deposited on top of the stack, the higher are the chances of contacting the bottom electrode. As a result, the thickness of the top ITO layer was found to be critical. Indeed, for films with thicknesses above 30 nm, it was observed that most

devices were non-functional. Therefore, a significant amount of time was dedicated to optimizing the deposition conditions of the ITO film in order to increase its conductivity and maintain a low sheet resistance at lower thicknesses.

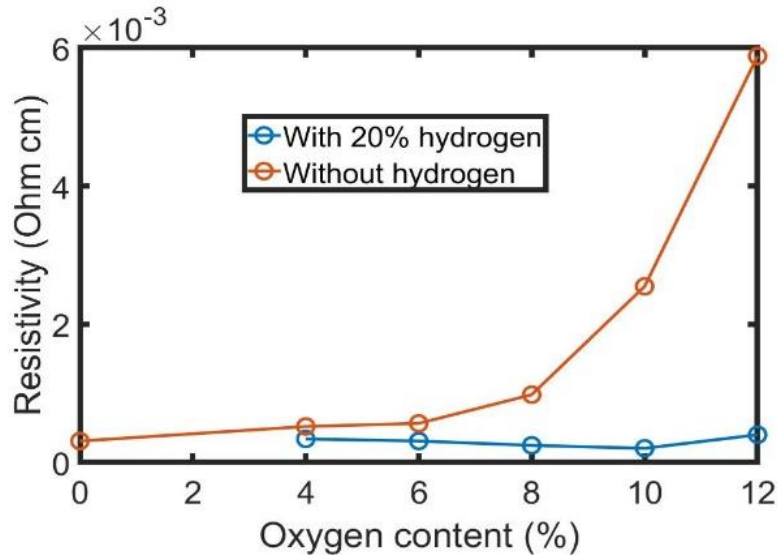


Figure 5-2 : Resistivity variation of 100-nm-thick ITO films depending on the oxygen and hydrogen contents.

The addition of oxygen [61] and hydrogen [62] proved to be helpful while depositing ITO at low temperature by increasing the carrier concentration. From Figure 5-2, a study of the gas composition (oxygen and hydrogen) was undertaken to decrease the resistivity of the ITO films. At a concentration of 10% oxygen, 20% hydrogen and 70% argon, the deposited films were slightly less resistive ($2 \times 10^{-4} \Omega \text{ cm}$ vs $3 \times 10^{-4} \Omega \text{ cm}$) than the films deposited under 100% argon. However, films deposited with no added reactive gases were more stable after deposition, as the films fabricated with oxygen and hydrogen, while initially more conductive, lost their conductivity after approximately 24 h.

Apart from optimizing the conductivity of the topmost ITO layer, minimizing short-circuits occurring through the device was another challenge to fabricate a functional ASSD. To further reduce short-circuits, the device was patterned to remove any risk of contact between the top and bottom electrodes.

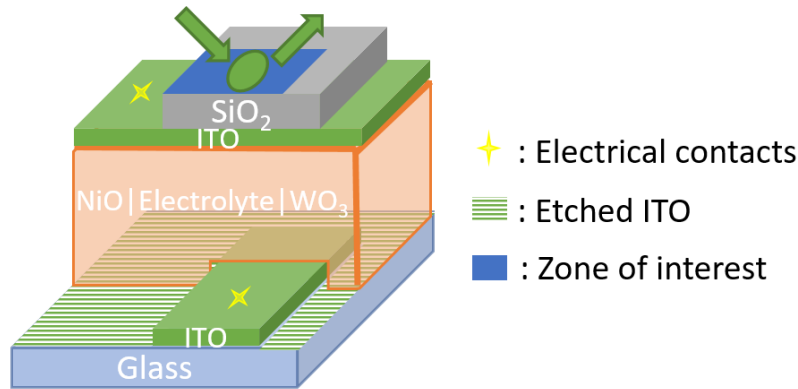


Figure 5-3 : Device patterning to optimize electrical properties and minimize the possibility of short circuits.

The patterning shown in Figure 5-3 was obtained with the following methodology: Before deposition, a thin region touching only one edge was masked (bottom green layer in Figure 5-3) and etched under an argon bias of -600 V for 30 minutes to completely remove the unmasked ITO. The sample was then cleaned using the method described in section 3.2.1.2 and masked once again on the part not covered by the orange section; this allowed to maintain a direct contact with the bottom electrode. After fabricating the ASSD ($\text{NiO} \mid \text{Ta}_2\text{O}_5 \mid \text{SiO}_2 \mid \text{WO}_3 \mid \text{ITO}$), the sample was taken out and masked along the section on the top left to allow for a direct electrical contact with the top ITO film (top green layer). Finally, any additional films required to complete the optical performance requirements of the device were added. This patterning is crucial for the device performance, as it removes edges (top ITO contacting bottom ITO on the sides of the device) and stack piercing (probe piercing the device and contacting directly the bottom ITO when applying the potential) effects that can increase as well as generate additional short circuits.

Having optimized and characterized the optical properties of all required materials, and demonstrated the functionality of the chosen architecture, it was now time to proceed with the design and optimization of the optical performance of the ASSD using the matrix approach presented in section 3.3.3.2; i.e. obtain a low reflection (antireflective behaviour) in the bleached state and ideally, a 10% increase in reflection in the colored state, by tuning the thicknesses of each layer. To do so, traditionally, *OpenFilters* was the software of choice, as it possesses the ability of tuning the thickness of every layer in order to comply to specified optical requirements (targets), such as a specific transmission, reflection and absorption at given wavelengths. While useful to model and design an antireflective stack, the software does not allow the use of dynamic materials

whose optical properties possess more than one state. As such, it was not possible to optimize the overall performance of an EC filter while considering its performance in two different states simultaneously (low R in the bleached state as well as high R in the colored state). This was the main reason for the development of a homemade *Matlab* program which considered the optical properties of the EC materials in both their states. The main difference between the developed code and *OpenFilters* is, however, the optimization strategy. In the *Matlab* code, every configuration for a specified range of thickness values is considered and thus constitutes a “brute force approach”, a process that can take hours of calculation but which allows one to find the optimal solution. More precisely, a given thickness range for two or more layers is specified, the corresponding spectral properties of the resulting stack are calculated in the bleached and colored states, the data saved at every iteration and then displayed in the form of 2D maps. In *OpenFilters*, a selective approach based on gradient calculations (Levenberg–Marquardt algorithm) converging on local minima for a given set of optical targets is adopted, a process which is significantly faster but which may not result in finding the optimal solution. The high computational times limit the brute force approach to the variation in thickness of a limited number of layers at a time, as adding too many layers increases the calculation time exponentially. However, it was nevertheless possible to easily repeat the calculations for materials having different optical properties, allowing the calculation of the reflectivity variation upon coloration. Without the ability to simultaneously consider the thickness of every material in a stack for the modeling of an optimal configuration, as well as considering multiple optical states for the EC materials, finding of a more suitable tool was needed. *Essential Macleod*, as suggested by our partner *Essilor*, was the chosen software, as it uses a similar approach as *OpenFilters* with the added benefit of allowing for the incorporation of dynamic materials. More precisely, the software was used to tune the thickness of every layer of the stack within specified ranges in order to obtain the lowest R_{lum} when NiO and WO₃ are in their bleached state, as well as having the highest R_{lum} when they are both colored. Subsequently, we first proposed an architecture without Ta₂O₅, and where the position of the NiO and WO₃ were interchanged in the stack (reasons explained in the next section) – this allowed us to optimize the optical response of the ASSD along with the proposed limitations on the thicknesses.

Table 5-1 : Physical thicknesses of optimal modeled ASSD with their restrictions.

Material	Thickness (nm)	Minimum thickness (nm)	Maximum thickness (nm)
SiO₂	90	50	150
ITO	30	15	30
WO₃	150	150	300
SiO₂	255	150	300
NiO	100	100	300
ITO	82	-	
B270	2x10 ⁶		

The thicknesses from Table 5-1 were obtained using *Essential MacLeod* by considering imposed targets and restrictions in the colored and bleached states. In this case, the varied parameter was the layers' thickness to optimize two optical targets: The first target applied to the bleached state reflectivity with the criteria of minimizing R_{lum} (the luminous reflectance), and the second target applied to the colored state, with the criteria of maximizing R_{lum} . The thicknesses were kept in the range where we observed the best performance regarding short-circuits (thick electrolyte, thin top electrode).

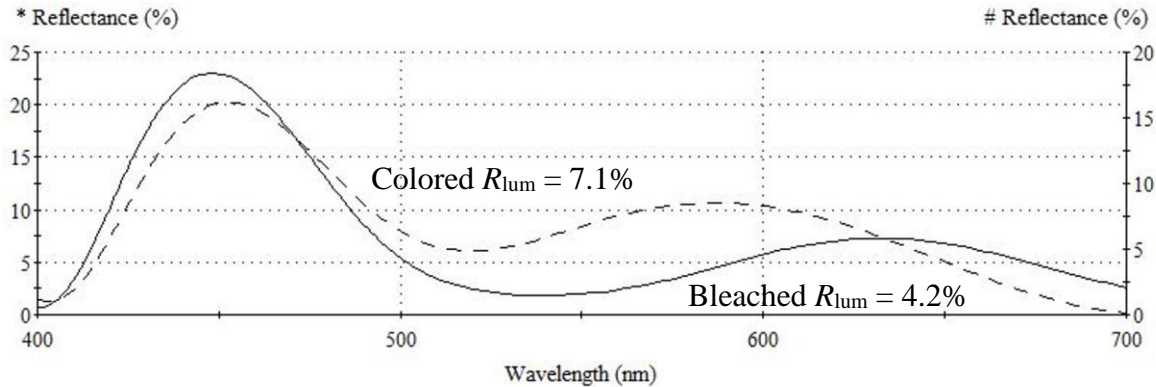


Figure 5-4 : Reflectance spectra of a modeled ASSD based on the thicknesses shown in Table 5-1. The full curve represents the bleached state (left axis) and the dashed curve the colored state (right axis).

The R_{lum} variation of Figure 5-4 is mainly the result of interference effects. As EC materials tend to be less reflective when colored (see Figure 4-1 for NiO, for example), the strategy employed was to design an antireflective (AR) filter where the optical thickness changes in the colored state lead to the loss of the AR properties (by varying the optical path in the EC layers). In the spectra above, the reflectance minimum blueshifts when the device is colored, from around 545 nm to 520 nm, due to the reduction of the optical thickness (OT) (from ~505 nm to ~485 nm). As the maximum sensitivity of the human eye is centered at 555 nm, the spectral variations in this region have a larger impact on R_{lum} . Using this modeling approach, we predicted a R_{lum} variation from 4.2% up to 7.1% when passing to the colored state (with the backside reflection considered). At this point, this reflectivity behavior is close but does not meet the required performance ($< 1\%$ R_{lum} in the bleached state and $> 10\%$ ΔR_{lum} in the colored state without considering the backside reflection), but it proves that such an increase in reflectivity is possible. Permutating the NiO and WO_3 layers proved to help the reflectivity increase, but in our observations, the growth of a conductive ITO layer on top of NiO was harder to achieve (subject treated in the following section).

5.3 Fabrication and characterization

In this section, the steps towards fabrication and characterization of a functional ASSD are discussed, along with the observations made during coloration and bleaching. As many parameters can affect the overall dynamics of ion displacement in the device, quantitative and qualitative

approaches were used to understand in further detail the coloration behavior in order to develop more precise models for optimization.

5.3.1 Filters deposited on the MAG-4 system

The first devices were fabricated using the MAG-4 system with thickness control by time monitoring, i.e. the films were deposited individually and characterized optically *a posteriori* to obtain their thickness and thus calibrate the deposition rate. However, since the deposition rate can vary as a function of time (evolution of the oxidation state of the target during reactive sputtering), an error, depending on the deposited material (low error (1-2%) for SiO₂, significantly higher error (40-60%) for NiO) was observed on the predicted thickness, as target poisoning with reactive oxygen can affect the sputtering yield, implying that ideally *in situ* monitoring should be implemented to reduce the error. Attempts were nevertheless made to fabricate ASSDs with the desired optical properties by depositing one layer at a time and characterizing the stack optically by ellipsometry and spectrophotometry at each deposition step. This technique allowed for a re-optimization of the stack following the measured thickness errors. For example, as the original design was modified, devices with a low reflectivity in the bleached state were still possible to obtain by modifying the thicknesses of the topmost remaining layers. The original device architecture was substrate | ITO | WO₃ | Ta₂O₅ | NiO | ITO, as tantalum oxide was the first studied electrolyte (it was later replaced by silica that proved to function better as the electrolyte).

Having the optical properties for every deposited material as well as the dynamic properties of the EC obtained during CV measurements, the performances of the fabricated devices in the MAG-4 system could be modeled.

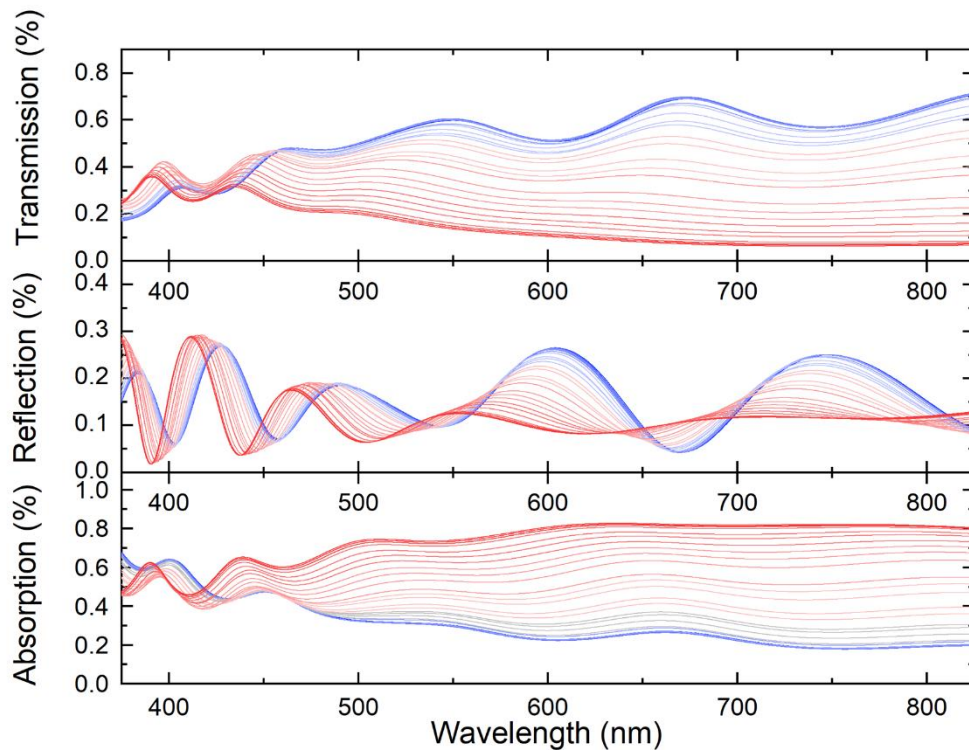


Figure 5-5 : Modeled spectral transmission, reflection and absorption intensities of an ASSD fabricated in the MAG-4 going from a bleached state (blue) to a colored state (red).

The device architecture shown in Figure 5-5 is of Glass (2 mm) | ITO (18 nm) | WO_3 (300 nm) | Ta_2O_5 (300 nm) | SiO_2 (50 nm) | NiO (150 nm) | ITO (100 nm). Silica was added in the electrolyte at this point because it proved to help with the electronic insulation when added above tantalum. The purpose of this stack was not to make an AR device, but to confirm functionality and model matching. From these modeling results, it can be observed that the transmission varies from 60% to 14% at 550 nm. Correspondingly, the absorption goes up from 30% to 75%. Regarding the reflection spectra, when coloring, the interference fringes are seen to shrink in amplitude, as less light is reflected at the interfaces below NiO due to its higher absorption, minimizing the interferential effects in the stack. The reflective behavior in the colored state is then mainly dependent on the air/ITO and ITO/NiO interfaces.

In order to measure the properties of the deposited ASSDs, the samples were installed in the UMA of the Carry 7000 spectrophotometer in order to establish the measure R_{lum} , T_{lum} and A_{lum} , and a fixed voltage of ± 5 V applied on the electrodes using a Keithley power supply.

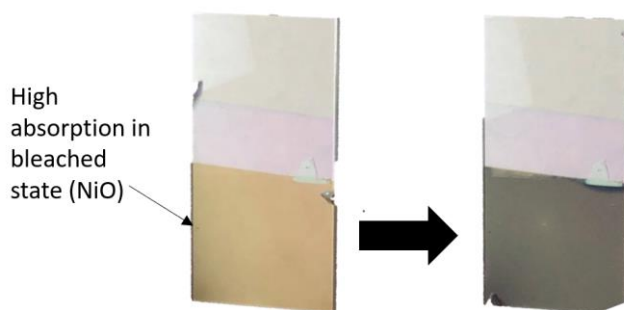


Figure 5-6 : Coloration of an ASSD deposited in the MAG-4 system.

While being active, the ASSD fabricated in the MAG-4 system was less absorbing than predicted in the bleached state (see Figure 5-6), suggesting that the EC materials, mainly the NiO as its residual color is brownish, does not possess the same optical properties when activated in liquid vs. solid environments. This phenomenon was observed in the study presented in Chapter 4 on the activation of nickel oxide when submerged in a liquid. The main identified reason why an optical mismatch is observed is that the structural state of the anodic EC material evolves upon reaction, affecting its absorptive properties. The transformations responsible are both the reaction of NiO with hydroxides and the effect of ageing, while in a solid environment these effects do not occur.

After 3-4 days of exposure to the atmosphere, the top electrode was no longer conductive, suggesting an evolution of the composition of the deposited ITO. In fact, this specific ITO was deposited with the addition of hydrogen in the gas mixture, as studies in the literature [63] have suggested an increase in conductivity when protons are inserted, increasing the amount of available carriers. However, in the present case, the relatively high amounts of hydrogen which were used (20%) may explain the resulting instability of the films.

Table 5-2 : Optical performance of the ASSD deposited on the MAG-4 system in comparison to the predicted modeled values.

	Modeled		Measured		Difference	
	Bleached	Colored	Bleached	Colored	Bleached	Colored
R_{lum} (%)	16.1	10.3	17.0	14.5	0.9	4.2

T_{lum} (%)	55.5	13.8	72.6	11.3	17.1	2.5
A_{lum} (%)	28.5	75.8	10.4	74.2	18.1	1.6

The expected values for the bleached and colored states of the deposited device differ significantly (see Table 5-2). This mismatch suggests that the optical properties of the individual EC materials are not the same as those when they are integrated into a device. More precisely, when depositing layers on top of the EC layers (where ions are inserted during deposition), coloration (NiO) and decoloration (WO₃) of the pre-intercalated films was observed corresponding to charge desorption. This phenomenon was quantified and documented by an increase of the gradient (~8%) on the Tauc-Lorentz oscillator intensity of the NiO film after depositing the Ta₂O₅ electrolyte above it. This was also observed as a decrease of the near-infrared Gaussian oscillator intensity (at ~1000 nm) in the WO₃ model (50-90%) following ITO deposition, suggesting that WO₃ is more affected than NiO during the device fabrication. Indeed, as charge density diminished due to ion desorption, device functionality is *a priori* affected. In addition, some devices showed a larger coloration the day after their deposition. This may be the result of the absorption of water from the ambient air which, upon application of a voltage, is dissociated into H⁺ and OH⁻, the former becoming a potential source of ions in the device as observed by Deb in his first publication [21]. To be able to fully predict the optical behaviour of an EC filter, a more in depth study of the charges in play could be of use to correlate a specific optical state to a precise amount of inserted charge (like in the CV experiments). By knowing the number of intercalation sites (surface density, obtained by RBS, times the thickness) and by measuring the current during the application of a specific voltage, which, on an EC device should slowly decrease until a null or low and constant value is obtained (all accessible intercalation sites being occupied), it would be possible to calculate the intercalation level of the EC layers. Doing so would allow us to determine the level of coloration of each individual material, therefore allowing the corresponding specific optical states to be included in the models. However, due to short-circuits, the current never reaches zero, making this type of calculation more complex, as a part of the inserted charges are not involved in the intercalation process. Also, being affected by water, the coloration does not depend on only the amount of inserted charges but also on the amount of H₂O molecules inserted into the device, making it harder to establish a charge-dependant dynamic optical model based on the coloration level. One could

thus imagine performing these measurements under a controlled low water content atmosphere. Solutions to these problems exist and are discussed in Chapter 6.

The other material whose properties changed when deposited into the stack was the top ITO layer. When the growth occurred on flat surfaces (e.g., B270 glass substrate), the film displayed a good conductivity ($\sim 100\ \Omega$ on the surface as measured with an ohmmeter), but when deposited onto NiO, the films were no longer conductive enough to allow the device to work properly (surface resistance $> 1\ \text{k}\Omega$). As nickel oxide films are known to have a high surface roughness [32], we proceeded to treat the surface by using a plasma, as similar treatments were performed by Vernhes *et al.* (ion bombardment of a $\text{SiN}_x\text{:H}$ film with 40 mTorr of Ar) [52] to reduce the surface roughness by densifying the top part of the film as discussed in Section 3.2.3.

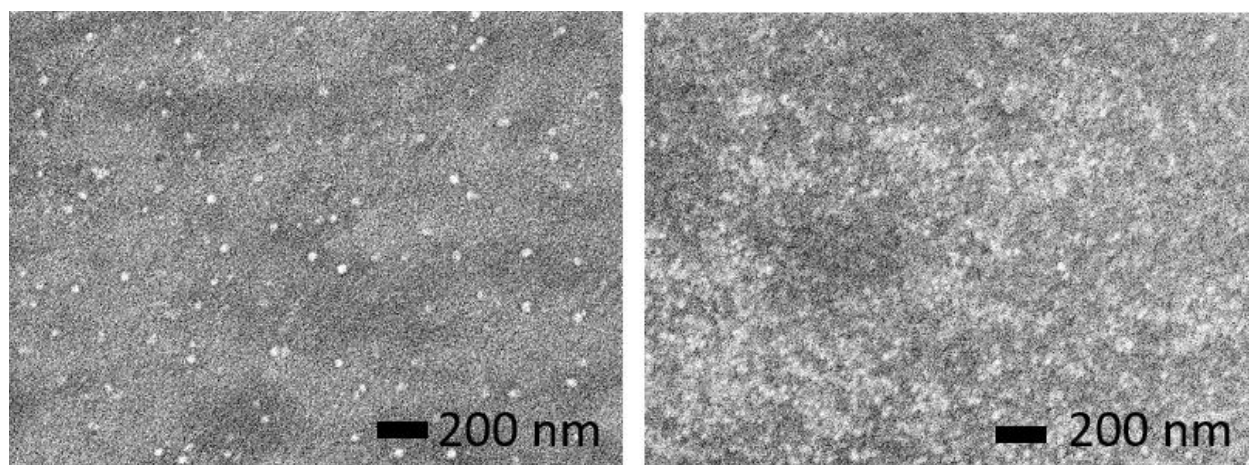


Figure 5-7 : SEM images showing an untreated NiO surface with large particles ($\sim 50\ \text{nm}$) (left) and defect free ion bombarded surface (right).

To understand why the ITO top layer was less conductive when deposited over NiO in comparison to glass, SEM images were taken to study the topography of an untreated NiO surface and of a plasma treated NiO surface. From Figure 5-7, large particles (three-dimensional island growth mode [28]) of more than $50\ \text{nm}$ can be observed on the pristine NiO film, while none are present on the bombarded surface. While the SEM images do not allow for a clear observation of the impact of the plasma treatment, the surface resistance of the ITO nevertheless dropped from more than $1\ \text{k}\Omega$ when deposited onto untreated NiO down to $100\ \Omega$ when deposited onto treated NiO. Though the resistance between the top and bottom ITO layers was in the $\text{k}\Omega$ range, the untreated NiO device

was not active as the charges shorted through the electrolyte instead of accumulating at the surface. As the beneficial impact of the treatment was not as pronounced when depositing thicker ITO films, we conclude that the main culprit here is the surface roughness of the NiO film.

5.3.2 ASSDs deposited on the CMS-18 system

As the control over the layer thicknesses with the MAG-4 system was insufficient to fulfill the project's requirements, the depositions were transferred to the UHV CMS-18 system. The latter being fully automated as well as equipped with a load lock and *in situ* ellipsometer, it allowed for a higher level of control and reproducibility. Following the characterization of the individual materials of the device, preliminary devices were fabricated using similar, albeit adapted conditions from the MAG-4 processes. However, issues with the top ITO were still present, and ion bombardment of the NiO layer was, in this case, not sufficient to grow a conductive electrode. The proposed solution was to modify the structure of the ASSD by switching the position of the WO₃ and NiO layers, in which case the top ITO layer would be deposited onto WO₃. As the cathodic and anodic layers' position is in principle interchangeable, since they share a similar role in the device, no significant impact on the EC functionality was expected.

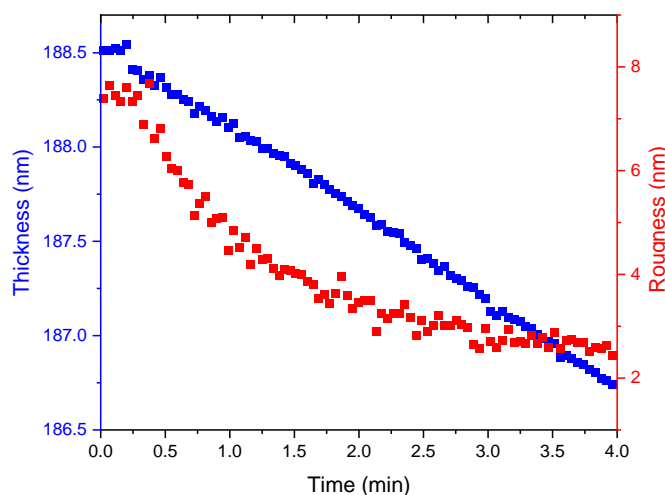


Figure 5-8 : Variation of the WO₃ film thickness and roughness as a function of time under exposure to an argon plasma at 5 mTorr and -600 V bias as measured by *in situ* ellipsometry.

The typical roughness of WO₃ films deposited at 14 mTorr is between 6 and 10 nm, which is much lower than what was modeled optically on the NiO films (40 nm – using a Bruggeman model).

Following an argon plasma treatment at 5 mTorr and -600 V, it was possible to lower the roughness to around 2 nm after 4 min at the expense of a 2 nm loss of material, as can be observed in Figure 5-8. The roughness variation can be attributed to diffusion, where the added energy supplied by the bombarding ions enhances the mobility of the surface atoms, allowing their relocation deeper below the surface, resulting in a denser structure [52]. Resputtering can also be involved in the process, where atoms on the substrate are ejected following the impact of an incoming Ar ion. The observed thinning of the WO_3 is thus the result of both densification and resputtering. This variation must be considered when depositing filters that require surface treatments, as the layer thickness is a critical parameter affecting the final optical performance.

Having treated the surface of the WO_3 , the subsequent deposited ITO films were conductive, and the devices were active. Note that a qualitative study was also undertaken following the electrode functionalization to establish the best electrolyte composition (between SiO_2 and Ta_2O_5). The main conclusion was that silica alone offered the best electronic insulating properties, where the addition of tantalum was not observed to reduce the conductivity between the top and bottom electrodes. If the resistivity between the top and the bottom electrode is lower than their individual surface resistivity, the ASSD functioning principle cannot occur, as electrons diffuse directly through the electrolyte instead of accumulating in the desired layers. This effect prevents ion displacement, therefore intercalation and coloration. The resulting and final structure, which was studied during this project, was thus: substrate | ITO | NiO | SiO_2 | WO_3 | ITO | SiO_2 .

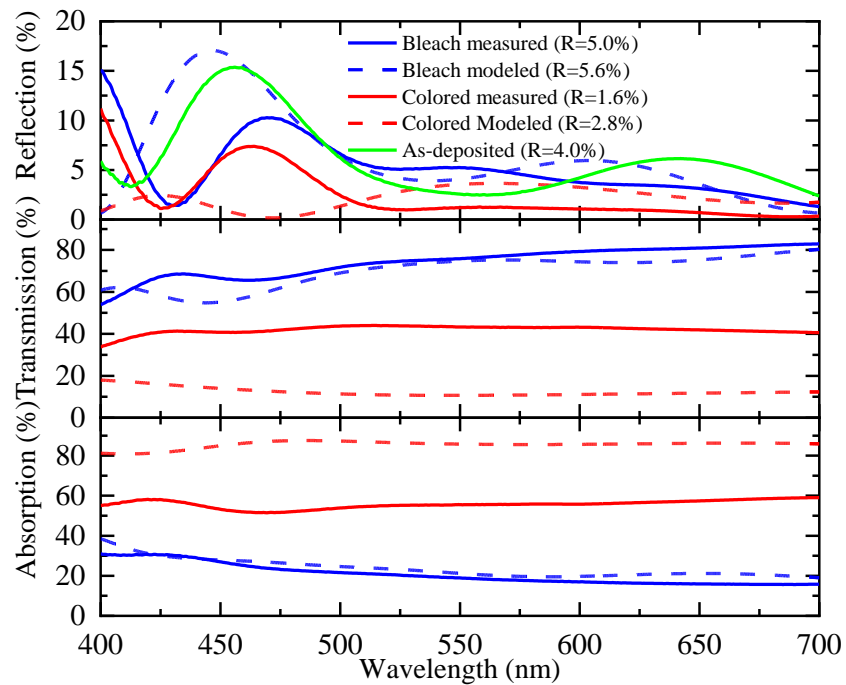


Figure 5-9 : Reflection, transmission and absorption in the visible area of a functional ASSD.

The architecture of the device from Figure 5-9 is composed of Glass (2 mm) | ITO (82 nm) | NiO (100 nm) | SiO₂ (255 nm) | WO₃ (150 nm) | ITO (30 nm) | SiO₂ (90 nm). The devices fabricated in the CMS-18 system were monitored using *in situ* ellipsometry to ensure a higher control over the thickness of the films. No rotation was possible when doing so, as the light beam requires a fixed surface; the result is a larger thickness inhomogeneity of the deposited layers. Nevertheless, as the *ex situ* characterization was performed in the same region on the sample as the monitoring beam, thickness gradients were not problematic for the optical measurements. However, for practical purposes, a uniform optical filter is required on the full surface of an ASSD, and thus, other means of monitoring which would allow substrate rotation should be considered in the near future. These include using a quartz crystal monitor or time monitoring in the case of optimized and more stable processes.

From Figure 5-9, the measured and modeled optical performances of the final device fabricated are shown. This device was not optimized for the project's objectives ($<1\%$ R_{lum} bleached, $>10\%$ ΔR_{lum} when coloring), as it was meant to be a proof of concept for the modeling approach's accuracy. However, a clear mismatch can be observed between the models and the experimental measurements for the colored state. Indeed, the reflection in the as-deposited state is close to the

modeled bleached state behavior; however, once colored, the bleached material does not completely regain its initial behavior. When comparing the measured reflections of the bleached and colored states, the effect is quite different from what has been modeled, as the coloration only lowers the intensity instead of shifting the reflection caused by the interferential fringes. Using the proper optical indices, the modeled variation of the optical path is expected to follow the experimental measurements, shifting the reflection maximum upon coloration from 525 nm to the center of the eye's maximum sensitivity (555 nm). However, in the presence of a different coloration mechanism and a lower amount of inserted charges (solid state), the optical evolution does not follow what was theoretically predicted.

When looking at the absorption/transmission curves, the modeled bleached state is close to the measured spectrum, but the coloration is less than expected. These observations indicate that the ASSD's coloration involves less charges than what was predicted with the *in situ* CV measured EC films, as the amount of pre-inserted charge during the deposition process is insufficient and/or short-circuits effects are affecting the intercalation capability. To create a better model for EC materials in the case of ASSDs, a new method had to be used to characterize the level of coloration, as the properties used in the previous model were taken from *in situ* cyclic voltammetry characterization.

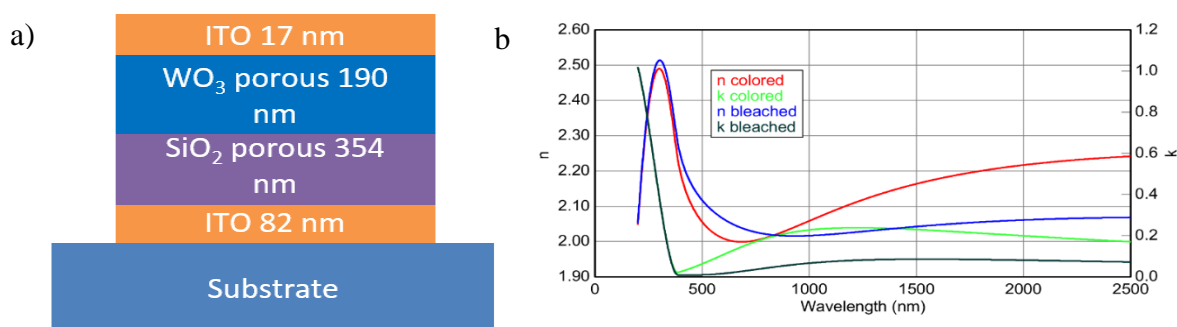


Figure 5-10 : ASSD based on one EC layer. a) adopted architecture of the device, and b) the resulting dispersion curves of the bleached and colored WO₃.

A device based on only one EC material was designed in an attempt to predict the performance and to fix the mismatch between what is modeled and measured. To do so, the NiO layer was removed from the stack and the electrolyte thickness increased for it to also act as an ion reservoir. The device was active, however incomplete bleaching of the WO₃ films was observed, as the extinction

coefficient was still quite high in the bleached state after the application of a positive potential. With the dispersion curves shown in Figure 5-10b, a potentially more accurate ASSD model can be made as the optical properties are obtained in the same solid state environment. The hypothesis here is that the coloration will be the same in every device (same n & k for the EC material under a certain potential). However, modifying the electrode/electrolyte will most likely affect the coloration, as the charge displacement will also be affected. Nevertheless, this approach can prove to be better than characterizing the EC materials in a liquid cell environment. In the case of WO_3 , the dispersion curves are rather similar to what was observed in the liquid cell and the material does not seem to be affected by the liquid environment. Attempts were made to reproduce this experiment with NiO deposited beneath the ion reservoir and without WO_3 , as ITO deposition onto NiO was unsuccessful.

As previously discussed, depending on the amount of short-circuits, a device can be functional (low defects density), functional with limited color variation and self bleaching effects (medium defects density), and dysfunctional (high defects density). The factor identified causing these effects are the pinholes caused by micro and nano particles (see Section 3.2.1.1).

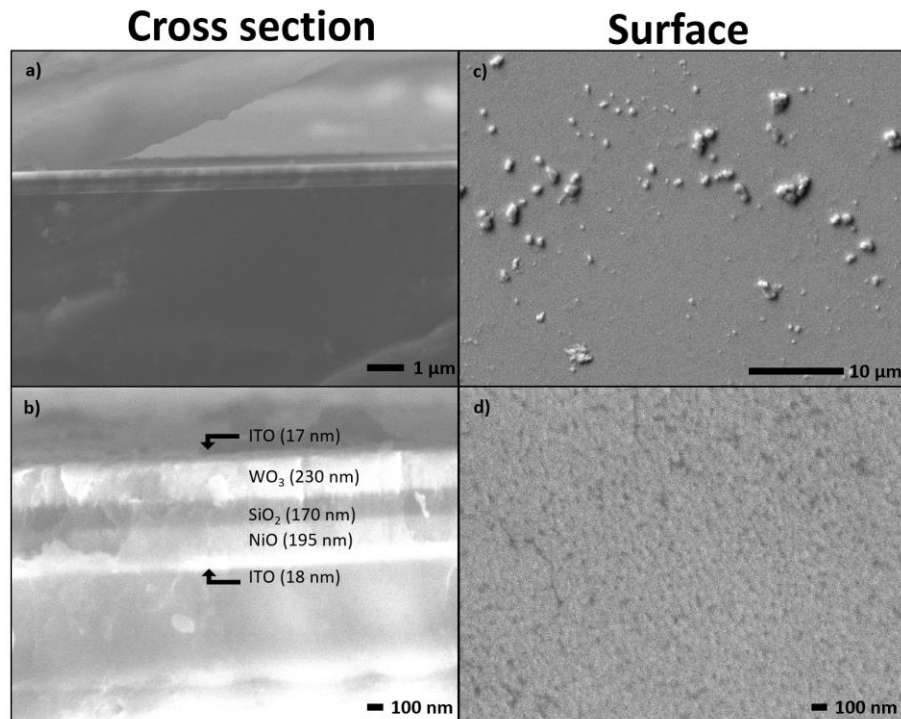


Figure 5-11 : SEM images of an ASSD following a CO_2 snow cleaning treatment: a) and b) the cross section, c) and d) the surface.

An SEM topographic study was made to understand what was causing device failures. The expected observations were the possible presence of particles and traces of cracks due to the stress induced during deposition. However, from Figure 5-11, no cracks are visible in the cross section of the stack. From the surface topography image (see Figure 5-11c), the main observed defects are micro-particles, such as dust or other residues coming from either the ambient air when transporting the substrate between the cleaning station and the deposition system, and/or during deposition processes (particles coming from the chamber walls during pumping). The corresponding defects are found both below and on top of the stack. This observation suggests that even with the most efficient cleaning method, when the substrate is exposed to suspended particles in the air, the presence of micro-particles is inevitable. A viable solution would be to deposit such samples in a clean room environment, thus minimizing surface contamination. In this respect, a portable mini-glove box compatible with the substrate cleaning station and with the CMS-18 load lock system would be a possible solution (see, for example, the air lock chambers from Cleanroom Synergy [64]).

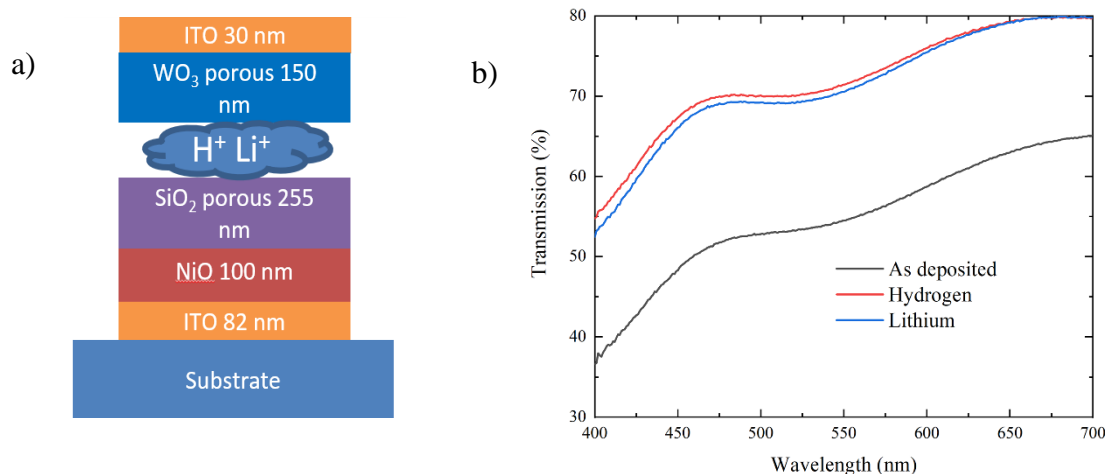


Figure 5-12 : Effect of the cyclic voltammetry pre-intercalation process (a) on the optical transmission spectra (b).

Another critical step that limited the performance of the fabricated devices was the lack of coloration without added water. Indeed, pouring DI water onto the surface of the devices was often necessary for activation, otherwise no coloration was observed. This effect has not been studied in detail, but a lack of charges in the devices was clearly distinguished in the previous section as the

fully colored state was always lower than what was expected/modeled (see Figure 5-9), even with the addition of hydrogen during the deposition. Other effects, such as a reaction of NiO with water, or the creation of stress upon immersion could be responsible for the activation, however, further studies would be needed to confirm these hypotheses.

In an effort to insert more charge into the devices the charges were pre-intercalated into the NiO film electrochemically after having deposited the SiO₂ electrolyte. In fact, the presence of the SiO₂ does not hinder the intercalation process and also helps to maintain the inserted charge within the NiO after removal from the liquid electrolyte.

As expected, the intercalation of either H⁺ (1 M KOH solution) or Li⁺ (1 M LiClO₄ in PC) ions causes an increase of the transmission (additional bleaching of the device) as shown in Fig. 5-10b. Interestingly, only a minimal difference is observed between the transmission spectra following intercalation of either hydrogen or lithium, and thus, the nature of the ion does not seem to impact the resulting optical properties of the film. Following the pre-intercalation process, the samples were rinsed, dried and completed with the deposition of the WO₃ and ITO films. Still, the final devices did not show any activity and also required water for activation. These results thus seem to invalidate the previous hypothesis of a lack of charges in the device and, as of now, no clear explanation for these observations is available. One assumption is that the charges are removed during the deposition of the last two layers. While some loss of charge is possible and expected when using H⁺ ions (see Figure 4-7), this should not be the case when using larger Li⁺ ions. On the other hand, both the NiO and WO₃ films were not optimized for Li⁺ ions and thus, their performance using such ions is difficult to predict in the present case. Finally, this procedure is common in the literature and additional experiments would be needed as the number of trial runs is insufficient to derive a straightforward explanation at this point.

CHAPTER 6 CONCLUSION AND RECOMMENDATIONS

6.1 Summary

The project was based on two objectives, the first being the design and fabrication of an EC ASSD that was antireflective in its bleached state (1.1), that showed an increase in reflection upon coloration (1.2) and possess a minimal absorption in the bleached state (1.3-1.4). To fabricate such a device, a magnetron sputtering process was chosen to deposit a thin film-based structure onto a glass substrate coated with ITO. The most suited cleaning method for the preparation of the substrate prior to deposition was by exposing the surface to a solid CO₂ flow to remove most dirt particles that are believed to be the main source of short circuits. This method was thus integrated into the group's facilities during this project. Following the substrate preparation, the deposition of nickel oxide, silica, tungsten oxide and ITO layers was monitored by *in situ* ellipsometry to ensure precise thickness control. Simply obtaining functional devices ended up requiring a significant amount of time and work and in the end, active devices with a low reflectivity (5.3%) in the bleached state were fabricated, fulfilling objective 1.1. However, upon coloration, the optical behavior was difficult to predict. As the dispersion curves of the EC materials used to model the impact of the coloration on the reflection spectrum were obtained from CV processes (liquid environment), the reflectivity variation differed from what was predicted when used in an ASSD (dry environment). In addition, it is difficult to obtain the exact amount of charges available within the ASSD and consequently choosing the most appropriate set of optical properties for both the NiO and WO₃. From the modeling tools used during this project, a theoretical increase of 3% in reflection was possible, however the measured reflection actually lowered after coloration by 1.6%, implying that objective 1.2 and 1.3 have not been met. It is also important to add that the bleached state absorption was quite high due to the nature of the deposited NiO, as it was optimized for η and not for its transparency; slight gains in transmission may thus be expected if optimizing for a lower absorption. Nevertheless, the absorption in the bleached state was of only 10-20% complying with objective 1.4.

Regarding the second main objective of the project, quite a few observations can be made with the results obtained from the study of the EC properties of nickel oxides films. First, to accurately build

an optical model, multiple measurements are needed. *Ex situ* measurements proved to be the best solution to build such models, as multiple angles and high-resolution measurements were taken, and they also allowed for spectra to be measured up to 2500 nm. However, to fully comprehend and quantify how the coloration of nickel oxide evolves when submerged in a KOH solution, an *in situ* approach was needed as we have clearly demonstrated. With this method, multiple dispersion curves as a function of the inserted charge were obtained, allowing for the quantification of the coloration depending on the inserted charge. Furthermore, while comparing each cycle, increasing trends for the optical and charge insertion were observed, an increase associated to a phase transformation from α -NiOOH to β -NiOOH. This transformation, termed ageing, represents the state of the material where water is absorbed in the interplanar spaces, modifying the density, and allowing ions access to intercalation sites. This effect has also been quantified in the thickness evolution of the films, as intercalation causes swelling while ageing reduces the overall thickness over time.

During the *in situ* CV experiments made on the nickel hydroxide films, a variation of 1.88 to 2.05 and 0.04 to 0.16 were observed in the refractive index and the extinction coefficient at 550 nm respectively upon coloration. The η corresponding to the optical change upon charge insertion evolved from 34.3 cm²/C to 57.3 cm²/C throughout cycling. The film thickness evolved from 197 nm in the first cycle to 195 nm in the last cycle, with a loss of 2 nm when deintercalated, with a surface roughness of 40 nm. This shrinkage is associated to ageing, where water is removed from the interplanar spaces. Following RBS and ERD characterization, the stoichiometry of the films was established to be Ni_{0.265}O_{0.53}H_{0.265} with a density of 3.55 g/cm³. Also, the intercalation ratio was estimated to reach a value of 4% up to 8% when going from the 1st to 10th cycle.

6.2 Perspectives

To further comprehend how the CV experiments affect NiO films, Raman spectroscopy and X-ray photoelectron spectroscopy could determine the effect of hydroxide reaction and ageing on the physical properties. The following logical steps in the study of nickel oxide's EC properties would be to characterize the long-term stability of the material and the ageing effect after stabilization. As the measurements of the first 10 first cycles do not clearly indicate a fully stabilized regime, it would be interesting to observe the behavior after hundreds of cycles. Furthermore, as ageing was the mechanism mainly studied here, overcharging and “drying” the film can also be of interest, as

the characterization of the phase transition back to the $\alpha \leftrightarrow \gamma$ pathway could help in the comprehension of the differences observed between *ex situ* and *in situ* measurements. Finally, as most EC devices are based on lithium intercalation, the study should also be performed in a LiClO_4 -PC solution and compared with the results obtained using a KOH solution. Also, instead of optimizing the films for the CE, the bleached state should be optimized (absorption minimized) with Li^+ ions to yield the most transparent films possible.

Regarding the continuation of the work on ASSDs, the most prominent path to follow would be to use the architecture shown in Figure 2-11a, which is to use a thick polymer as the electrolyte. This would slow down the coloration process, but it would palliate most issues related to short-circuits, as a thick (1-100 μm) electrolyte would bury all surface defects adsorbed during exposure to the ambient atmosphere following the cleaning procedure. This process was not initially considered for two reasons: the fabrication is more complicated than a conventional ASSD, and a thick media inside a stack was not easily taken into account in our filter design software. However, with the *Essential Macleod* software, one can include the fact that a medium is thicker than the coherence length of the light inside the stack, making the design and optimization of such a filter possible. To fabricate such device, the suggested process would be to individually deposit NiO and WO_3 over ITO coated substrates, spin coat a PMMA polymer [65] onto the EC layer and bond the substrates together with the PMMA surface touching each other with a bonder in an adhesive bonding lamination process. Both spin coater and a bonder are available in the microfabrication laboratory facilities.

As a significant amount of time was spent preventing/reducing the presence of short-circuits during the project, less time was spent on predicting the optical response of ASSDs. Indeed, as the measurements in the previous section showed, the modeled bleached and colored states did not match in most cases. The concept of fabricating a device based on only one active EC material was useful to increase the matching between measurements and models, and also to characterize the optical variation of WO_3 in an ASSD; however, the coloration behavior of NiO by itself was not measurable inside an ASSD.

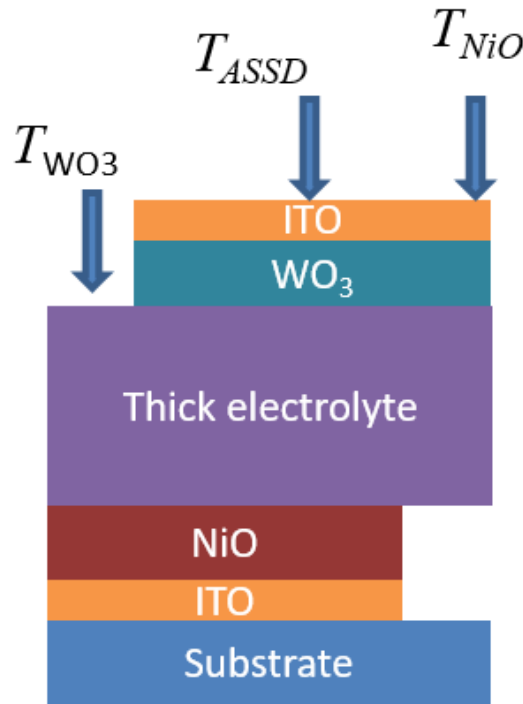


Figure 6-1 : Suggested ASSD structure to effectively measure the coloration properties of each EC materials.

In this respect, fabricating the ASSD shown in Figure 6-1 would technically allow for the measurement of the performance of both EC materials both separately and in tandem. Such a device would be optimal to accurately measure the effect of both anodic and cathodic layers on the transmission/reflection variation and to compare it with the modeled and expected spectra. In addition, it is expected that with the use of a thicker electrolyte, the performance would not be impacted by the presence of short-circuits which can limit the level of coloration.

As the project's objectives were oriented towards fabricating a device based on reflection variation, using materials whose coloration mechanisms are based on a transmission to absorption transition is not the most optimal solution. While the adopted solution is mainly based on using interference effects to vary the reflective properties, using a material that directly reflects upon coloration could be an alternative solution to achieve the objectives. A known material that exhibits such a behavior is Mg₄Ni, a cathodic electrochromic (and gasochromic) material [37, 63] that could replace the NiO layer in the current architecture. When intercalated, this material's optical behavior passes from mirror-like (high R and low T) to transparent (low R and higher T), with a lowly varying absorption [63]. The downsides of Mg₄Ni are that when exposed to higher temperatures (above

40°C) and humidity (80%), the film degrades and is less optically active. In addition, the fabrication process of such material is more complex. To prepare such films, a Mg target must be used, which is highly reactive with the ambient humidity (produces magnesium hydroxide and hydrogen) along with a nickel target in a co-sputtering process (simultaneous use of two magnetron during the deposition). As well, a thin (3 nm) layer of Pd is needed as a proton injector between the electrolyte and the Mg_4Ni layer. Nevertheless, as the EC properties of Mg_4Ni are best suited for this application, its study would be very attractive.

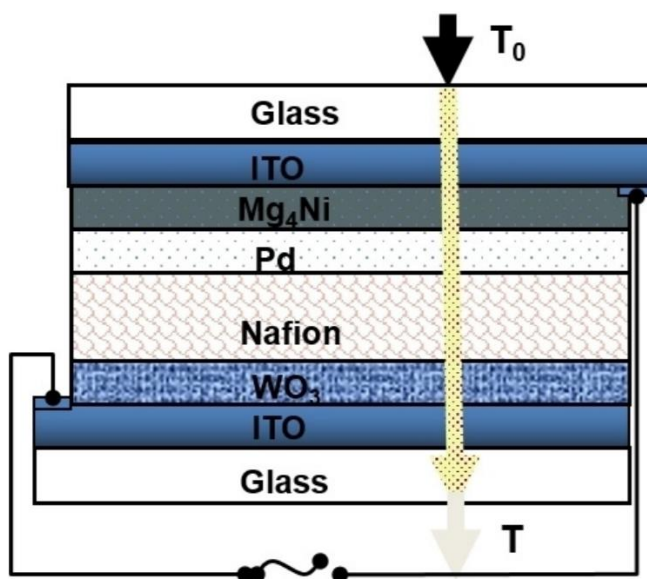


Figure 6-2 : Proposed architecture of a laminated ASSD composed of a Nafion (polymer) electrolyte and Mg_4Ni cathodic EC material. Imagen taken from [66].

Combining the two substrates laminated into a single device Li & *al.* proposed an ASSD architecture including a cathodic Mg_4Ni layer. Such a configuration could be a promising candidate to fulfill the present objectives.

The final design improvement that can be considered in the ASSD fabrication would be to improve the electrolyte itself. Instead of opting for the thick electrolyte solution, using a thin silica capping layer, a known effective electron insulator, conformally coated by atomic layer deposition (ALD) could also potentially help to prevent short-circuits. With sputtering and evaporation being highly directional deposition techniques (oriented particle flux), shadowing effects caused by the presence of defects are one of the reasons for the creation of pinholes [42]. One should keep in mind

however, that the film should not be ion insulating, which would otherwise render the device inactive. This approach is now being explored within FCSEL.

REFERENCES

- [1] C. G. Granqvist, S. Green and G. A. Niklasson, "Advances in chromogenic materials and devices," *Thin Solid Films*, pp. 3046-3053, 2010.
- [2] C. M. Lampert, "Chromogenic smart materials," *Materials today*, pp. 28-35, 2004.
- [3] A. Leitaó, "Electronic paper," Licenciatura Bolonha em Engenharia Electrónica, [Online]. Available:
<https://sites.google.com/site/fl1electronicpaper/Home/technology/electrochromic-technology>. [Accessed 15 06 2020].
- [4] A. M. Research, "Flat Panel Display Market by Technology (OLED, Quantum Dot, LED, LCD, and Others), Application (Smartphone & Tablet, Smart Wearable, Television & Digital Signage, PC & Laptop, Vehicle Display, and Others), and Industry Vertical (Healthcare, Retail, [...]," 2020. [Online]. Available:
<https://www.alliedmarketresearch.com/press-release/flat-panel-display-market.html>.
- [5] P. Monk, R. Mortimer and D. Rosseinsky, in *Electrochromism and Electrochromic Devices*, Cambridge University Press, 2007, pp. 25-32.
- [6] E. G. Market, "Electrochromic Glass Market by Material (Polymers, Nanocrystals, Viologens), Device (Windows, Mirror, Display), Application (Commercial, Residential, Transportation, Retail, Hospitality), and Geography - Global Forecast to 2020," May 2015. [Online]. Available: <https://www.marketsandmarkets.com/Market-Reports/electrochromic-glass-market-110534618.html>.
- [7] M. Boubekri, I. N. Cheung, B.A., K. J. Reid, C.-H. Wang and P. C. Zee, "Impact of Windows and Daylight Exposure on Overall Health and Sleep Quality of Office Workers: A Case-Control Pilot Study," *Journal of Clinical Sleep Medecine*, vol. 10, no. 6, pp. 603-611, 2014.

- [8] G. Ding and C. Clavero, "Silver-Based Low-Emissivity Coating Technology for Energy-Saving Window Applications," in *Modern Technologies for Creating the Thin-film Systems and Coatings*, San Jose, Intermolecular, 2017.
- [9] D. & M. Gulfside Windows, "Low-E Glass Coating," 05 December 2018. [Online]. Available: <https://www.gulfsidefl.house/blog.php?post=low-e-glass-coating-2>.
- [10] R. McCluney, *Fenestration Solar Gain Analysis*, Orlando: Florida Solar Energy Center/University of Central Florida, 1996.
- [11] S. D. Rezaei, S. Shannigrahi and S. Ramakrishna, "A review of conventional, advanced, and smart glazing technologies and materials for improving indoor environment," *Sol. Energy Mater. Sol. Cells*, pp. 26-51, 2017.
- [12] S. Papaefthimiou, E. Syrrakou and P. Yianoulis, "An alternative approach for the energy and environmental rating of advanced glazing: An electrochromic window case study," *Energy and Buildings*, vol. 41, no. 1, pp. 17-26, 2009.
- [13] Visio-Rx, "Lens coatings," 2019. [Online]. Available: <https://www.visio-rx.com/vision-topics/lenses/lens-coatings>.
- [14] W. Zhao and E. M. Carreira, "Solid-Phase Synthesis of Photochromic," *Organic letters*, vol. 7, no. 8, pp. 1609-1612, 2005.
- [15] C.-G. Granqvist, *Handbook of Inorganic Electrochromic Materials*, Uppsala: Elsevier, 1995.
- [16] A. Kraft, "Electrochromism: a fascinating branch of electrochemistry," *ChemTexts*, vol. 5, no. 1, 2019.
- [17] R. J. Mortimer, "Organic electrochromic materials," *Electrochimica Acta*, vol. 44, no. 1, pp. 2971-2981, 1999.

- [18] P. Jittiarporn, S. Badilescu, M. N. A. Sawafta, S. Lek and V.-V. Truong, "Electrochromic Properties of Sol-Gel Prepared Hybrid Transition Metal Oxides A Short Review," *Science Direct*, vol. 2, no. 3, pp. 286-300, 2017.
- [19] F. Blanchard, B. Baloukas and L. Martinu, " Highly durable electrochromic tungsten oxide thin films," *Applied Materials Today*, vol. 12, pp. 235-243, 2018.
- [20] G. A. Niklasson and C. G. Granqvist, "Electrochromics for smart windows: Thin films of tungsten oxide and nickel oxide, and devices based on these," *Journal of Materials Chemistry*, vol. 17, no. 2, pp. 127-156, 2007.
- [21] S. K. Deb, "A Novel Electrophotographic System," *Applied Optics*, vol. 8, no. S1, pp. 192-195, 1969.
- [22] C. SUNSERI, F. D. QUARTO and A. D. PAOLA, "Kinetics of coloration of anodic electrochromic," *JOURNAL OF APPLIED ELECTROCHEMISTRY*, vol. 10, pp. 669-675, 1980.
- [23] G. A. Niklasson, L. Berggren and A.-L. Larsson, "Electrochromic tungsten oxide : the role of defects," *Solar Energy Materials*, vol. 84, no. 1-43, pp. 315-328, 2004.
- [24] H. Camirand, B. Baloukas, J. E. Klemberg-Sapieha and L. Martinu, "In situ spectroscopic ellipsometry of electrochromic amorphous tungsten oxide films," *Solar Energy Materials and Solar Cells*, vol. 140, pp. 77-85, 2015.
- [25] L. Berggren, *Optical Absorption and Electrical Conductivity in Lithium Intercalated Amorphous Tungsten Oxide Films*, Uppsala: Acta Universitatis Upsaliensis, 2004.
- [26] Y. Yamada, K. Tajima, S. Bao, M. Okada and K. Yoshimura, "Optical charge transfer absorption in proton injected tungsten oxide thin films analyzed with spectroscopic ellipsometry," *Solid State Ionics*, vol. 180, no. 6-8, pp. 659-661, 2009.

- [27] M. Kitao, K. Izawa, K. Urabe, T. Komatsu, S. Kuwano and S. Yamada, "Preparation and Electrochromic Properties of RF- Sputtered NiOx Films Prepared in Ar/O₂/H₂ Atmosphere Preparation and Electrochromic Properties of RF- Sputtered NiOx Films Prepared in Ar/O₂/H₂ Atmosphere," *Jpn. J. Appl. Phys*, vol. 33, pp. 6656-6662, 1994.
- [28] K.-S. Ahn, Y.-C. Nah and Y.-E. Sung, "Surface morphological, microstructural, and electrochromic properties of short-range ordered and crystalline nickel oxide thin films," *Applied Surface Science* 199, vol. 199, no. 1-4, pp. 259-269, 2002.
- [29] I. Bouessay, A. Rougier, P. Poizot, J. Moscovici, A. Michalowicz and J. M. Tarascon, "Electrochromic degradation in nickel oxide thin film: A self-discharge and dissolution phenomenon," *Electrochimica Acta*, vol. 50, no. 18, pp. 3737-3745, 2005.
- [30] D. S. Hall, D. J. Lockwood, C. Bock and B. R. MacDougall, "Nickel hydroxides and related materials: a review of their structures, synthesis and properties," *Proc Math Phys Eng Sci*, vol. 471, no. 2174, 2015.
- [31] A. A. WRONKOWSKA, "AN ELLIPSOMETRIC INVESTIGATION OF NICKEL OXIDE FILMS IN ALKALINE SOLUTION: THE MULTILAYER FILM APPROACH," *Surface Science* 2, vol. 214, pp. 507-522, 1989.
- [32] P. Häring and R. Kötz, "Nanoscale thickness changes of nickel hydroxide films during electrochemical oxidation/reduction monitored by in situ atomic force microscopy," *Journal of Electroanalytical Chemistry*, vol. 385, pp. 273-277, 1995.
- [33] L. d. Souza, F. P. Kong, F. R. McLarnon and R. H. Muller, "Spectroscopic ellipsometry study of nickel oxidation in alkaline solution," *Electrochimica Acta*, vol. 42, no. 8, pp. 1253-1267, 1997.
- [34] A. Pettersson, "ChromoGenics," ChromoGenics, [Online]. Available: <https://www.chromogenics.com/>. [Accessed 18 06 2020].

- [35] A.-L. Larsson, *All-Thin_Film Electrochromic Devices for Optical and Thermal modulation*, Uppsala: Universitetsstryckeriet, 2004.
- [36] H. Peng, X. Sun, W. Weng and X. Fang, "Electrically Driving Sensors Based on Polymer," in *Polymer Materials for Energy and Electronic Applications*, Shanghai, Academic Press, 2017, pp. 187-323.
- [37] K. Tajima, H. Hotta, Y. Yamada, M. Okada and K. Yoshimura, "Surface Analysis of Electrochromic Switchable Mirror Glass Based on Magnesium-Nickel Thin Film in Accelerated Degradation Test," *Materials Transactions*, vol. 52, no. 3, pp. 464-468, 2011.
- [38] L. Liu, K. Dub, Z. He, T. Wang, X. Zhong, T. Ma, J. Yang, Y. He, G. Dong, S. Wang and X. Diao, "High-temperature adaptive and robust ultra-thin inorganic all-solid-state smart electrochromic energy storage devices," *Nano Energy*, vol. 62, no. 1, pp. 46-54, 2019.
- [39] D. Dong, W. Wang, A. Rougier, A. Barnabe, G. Dong, F. Zhanga and X. Diao, "Lithium trapping as a degradation mechanism of the electrochromic properties of all-solid-state WO₃/NiO devices," *Journal of Materials Chemistry C*, vol. 6, no. 37, pp. 9875-9889, 2018.
- [40] *. M. A. A. Bill Baloukas, R.-T. Wen, G. A. Niklasson, C. G. Granqvist, R. Vernhes, J. E. Klemberg-Sapieha and L. Martinu, "Galvanostatic Rejuvenation of Electrochromic WO₃ Thin Films: Ion Trapping and Detrapping Observed by Optical Measurements and by Time-of-Flight Secondary Ion Mass Spectrometry," *Applied Materials and Interfaces*, vol. 9, no. 20, pp. 16995-17001, 2017.
- [41] S.-I. Park, Y.-J. Quan¹, S.-H. Kim, H. Kim, S. Kim, D.-M. Chun, C. S. Lee, M. Taya, W.-S. Chu and S.-H. Ahn, "A Review on Fabrication Processes for Electrochromic Devices," *INTERNATIONAL JOURNAL OF PRECISION ENGINEERING AND MANUFACTURING-GREEN TECHNOLOGY*, vol. 3, no. 4, pp. 397-421, 2016.
- [42] R. T. Rozbicki, "Fabrication of electrochromic devices". United States Patent US20180067370A1, 31 03 2009.

- [43] S. Palm, J.-C. Giron, P. Letocart, J. Roussele, t. Selles and K. Werner, "System and method for detecting and repairing defects in an electrochromic device using thermal imaging". United States Patent US20150097944A1, 29 03 2012.
- [44] B. S. Kwak and N. Krishna, "Electrochromic Devices". United States Patent US20120218620A1, 06 06 2008.
- [45] M. Kozlowski, E. Kurman, Z. Wang, M. Scobey, J. Dixon, A. Pradhan and R. Rozbicki, "Fabrication of low defectivity electrochromic devices". United States Patent US20100243427A1, 31 03 2009.
- [46] R. T. Rozbicki, "Fabrication of electrochromic devices". United States Patent US20180067370A1, 31 03 2009.
- [47] D. M. Moshfeghian, "Variation of properties in the dense phase region; Part 1 – Pure Compounds," PetroSkills, 1 12 2009. [Online]. Available: <http://www.jmcampbell.com/tip-of-the-month/2009/12/variation-of-properties-in-the-dense-phase-region-part-1-pure-compounds/>. [Accessed 25 05 2020].
- [48] R. Sherman, "Carbon Dioxide Snow Cleaning," *Developments in Surface Contamination and Cleaning*, pp. 987-1012, 2008.
- [49] C. clean, "Thermodynamics of CO2 Snow Formation," CO2 clean, - - -. [Online]. Available: <https://www.co2clean.com/snow-formation>. [Accessed 10 04 2020].
- [50] S. Swann, "MAGNETRON SPUTTERING," *Phys Technol*, vol. 19, pp. 67-75, 1998.
- [51] J. Musil, "Low-pressure magnetron sputtering," *Vacuum*, vol. 50, no. 3-4, pp. 363-372, 1998.
- [52] A. Anders, "A structure zone diagram including plasma-based deposition and ion etching," *Thin Solid Films*, vol. 518, no. 15, pp. 4087-4090, 2009.

- [53] R. Vernhes, A. Amassian, J. E. Klemberg-Sapieha and L. Martinu, "Plasma treatment of porous Si N x : H films for the fabrication of porous-dense," *JOURNAL OF APPLIED PHYSICS*, vol. 99, no. 11, p. 114315, 2006.
- [54] H. Mauser and G. Gauglitz, "Experimental Techniques in Photokinetic Analysis," in *Comprehensive Chemical Kinetics*, Tübingen, Elsevier, 1998, pp. 241-297.
- [55] A. Rothen, "The Ellipsometer, an Apparatus to Measure Thickness of Thin Surface Films," *Rev. Sci. Instrum.*, vol. 2, no. 26, p. 16, 1945.
- [56] Accurion, "Ellipsometry," Accurion, 2020. [Online]. Available: <https://www.accurion.com/ellipsometry>. [Accessed 07 05 2020].
- [57] S. Larouche and L. Martinu, "OpenFilters: open-source software for the design, optimization, and synthesis of optical filters," *Applied optics*, vol. 47, no. 13, 2008.
- [58] H. A. Macleod, Thin-film optical filters, fifth edition, Tuscon: Technology & Engineering, 2017.
- [59] J. ATTEBERRY, "How Scanning Electron Microscopes Work," How stuff works, [Online]. Available: <https://science.howstuffworks.com/scanning-electron-microscope2.htm>. [Accessed 07 05 2020].
- [60] T. H. Metzger, I. Kegel, R. Paniago, A. Lorke, J. Peisl, J. Schulze, I. Eisele, P. Schittenhelm and G. Abstreiter, "Shape, size, strain and correlations in quantum dot systems studied by grazing incidence X-ray scattering methods," *Thin Solid Films*, vol. 336, no. 1-2, pp. 1-8, 1998.
- [61] R. J. Composto, R. M. Walters and J. Genzer, "Application of ion scattering techniques to characterize polymer surfaces and interfaces," *Materials Science and Engineering*, vol. 38, pp. 107-180, 2002.

- [62] H. N. a. S. Gardner, "The Michelson Interferometer: Determining Doublet Wavelengths, Coherence Lengths, and Refractive Indices of Gases," flax, [Online]. Available: <http://flax.nzdl.org/greenstone3/flax;jsessionid=15E19BBADEB6F8B2DDF140B30DACAF01?a=d&c=BAWEPS&d=D1414&dt=simple&p.a=b&p.s=ClassifierBrowse#:~:text=This%20is%20because%20the%20coherence,is%200.03cm%20%5B%5D..> [Accessed 23 07 2020].
- [63] M. Dudek, A. Amassian, O. Zabeida, J. Klemberg-Sapieha and L. Martinu, "Ion bombardment-induced enhancement of the properties of indium tin oxide films prepared by plasma-assisted reactive magnetron sputtering," *Thin Solid Films*, vol. 517, pp. 4576-4582, 2009.
- [64] D.-G. Kim, S. Lee, G.-H. Lee and S.-C. Kwon, "Effects of hydrogen gas on properties of tin-doped indium oxide films deposited by radio frequency magnetron sputtering method," *Thin Solid Films*, vol. 515, no. 17, pp. 6949-6952, 2007.
- [65] K. Tajima, H. Hotta, Y. Yamada, M. Okada and K. Yoshimura, "Mg–Ni thin-film composition dependence of durability of electrochromic switchable mirror glass in simulated environment," *Solar Energy Materials and Solar Cells*, vol. 95, no. 12, pp. 3370-3376, 2011.
- [66] "Glove Boxes and Air Lock Chambers," Cleanroom synergy, [Online]. Available: <http://cleanroomsynergy.com/products/glove-boxes-air-lock-chambers/>. [Accessed 18 07 2020].
- [67] H. Wang, M. Barrett, B. Duane, J. Gu and F. Zenhausern, "msebReviewMaterials and processing of polymer-based electrochromic devicesHongfeng," *Materials Science & Engineering B*, vol. 228, pp. 167-174, 2018.
- [68] N. Li, S. Bao, Q. Zhang, L. Xie and P. Jin, "Wide-Band Reflection-Type, All-Solid-State Switchable Mirror Composed of WO₃–Mg₄Ni Thin Films and Proton-Conductive Polymer

- Electrolytes," *Materials Science inc. Nanomaterials & Polymers*, vol. 3, pp. 7507-7512, 2018.
- [69] A. Agrawal, J. P. Cronin and R. Zhang, "Review of solid state electrochromic coatings produced using sol-gel techniques," *Solar Energy Materials and Solar Cells*, vol. 31, no. 1, pp. 9-21, 1993.
- [70] M. K. Carpenter and D. A. Corrigan, "Photoelectrochemistry of Nickel Hydroxide Thin Films," *Journal of The Electrochemical Society*, vol. 136, no. 4, pp. 1022-1026, 1989.
- [71] P.-Y. Pennarun, S. Papaefthimiou, P. Yianoulis and P. Jannasch, "Electrochromic devices operating with electrolytes based on boronate ester compounds and various alkali metal salts," *Solar Energy Materials and Solar Cells*, vol. 91, no. 4, pp. 330-341, 2007.
- [72] C. G. Granqvist, "Electrochromics for smart windows: Oxide-based thin films and devices," *Thin Solid Films*, vol. 564, pp. 1-38, 2014.
- [73] K. Ono, N. Nakazaki, H. Tsuda, Y. Takao and K. Eriguchi, "Surface morphology evolution during plasma etching of silicon: roughening, smoothing and ripple formation," *Journal of Physics D: Applied Physics*, vol. 50, no. 41, pp. 1-103, 2017.
- [74] D. Pereles, J. Gorley, B. Hensley, C. Loberg and A. Wolke, "Performing Cyclic Voltammetry," Tektronix, 6 11 2015. [Online]. Available: <https://www.tek.com/blog/performing-cyclic-voltammetry>. [Accessed 15 4 2020].
- [75] A. W. H. Cezarina C. Mardare, "Review on the Versatility of Tungsten Oxide Coatings," *Phys. Status Solidi A*, vol. 216, pp. 1-16, 2019.
- [76] M. Hibino, W. Han and T. Kudo, "Electrochemical lithium intercalation into a hexagonal WO₃ framework and its structural change," *Solid State Ionics*, vol. 135, no. 1-4, pp. 61-69, 2000.

- [77] C. G. Granqvist, "Electrochromic glazing for energy efficient buildings," *Nanotechnology in Eco-efficient Construction*, pp. 467-501, 2019.
- [78] A. Bearnot and A. Greene, *Study and Comparison of Coins by X-ray Diffraction (XRD); Preliminary Findings*, <https://blogs.brown.edu/archaeology/files/2015/07/Study-and-Comparison-of-Coins-by-X-Ray-Diffraction.pdf>.
- [79] D. S. Hall, D. J. Lockwood, C. Bock and B. R. MacDougall, "Nickel hydroxides and related materials: a review of their structures, synthesis and properties," *Proc Math Phys Eng Sci*, vol. 471, no. 2174, pp. -, 2105.
- [80] S. Mohseni, Meybodi, S. Hosseini, M. Rezaee, S. Sadrnezhad and D. M. Yani, "Synthesis of wide band gap nanocrystalline NiO powder via sonochemical method," *Ultrasonics Sonochemistry*, vol. 19, no. 4, pp. 841-845, 2012.
- [81] C. A. C. Sequiera and D. M. F. Santos, "Tungsten Oxide Electrochromic Windows with Lithium Polymer Electrolytes," *Journal of the electrochemical society*, vol. 157, no. 6, pp. 202-207, 2020.